CWP-235
December 1996

Reflection Coefficients and Azimuthal AVO Analysis in Anisotropic Media

Andreas Rüger

— Doctoral Thesis —
Geophysics

Center for Wave Phenomena
Colorado School of Mines
Golden, Colorado 80401
303/273-3557

This thesis is dedicated to the memory of my daughter Linda Nadine

ABSTRACT

Reflection and transmission of plane waves at a plane boundary between two homogeneous halfspaces is one of the most fundamental problems in wave propagation. One application of reflection-coefficient studies of practical importance is analysis of amplitude variations with offset (AVO), which can be used for direct detection of hydrocarbons.

While numerical evaluation of the reflection coefficient is relatively straightforward, the algebraic complexity of the solution greatly impedes any analytic insight into the influence of medium parameters on the AVO signature. Conventional AVO analysis in isotropic media is based primarily on approximate analytic solutions of the reflection/transmission problem. In this thesis, a similar approach is used to elucidate the influence of anisotropy on the reflection response in anisotropic media.

Transverse isotropy with a vertical axis of symmetry (VTI media) is the simplest anisotropic model typically used to describe thinly layered media and shale sequences. The approximate expression for reflection coefficients in VTI media derived here has the same AVO-gradient term describing the low-order angular variation of the reflection coefficient as do the equations published by Banik (1987) and Thomsen (1993), but is more accurate for large incidence angles. The refined approximation is then extended to transverse isotropy with a horizontal axis of symmetry (HTI) – the symmetry system typically caused by a system of parallel vertical cracks. Expressions for the reflection and transmission coefficients in the vertical symmetry planes of HTI media are obtained by taking advantage of a limited analogy with VTI models. This analogy is of far-reaching importance: it is the key step in deriving all kinematic signatures and polarizations in HTI media and leads to a new parameterization of HTI models that proves to be very convenient in surface seismic applications.

The newly-derived approximate symmetry-plane P-wave reflection coefficient is further generalized to observations at arbitrary azimuth. The AVO-gradient term in the approximate P-wave reflection coefficient in HTI media varies with azimuth as a function of the squared cosine of the azimuthal angle. Azimuthal variation in the gradient term can be inverted for the symmetry-plane directions and a combination of the shear-wave splitting parameter (Thomsen's parameter γ) and the newly introduced anisotropy coefficient $\delta^{(V)}$ describing P-wave anisotropy for near-vertical propagation. Since $\delta^{(V)}$ can be found from the P-wave NMO velocity, these results make it possible to combine P-wave AVO response with moveout data in the evaluation of the shear-wave splitting parameter, which is close to the crack density. P-wave AVO data alone are sufficient to estimate the crack density in the special case of thin saturated cracks and negligible equant porosity, typical for fractured coals.

To provide a physical foundation for multi-component AVO studies in azimuthally anisotropic media, I have also obtained approximate symmetry-plane reflection coeffi-

cients for shear and converted waves in HTI media, as well as for waves propagating in orthorhombic models. Also discussed in the thesis are practical aspects and difficulties of applying the azimuthal AVO analysis in the case of an anisotropic overburden.

TABLE OF CONTENTS

ACKNOWLEDGMENTS

The successful completion of a Ph.D is not a personal effort, it is a consequence of the help and support of family and friends. I am thankful to my parents Gisela and Bernd who encouraged me to pursue a higher-level education. My interest in art and science was particularly inspired by Thomas Unseld and Ottmar Siegel. Professor Hubral first introduced me to exploration geophysics. His support and the help of Uwe Kästner, Wilfried Jokat and Professor Wilhelm enriched my studies with the opportunity to make my first steps in the field of seismology, to travel and finally to reach out for a degree at CSM. My friends Norbert Pralle, Ralph Skoda, Sabine Philippin and Ursula Claus always stayed in touch and made sure that geophysics was not the only part of my life. Norbert was also the key-player in discovering my interest for Spain and the US, its people and culture.

Without the support of my friends Herman Jaramillo, Lydia Deng and Omar Uzcatequi, my stay at Mines would have been a short one. They taught me that "prime" means derivative, that C is a learnable programming language and that help and friendship are possible even in a demanding school. Timo Tjan, Ted Shuck, Wences Gouveia, Craig Artley, Gilein Steensma, Alberto Villareal, Alejandro Murillo, Tagir Galikee, Brian De Vault, Raul Cabrera, Bruce Mattocks, Norman Ettrich, Björn Rommel and many others are acknowledged for help, fun and advice. Also thanks to Sam and Jean for making us feel at home in Denver.

My gratitude also goes to the professors and staff at CSM. Dave Hale initiated my interest in programming, Jack Cohen and Norm Bleistein helped me build the self-esteem necessary to do research and Ken Larner taught me how to organize and communicate it. His lessons in writing papers, lecturing and giving talks will leave a permanent imprint (according to his letter-size rules, of course). Marge, Jo Ann, Barbara, Michelle, Peggy and Seismic Unix guru John Stockwell were always helpful and took much work off of my shoulders.

I want to give my deepest appreciation to Ilya Tsvankin for his advice and direction that led me into this specific area of research. I admire his analytical insight and unmatched sharpness of thinking. As my advisor, he always gave me the freedom that I needed to develop original ideas. He supported me even in times when I was in doubt about my own performance. My research was also enriched by talking to Vladimir Grechka, Tariq Al-Khalifah, Leon Thomsen, Ted Shuck, Dennis Corrigan, Geir Haugen, Richard Bates, Heloise Lynn, Richard van Doc, Subhashis Mallick, Martijn de Hoop, Al-Dajani Abdulfattah and many others.

I also want to thank the members of my Ph.D committee – Norm Bleistein, Tom Boyd, Ken Larner, Steve Pruess, John Scales and Ted Shuck – who all played an important role in defining this thesis, and John Anderson, Alex Kaufmann, Terry Young and Joe Higginbotham who trusted in me and provided me with exciting professional

opportunities. Financial support for my studies has been provided by Fulbright-, SEG-, and Phillips Petroleum scholarships, as well as by the consortium members of CWP.

Finally, I am most indebted to my wonderful spouse Christa and our precious daughter Sydney Jean. Christa's love and support made all this work possible and Sydney's charm and smile turned the last months into a very enjoyable experience.

Chapter 1

INTRODUCTION

Reflection and transmission of plane waves at a plane boundary between two isotropic media is one of the most fundamental problems in wave propagation. Zoeppritz (1919) was among the first to publish the solution to this problem invoking continuity of stress and displacement at the reflecting horizon.

One important application of reflection-coefficient studies is analysis of amplitude variations with offset (AVO). The variation of P-wave amplitudes with incidence angle provides one of the few direct hydrocarbon indicators (Ostrander, 1982) and has drawn substantial attention within the geophysical community.

Due to the algebraic complexity of the Zoeppritz equations, conventional AVO analysis is mostly based on approximate analytic expressions for P-wave reflection coefficients in isotropic media. Several approximations for isotropic models have been described in the literature (Richards & Frasier, 1976; Aki & Richards, 1980; Shuey, 1985; Thomsen, 1990); they differ in their assumptions, as well as in the choice of medium parameters. Chapter 2 provides an overview of the reflection and transmission problem in isotropic media. It also introduces the notation that is used throughout the thesis and contains a review of the basic physical principles that lead to the boundary conditions at interfaces in welded contact.

Conventional AVO analysis is based on approximate isotropic reflection coefficients and needs to be modified if anisotropy is present on either side of the reflecting boundary. Reflection and transmission of plane waves at an interface between two anisotropic media have been discussed, for example, by Musgrave (1970), Henneke (1972), Keith and Crampin (1977) and Daley and Hron (1977). Even more so than in the isotropic case, the exact solution for reflection coefficients at interfaces of anisotropic media is very complicated. The general solution cannot be presented in closed form and requires a numerical inversion of 6x6 matrices. The matrix components include polarizations and tractions of three different wave modes in both media that have to be obtained by the eigenvalue/eigenvector analysis of the Christoffel equation (Musgrave, 1970). The complexity of the problem obscures any physical insight into the AVO signature. Empirical and analytic studies, however, show that the presence of anisotropy can significantly distort the conventional AVO analysis (Wright, 1986; Banik, 1987; Kim *et al.*, 1993).

In the first part of Chapter 3, I discuss wave propagation and medium parameterization for transversely isotropic media with a vertical axis of symmetry (VTI media). The VTI model provides an adequate description of wave propagation in thinly layered media with horizontal interfaces and horizontally stratified shale formations. I follow Graebner's (1992) derivation of the exact reflection coefficients and

explain how the solution can be extended to plane dipping interfaces. As in the isotropic case, the reflection coefficients are evaluated for the displacement vector, and the positive polarization direction is chosen according to the sign convention in Aki and Richards (1980). Following Thomsen (1993), I then derive a refined approximation for the reflection and transmission coefficients for pure and converted modes assuming weak anisotropy and a boundary with small discontinuities in elastic properties. The derived approximation for the quasi *P*-wave [1] reflection coefficient has the same gradient term as does the solution presented by Banik (1987) and Thomsen (1993), but is more accurate at larger angles.

The remaining part of this thesis is devoted to media with azimuthally varying properties. While approximate reflection coefficients are available for isotropic and VTI media, corresponding expressions are unknown for media that are azimuthally anisotropic. One plausible explanation for the azimuthal anisotropy observed in seismic field data (Lynn *et al.*, 1995; Johnson, 1995) is natural fracturing of rocks, with fractures aligned in accordance with the dominant stress direction (Crampin, 1984a; Crampin, 1985). Anisotropic compressional stresses required to fracture rocks are relatively small and even flat-lying strata are commonly fractured, with the most famous example probably being the Austin Chalk in Texas (Mueller, 1991). This observation can be of crucial importance to hydrocarbon exploration since fracture networks often determine the direction and amount of fluid flow through reservoir rocks. Other physical reasons for azimuthally isotropic media include dipping shale sequences and intrinsic anisotropy.

The first-order azimuthally anisotropic model is the transversely isotropic medium with a horizontal axis of rotational symmetry (HTI media) that is frequently used to describe vertically-aligned penny-shaped cracks in an isotropic matrix (Thomsen, 1995). Because of its importance for reservoir characterization, much attention has been devoted to this model, mainly through analysis of shear-wave birefringence (Crampin, 1984a; Martin & Davis, 1987; Mueller, 1991; Shuck *et al.*, 1996). Azimuthal anisotropy has a first-order influence on vertically incident shear waves causing them to split into two components traveling with different velocities. In addition to the crack orientation, the parameter of crack systems of great interest in exploration is the crack density, which is close to the fractional difference between the velocities of split shear waves at vertical incidence [Thomsen's (1986) coefficient γ].

Chapter 4 reviews the significance of the HTI model and describes a limited analogy between wave propagation in HTI and VTI media. This analogy is the key step not only in deriving the approximate reflection coefficients, but also in obtaining kinematic properties and polarizations in HTI media. As shown in Chapter 4, this analogy implies that the known exact solutions for VTI reflection coefficients can be

[1] The qualifier in "quasi *P*-wave" refers to the fact that, for anisotropic media, the fastest (*P*-) wave is not polarized in either the slowness or ray directions; similarly, the *SV*-wave in anisotropic media is not polarized normal to the slowness or ray directions. In the following, I will omit the qualifier "quasi" in "*P*-wave" and "*SV*-wave".

used to evaluate the reflection coefficient for waves incident in the vertical plane containing the symmetry axis of HTI models. The observed analogy also leads to the introduction of a new set of dimensionless anisotropy parameters similar to Thomsen's (1986) coefficients that conveniently describe seismic reflection signatures in HTI media.

While seismic signatures of compressional waves in transversely isotropic media with a vertical axis of symmetry (VTI) have been an active study area in the last decade, research on HTI media has been predominantly focused on the propagation of shear waves, and the dependence of compressional wave data on azimuthal anisotropy is much less understood. Specifically, *P*-wave data are rarely used to directly detect and characterize fractured zones or "weak spots" of high crack density. Certainly, a method for direct detection of fracturing using *P*-wave data would be highly beneficial. The exploration community has become very sophisticated in the acquisition and processing of *P*-wave data; additionally, compressional data generally have better quality and are cheaper as compared to shear-wave data.

Just recently, it has been shown that *P*-wave AVO signatures are sensitive to fractures or cracks. Based on synthetic modeling studies, Mallick and Frazer (1991) suggested determining fracture orientation from *P*-wave AVO. More recently, Lefeuvre (1994) discussed the possibility of using *P*-wave reflections to infer fracture parameters statistically; however, he did not provide analytic insight into the relation between *P*-wave signatures and anisotropy parameters.

The approximate solutions for *P*-*P* reflection and transmission coefficients at a horizontal interface between two HTI media are first derived for waves incident in the two vertical symmetry planes of HTI media. In Chapter 5, this analysis is extended to waves incident in arbitrary azimuthal directions. The gained insight is helpful in characterizing the magnitude and the functional form of the azimuthal variation caused by different anisotropy parameters. The original goal of isotropic AVO analysis was to extract shear-wave information from the variations of the reflection coefficient with incidence angle. The results obtained in this chapter make it possible to devise a fracture-detection algorithm based on the inversion of azimuthal differences of the *P*-wave AVO gradient.

Estimates of anisotropy using the time delay between the fast and slow shear waves yield robust, alternative measurements of γ averaged over the propagation path of the shear waves. Thus, analysis of shear-wave kinematic signatures via the classical rotation analysis (Alford, 1986) helps to estimate the crack density (for HTI media), albeit with a low vertical resolution. For situations where a detailed measure of local anisotropy (highly resolved in depth/time) is desired, or where the rotation analysis fails due to insignificant time delays, Thomsen (1988), Lynn and Thomsen (1990) and Yardley et. al. (1991) suggest using the differences in the normal-incidence shear-wave reflection coefficients, as well as the amplitude-variation-with-offset signature to characterize the fracturing below the reflector. Yardley et. al. (1991) used the reflectivity method to compute the reflection coefficients as a function of incidence angle for various azimuthally anisotropic two-layer models. They modeled layers of

HTI symmetry that contain parallel vertical cracks normal and oblique to the survey line and discussed changes in the shear-wave reflection response for layers with water- and gas-filled cracks. Their results show a clear dependence of the S-wave AVO response on both the crack density and crack content. Yardley et. al. (1991) also emphasized severe difficulties in measuring shear-wave amplitudes if the acquisition (survey) line is not parallel or perpendicular to the crack orientation.

The results obtained by Yardley et. al. (1991) motivate a more detailed analysis of wave propagation and AVO for shear waves in HTI media (Chapter 6). As in the P-wave study, the approximate analytic equations for shear-wave reflection coefficients derived in this chapter are valid for interfaces between two HTI media (the principal axes of symmetry should coincide in both layers) and for interfaces between HTI and VTI layers. A typical geologic model for the VTI/HTI boundary is a massive shale layer overlying a fractured reservoir. Also derived in this chapter are reflection and transmission coefficients for the converted (PS) waves in the two vertical symmetry planes of HTI media.

Finally, an extension of the developed formalism to vertical symmetry planes of orthorhombic media is described in Chapter 7. Media of orthorhombic symmetry, believed to represent more realistic azimuthally anisotropic models, can, for example, be caused by a combination of horizontal layering and parallel vertical cracks. Likewise, a system of two orthogonal, but not necessary identical, crack systems or two identical crack systems at an oblique angle to each other lead to orthorhombic symmetry (Winterstein, 1990). As demonstrated in Chapter 7, the reflection coefficients in orthorhombic and HTI media are similar and the azimuthal variation in the P-wave reflection response is a function of the shear-wave splitting parameter γ and two anisotropy parameters describing P-wave anisotropy for near-vertical propagation in the symmetry planes.

Application of the developed AVO-inversion methods to synthetically modeled surface reflection data is given in Chapter 8. The data have been generated using both the reflectivity method (Mallick & Frazer, 1990) and dynamic ray tracing (Gajewski & Pšenčik, 1990). Especially important is a discussion of the influence of the overburden on the seismic reflection amplitudes and the AVO inversion. The chapter contains suggestions on processing and interpretation of field data to be used in azimuthal AVO analysis. Also discussed are potential extensions and applications of this work.

Chapter 2

REVEEW OF REFLECTION AND TRANSMISSION IN ISOTROPIC MEDIA

Reflection and transmission of seismic waves in isotropic media is a fundamental geophysical problem that has been intensively studied in the literature. The first papers related to this topic were published in the 19th century (Green, 1839; Knott, 1899). Zoeppritz (1919) was the first to produce a set of equations to compute particle-displacement amplitudes of reflected and transmitted waves in isotropic media. The anisotropic case is a much more difficult one. Incident and reflected waves have directionally-dependent wave speeds and can no longer be thought of as purely longitudinally or transversely polarized. In addition, the direction of the wave normal, the particle movement and the energy flux do not coincide with each other. However, despite these complications, the principles of computing reflection coefficients in isotropic and anisotropic media are similar. Also, reviewing analytic studies developed for isotropic waves leads to very useful approaches for analyzing reflection and transmission in anisotropic media. This – together with the fact that analysis and application of isotropic reflection coefficients is still an active research topic – motivates the following introductory chapter on scattering in isotropic media.

2.1 Wavefields in isotropic media – notation

Two different types of body waves propagate in isotropic media. If the medium is homogeneous, both waves from a localized source spread out as spherical wavefronts, but heterogeneities can distort them in various ways. The first wave type is the *P*-wave; *P* simply means "primary", because *P*-waves arrive earlier than the ("secondary") *S*-waves. *P*-waves are compressional and cause the medium to alternatively undergo compression and rarefaction. *S*-waves are shear waves generating a transverse particle motion; i.e., the particle motion is perpendicular to the propagation direction. Two different shear waves can be distinguished upon incidence at a boundary. The *S*-wave polarized in the plane formed by the normal to the interface and the propagation direction is called the *SV*-wave; the wave polarized within the interface is referred to as the *SH*-wave. The propagation speeds of *P*-waves and *S*-waves are

$$\begin{aligned} V_P &= \sqrt{(\lambda + 2\mu)/\rho} \\ V_S &= \sqrt{\mu/\rho}, \end{aligned} \tag{2.1}$$

where λ and μ are known as Lamé constants and ρ is the density of the medium.

If the radius of a spherical wave front is large compared to the wavelength of the body wave, the wavefront can be locally approximated by a plane surface. In this thesis, plane-wave reflection and transmission coefficients are derived. This however does not mean that analysis of spherical waves is out of the scope of this thesis: spherical waves can be decomposed into plane waves, and the derived theoretical results can be applied to each plane wave individually.

To describe the wavefields scattered at a plane horizontal interface, I adopt the sign convention introduced by Aki and Richard (1980): the positive polarization direction is such that the horizontal component points in the direction of horizontal slowness (Figure 2.1). As conventionally assumed in the seismological signature, the x_3-axis is pointing downwards and the x_2-axis is normal to the incidence plane. The wave-

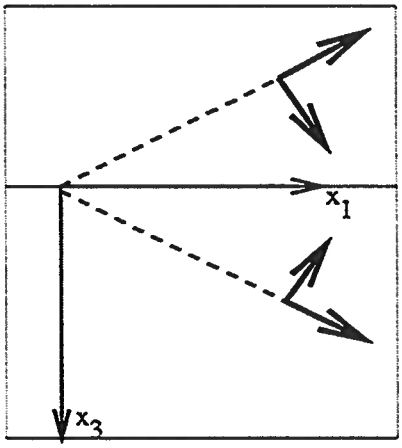

FIG. 2.1. Sign convention: the positive particle polarization directions for *P*-waves and *SV*-waves are indicated by thick black arrows. The dashed lines show the propagation directions of waves in the upper and lower medium. The interface is defined as $x_3 = 0$.

field generated by an incident *P*-wave of unit amplitude upon the horizontal reflector $x_3 = 0$ is shown in Figure 2.2. For a given frequency ω and horizontal slowness p, the particle displacement u_i of the (unit amplitude) plane wave incident in the $[x_1, x_3]$ plane can be written as

$$\mathbf{u}_P^{\text{inc}} = \begin{pmatrix} \mathrm{l}_{i_1} \sin i_1 \\ \mathrm{m}_{i_1} \cos i_1 \end{pmatrix} e^{i\omega\left(p x_1 + \frac{\cos i_1}{v_{i_1}} x_3 - t\right)}. \tag{2.2}$$

The displacement vector of an incident *SV*-wave can be represented as

$$\mathbf{u}_{SV}^{\text{inc}} = \begin{pmatrix} \mathrm{m}_{j_1} \cos j_1 \\ -\mathrm{l}_{j_1} \sin j_1 \end{pmatrix} e^{i\omega\left(p x_1 + \frac{\cos j_1}{v_{j_1}} x_3 - t\right)}. \tag{2.3}$$

This notation is quite general and will also be used in transversely isotropic media. For isotropic media, $l_{i_k} = l_{j_k} = m_{i_k} = m_{j_k} = 1$ $(k = 1, 2)$; i.e., the waves are polarized parallel and perpendicular to the phase direction. Velocities v_{i_1}, v_{j_1}, v_{i_2} and v_{j_2} are the P-wave and SV-wave velocities of the upper and lower medium, respectively. Angles i_k and j_k $(k = 1, 2)$ are shown in Figure 2.2. The generated wave modes are

$$\begin{aligned}
\acute{\mathbf{u}}_P &= \acute{P} \cdot \begin{pmatrix} l_{i_1} \sin i_1 \\ -m_{i_1} \cos i_1 \end{pmatrix} e^{i\omega\left(px_1 - \frac{\cos i_1}{v_{i_1}} x_3 - t\right)} \\
\acute{\mathbf{u}}_S &= \acute{S} \cdot \begin{pmatrix} m_{j_1} \cos j_1 \\ l_{j_1} \sin j_1 \end{pmatrix} e^{i\omega\left(px_1 - \frac{\cos j_1}{v_{j_1}} x_3 - t\right)} \\
\grave{\mathbf{u}}_P &= \grave{P} \cdot \begin{pmatrix} l_{i_2} \sin i_2 \\ m_{i_2} \cos i_2 \end{pmatrix} e^{i\omega\left(px_1 + \frac{\cos i_2}{v_{i_2}} x_3 - t\right)} \\
\grave{\mathbf{u}}_S &= \grave{S} \cdot \begin{pmatrix} m_{j_2} \cos j_2 \\ -l_{j_2} \sin j_2 \end{pmatrix} e^{i\omega\left(px_1 + \frac{\cos j_2}{v_{j_2}} x_3 - t\right)} .
\end{aligned} \tag{2.4}$$

Here, $\acute{P}, \grave{P}, \acute{S}$ and $\grave{S}$ denote the amplitudes of the scattered wave modes. The situation with an incident SH-wave is more simple. Unlike the P-wave and SV-wave modes, this wave is polarized perpendicular to both the normal to the interface and the direction of wave propagation. Hence, the incident SH-wave can generate only reflected and transmitted SH-waves. This decoupling of P-SV and SH propagation exists in isotropic media and symmetry planes of anisotropic models. In general azimuthally anisotropic media, the three wave modes are coupled, which leads to a more difficult treatment of energy partitioning at plane horizontal interfaces.

2.2 Boundary conditions and exact scattering formulas

Computation of plane-wave reflection and transmission coefficients (also called scattering coefficients) is based on two physical principles. First, the displacement amplitudes have to be continuous at boundaries between media which are in welded contact. In other words, the media on both sides of the boundary cannot be ripped apart and no slippage is allowed along the interface. These conditions are often referred to as "kinematic" boundary conditions. Secondly, the components of the stress tensor corresponding to the traction across the interface have to be continuous. The continuity of stress across the interface is called the "dynamic" boundary condition.

The kinematic boundary conditions require that the particle displacement caused by P- or SV-waves incident in the $[x_1, x_3]$ plane satisfies

$$[u_1] = [u_3] = 0 \tag{2.5}$$

at the boundary, where the square brackets denote the difference in displacement above

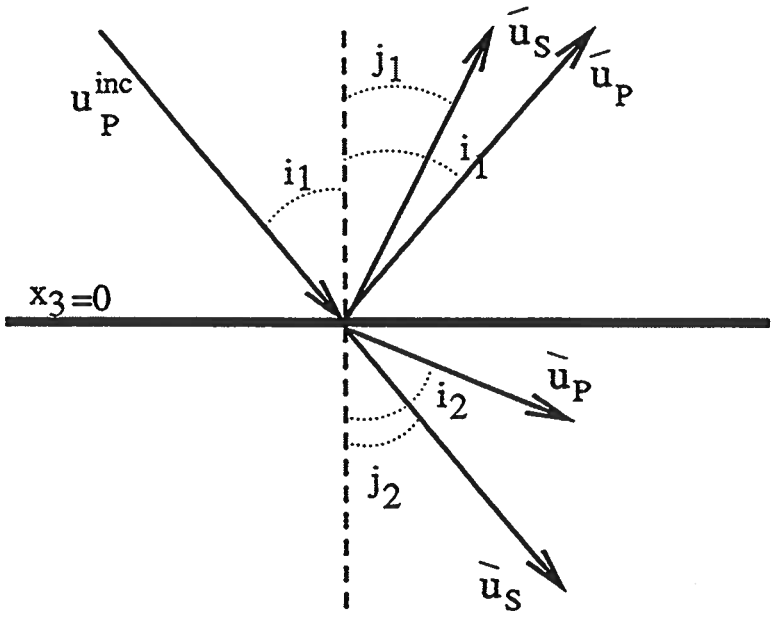

FIG. 2.2. Two upgoing wave modes ($\acute{\mathbf{u}}_P, \acute{\mathbf{u}}_S$) and two downgoing waves ($\grave{\mathbf{u}}_P, \grave{\mathbf{u}}_S$) are generated by an incident P-wave ($\mathbf{u}_P^{inc}$).

and below the boundary. For an incident P-wave, equations (2.2), (2.4) and (2.5) yield

$$\begin{aligned} -\mathrm{l}_{i_1}\sin i_1 &= \acute{P}\,\mathrm{l}_{i_1}\sin i_1 - \grave{P}\,\mathrm{l}_{i_2}\sin i_2 + \acute{S}\,\mathrm{m}_{j_1}\cos j_1 - \grave{S}\,\mathrm{m}_{j_2}\cos j_2 \\ -\mathrm{m}_{i_1}\cos i_1 &= -\acute{P}\,\mathrm{m}_{i_1}\cos i_1 - \grave{P}\,\mathrm{m}_{i_2}\cos i_2 + \acute{S}\,\mathrm{l}_{j_1}\sin j_1 + \grave{S}\,\mathrm{l}_{j_2}\sin j_2\,. \end{aligned} \quad (2.6)$$

Equation (2.5) has to be satisfied at any time and point along the interface. Consequently, the phase terms in equations (2.3) and (2.4) need to be identical at the boundary. This is a statement of Snell's law that requires the horizontal slowness to be continuous across the interface, i.e.,

$$\sin i_1/v_{i_1} = \sin i_2/v_{i_2} = \sin j_1/v_{j_1} = \sin j_2/v_{j_2}\,.$$

To honor the dynamic boundary conditions, the traction acting across the plane normal to the x_3-axis has to be continuous. From the definition of the stress tensor (Aki & Richards, 1980), the k-th component of the traction $\mathbf{T}$ acting across the horizontal interface can be written as

$$\tau_{3k} = T_k(\hat{\mathbf{x}}_3)\,,\ (k=1,2,3)\,,$$

with $\hat{\mathbf{x}}_3$ denoting the unit vector in direction of the x_3-axis, i.e., normal to the horizontal interface. If the medium is elastic (as is assumed throughout this thesis), the

stress tensor can be related to displacement using the constitutive relation

$$\tau_{ij} = 1/2\, c_{ijkl}\,(u_{k,l} + u_{l,k})\,. \tag{2.7}$$

Here, the Einstein summation over repeated indices is used and the comma in $u_{k,l}$ indicates a partial derivative with respect to the l-th component. c_{ijkl} is a tensor of rank four with at most 21 independent constants. In the special case of isotropic media, the number of independent components reduces to just two [see Musgrave (1970) for more details]. For *P-SV* propagation in the $[x_1, x_3]$-plane, the dynamic boundary conditions are

$$[\tau_{13}] = [\tau_{33}] = 0\,. \tag{2.8}$$

The component τ_{23} of the traction $\mathbf{T}(\hat{\mathbf{x}}_3)$ is nonzero only in case of an incident *SH*-wave. Equation (2.8), together with the constitutive relation (2.7) and the wavefield representations (2.2) and (2.4) yield two more equations for the unknown amplitude factors $\acute{P}, \acute{S}, \grave{P}$ and $\grave{S}$:

$$\begin{aligned}
-c_{55}^{(1)} \left(\mathrm{l}_{i_1} \sin i_1 \frac{\cos i_1}{v_{i_1}} + p\, \mathrm{m}_{i_1} \cos i_1 \right) \;=\; & \\
& \acute{P}\, c_{55}^{(1)} \left(-\frac{\cos i_1}{v_{i_1}} \mathrm{l}_{i_1} \sin i_1 - p\, \mathrm{m}_{i_1} \cos i_1 \right) + \\
& \acute{S}\, c_{55}^{(1)} \left(-\frac{\cos j_1}{v_{j_1}} \mathrm{m}_{j_1} \cos j_1 + p\, \mathrm{l}_{j_1} \sin j_1 \right) + \\
& \grave{P}\, c_{55}^{(2)} \left(-\frac{\cos i_2}{v_{i_2}} \mathrm{l}_{i_2} \sin i_2 - p\, \mathrm{m}_{i_2} \cos i_2 \right) + \\
& \grave{S}\, c_{55}^{(2)} \left(-\frac{\cos j_2}{v_{j_2}} \mathrm{m}_{j_2} \cos j_2 + p\, \mathrm{l}_{j_2} \sin j_2 \right)\,,
\end{aligned} \tag{2.9}$$

and

$$\begin{aligned}
-c_{13}^{(1)}\, p\, \mathrm{l}_{i_1} \sin i_1 - c_{33}^{(1)} \frac{\cos i_1}{v_{i_1}} \mathrm{m}_{i_1} \cos i_1 \;=\; & \\
& \acute{P} \left(c_{13}^{(1)}\, p\, \mathrm{l}_{i_1} \sin i_1 + c_{33}^{(1)} \frac{\cos i_1}{v_{i_1}} \mathrm{m}_{i_1} \cos i_1 \right) + \\
& \acute{S} \left(c_{13}^{(1)}\, p\, \mathrm{m}_{j_1} \cos j_1 - c_{33}^{(1)} \frac{\cos j_1}{v_{j_1}} \mathrm{l}_{j_1} \sin j_1 \right) + \\
& \grave{P} \left(-c_{13}^{(2)}\, p\, \mathrm{l}_{i_2} \sin i_2 - c_{33}^{(2)} \frac{\cos i_2}{v_{i_2}} \mathrm{m}_{i_2} \cos i_2 \right) + \\
& \grave{S} \left(-c_{13}^{(2)}\, p\, \mathrm{m}_{j_2} \cos j_2 + c_{33}^{(2)} \frac{\cos j_2}{v_{j_2}} \mathrm{l}_{j_2} \sin j_2 \right)\,.
\end{aligned} \tag{2.10}$$

Again, these equations are quite general and will be used below to derive the reflection

coefficients in VTI media and the vertical symmetry-planes in azimuthally anisotropic media. In isotropic media, $\mathrm{l}_{i_k} = \mathrm{l}_{j_k} = \mathrm{m}_{i_k} = \mathrm{m}_{j_k} = 1$ $(k = 1, 2)$. The three stiffness components c_{33}, c_{55} and c_{13} are shown in the two-index notation (Voigt recipe), and the superscripts $^{(1)}$ and $^{(2)}$ refer to the upper and lower medium, respectively. In isotropic media

$$\begin{aligned}
c_{33}^{(1)} &= c_{3333}^{(1)} = \rho^{(1)} v_{i_1}^2 ; \\
c_{33}^{(2)} &= c_{3333}^{(2)} = \rho^{(2)} v_{i_2}^2 ; \\
c_{55}^{(1)} &= c_{1313}^{(1)} = \rho^{(1)} v_{j_1}^2 ; \\
c_{55}^{(2)} &= c_{1313}^{(2)} = \rho^{(2)} v_{j_2}^2 ; \\
c_{13}^{(1)} &= c_{1133}^{(1)} = c_{33}^{(1)} - 2\, c_{55}^{(1)} ; \\
c_{13}^{(2)} &= c_{1133}^{(2)} = c_{33}^{(2)} - 2\, c_{55}^{(2)} .
\end{aligned} \tag{2.11}$$

The incident P-wave has a unit amplitude and the unknowns $\acute{P}, \acute{S}, \grave{P}$ and $\grave{S}$ represent the (displacement) reflection and transmission coefficients. They can be evaluated by solving the linear system of four equations (2.6), (2.9) and (2.10). A similar set of equations can be derived for an incident SV-wave. The reflection/transmission problem is much simpler for the SH-wave. In this case, only two equations have to be solved.

Although this derivation is straightforward, the analytic expressions for the scattering coefficients are rather complex and readily prone to error. The solution for the P-wave reflection coefficient in isotropic media, for example, is given in Aki and Richards (1980) as

$$\acute{P} = \left[\left(b \frac{\cos i_1}{v_{i_1}} - c \frac{\cos i_2}{v_{i_2}} \right) F - \left(a + d \frac{\cos i_1}{v_{i_1}} \frac{\cos j_2}{v_{j_2}} \right) H p^2 \right] / D , \tag{2.12}$$

with

$$\begin{aligned}
D &= E F + G H p^2 \\
E &= b \frac{\cos i_1}{v_{i_1}} + c \frac{\cos i_2}{v_{i_2}} \\
F &= b \frac{\cos j_1}{v_{j_1}} + c \frac{\cos j_2}{v_{j_2}} \\
G &= a - d \frac{\cos i_1}{v_{i_1}} \frac{\cos j_2}{v_{j_2}} \\
H &= a - d \frac{\cos i_2}{v_{i_2}} \frac{\cos j_1}{v_{j_1}} .
\end{aligned} \tag{2.13}$$

The remaining parameters are given by

$$a = \rho^{(2)} (1 - 2 v_{j_2}^2 p^2) - \rho^{(1)} (1 - 2 v_{j_1}^2 p^2)$$

$$
\begin{aligned}
b &= \rho^{(2)}\,(1-2\,v_{j_2}^2\,p^2) + 2\,\rho^{(1)}\,v_{j_1}^2\,p^2 \\
c &= \rho^{(1)}\,(1-2\,v_{j_1}^2\,p^2) + 2\,\rho^{(2)}\,v_{j_2}^2\,p^2 \\
d &= 2\,(\rho^{(2)}\,v_{j_2}^2 - \rho^{(1)}\,v_{j_1}^2)\,. \qquad (2.14)
\end{aligned}
$$

Equations similar to expression (2.12) have been derived by Aki and Richards (1980) for all reflection and transmission coefficients in isotropic media. Energy partitioning problems for elastic and acoustic waves at solid/solid, solid/fluid and fluid/fluid boundaries and free surfaces are also discussed in many other publications (Musgrave, 1970; Červený & Ravindra, 1971; Brekhovskikh, 1980; Tsvankin, 1995b).

2.3 Approximations and their assumptions

To find the reflection and transmission coefficients, we need to solve a system of kinematic and dynamic boundary conditions, with the dimension of the system depending on the symmetry of the media and the number of the wave modes above and below a reflecting interface. The inverse problem of estimating medium parameters from the angular changes of the reflection response represents a much more difficult problem. Koefoed (1955) went through the laborious exercise of numerically investigating reflection coefficients for many different sets of elastic parameters of isotropic models. He established "rules" to describe the behavior of his many computed curves, without stimulating any major advance in amplitude studies at his time. Obviously, extending his approach to azimuthally anisotropic media (exploring an even higher-dimensional parameter space) is not feasible. Instead, as shown below, it is more helpful to derive approximate scattering coefficients and learn about the influence of the anisotropy parameters on the reflection response.

After his laborious hand-calculations of reflection coefficients for many different combinations of medium parameters, Koefoed (1955) was the first to suggest that there is an invertible relationship between the reflection coefficient as a function of incidence angle and the medium parameters. Specifically, he wrote that

> ... in a more remote future it may be possible to draw conclusions concerning the lithologic nature of rock strata from the shape of the reflection coefficient curves ... *Koefoed*

Of particular importance was his observation that the changes of the reflection coefficient with incidence angle depend strongly on variations in Poisson's ratio. Koefoed's prediction came true in 1982, when Ostrander pioneered a new era in amplitude-versus-offset analysis at the 52nd International Meeting of Exploration Geophysicists.

> ... Embedding a low velocity gas sand into sediments having 'normal' Poisson's ratios should result in an increase in reflected *P*-wave energy with angle of incidence ... *Ostrander*

The relationship between reflection coefficients and velocities and densities is not readily obvious in equations (2.12), (2.13) and (2.14). These equations, for example,

do not allow one to predict the influence of a particular parameter on the reflection response. Therefore, to reveal the information content contained in the reflected amplitudes, it is useful to study analytical approximations. Several such approximations, differing in accuracy, medium and wavefield parameterizations, have been derived. While these approximations are based on different philosophies of interpretation and physical understanding, they share the same basic assumptions that have proved very useful in AVO studies:

- The media on both sides of the reflecting boundary have similar elastic properties, and the relative changes in P- and S-wave velocities and density are small across the interface.
- The incidence angles are sufficiently smaller than the critical angle. At the critical angle, the amplitudes change abruptly and phase changes make any parameter extraction very difficult.

The first approximation of this type was provided by Bortfeld (1961), who partially linearized the reflection coefficient with respect to changes in medium parameters. Subsequently, analytic approximations were given in Richards and Frasier (1976) and Aki and Richards (1980). Bortfeld's (still very cumbersome) approximation was later modified by Hilterman (1983), who showed that Bortfeld's approximation can be approximately represented as a sum of a "fluid" term and a "shear-wave" term. Other simplifications based on the assumption of $V_P/V_S = 2$ (Wiggins *et al.*, 1983) or constant density (Hilterman, 1983) further reduced the complexity, albeit with the risk of severely misinterpreting the results if the restrictive assumptions are not justified.

A particularly attractive representation of the reflection coefficient was derived by Shuey (1985). Shuey rewrote the approximate P-wave reflection coefficient presented in Aki and Richards (1980) in the form

$$\mathrm{R}_P^{\mathrm{iso}}(i) = \mathrm{A} + \mathrm{B}\sin^2 i + \mathrm{C}\sin^2 i \tan^2 i \; . \tag{2.15}$$

As discussed in more detail in Castagna & Backus (1993), the main advantage of this representation is that each term is responsible for a different angular range. The coefficient A is the normal-incidence reflection coefficient, while B describes the initial slope of the reflection-coefficient curve. B is the so-called "AVO gradient" that is nowadays routinely extracted from seismic data. The larger-angle term C becomes important for incidence angles larger than 20 degrees and is often referred to as the "curvature term". Recovery of this term is difficult, but it can provide useful additional information. For instance, it can be used to distinguish between high and low gas saturations in particular plays (Castagna & Backus, 1993).

The individual terms in Shuey's approximation [equation (2.15)] have the following form:

$$\mathrm{A} \;=\; 1/2 \left(\frac{\Delta V_P}{\bar{V}_P} + \frac{\Delta \rho}{\bar{\rho}} \right) = 1/2 \frac{\Delta Z}{\bar{Z}}$$

$$\begin{aligned} \mathrm{B} &= -2\left(1-\frac{\bar{\sigma}}{1-\bar{\sigma}}\right)\mathrm{A}-\frac{1}{2}\frac{1-3\bar{\sigma}}{1-\bar{\sigma}}\frac{\Delta V_P}{\bar{V}_P}+\frac{\Delta\sigma}{(1-\bar{\sigma})^2} \\ \mathrm{C} &= 1/2\,\frac{\Delta V_P}{\bar{V}_P}\,, \end{aligned} \tag{2.16}$$

where σ denotes Poisson's ratio and V_P is the P-wave velocity. In equation (2.16), the elastic properties are conveniently expressed as functions of the average values and relative differences in the model parameters. The P-wave impedance $Z = \rho V_P$ in the upper and lower layers, for example, can be written as functions of its average value $\bar{Z} = 1/2\,(Z^{(1)} + Z^{(2)})$ and the difference $\Delta Z = Z^{(2)} - Z^{(1)}$:

$$\begin{aligned} Z^{(1)} &= \bar{Z}\,(1-\frac{1}{2}\frac{\Delta Z}{\bar{Z}})\,, \\ Z^{(2)} &= \bar{Z}\,(1+\frac{1}{2}\frac{\Delta Z}{\bar{Z}})\,. \end{aligned}$$

The assumptions of small discontinuities in elastic parameters hence translate into

$$|\frac{\Delta Z}{\bar{Z}}| << 1\,. \tag{2.17}$$

Analogous expressions are defined for the relative changes in compressional velocity and density. Shuey (1985) suggested two different choices for angle i. First, i can be chosen as the average of the incidence and transmission angles, i.e. $i = 1/2\,(i_1 + i_2)$; or, alternatively, i can be identified with the incidence angle i_1. He states that the difference in accuracy between both choices is small for angles smaller than 30 degrees.

A more instructive and often used version of Shuey's approximation is given by Hilterman (1983)

$$\mathrm{R}_P^{\mathrm{iso}}(i) = A\cos^2 i + 2.25\,\Delta\sigma\sin^2 i\,, \tag{2.18}$$

with A given in equation (2.16). While this relation is certainly easy to interpret, it has to be treated with caution: the additional assumption used in deriving equation (2.18) is that $\bar{\sigma} = 1/3$, or, equivalently, $\bar{V}_P/\bar{V}_S = 2$. This relation is rather typical, but certainly not true, for all exploration targets.

The goal of conventional AVO analysis is the extraction of information about physical properties (and in particular on shear-wave velocities) from amplitude changes with offset of the reflected compressional wavefield. The gradient term in equation (2.15) is not easily interpretable in terms of shear-wave velocities or (equivalently) Poisson's ratio of the upper and lower media. The approximation that is probably best suited for analyzing the contrast in elastic parameters was suggested by Wright (1986) and first published in this form by Thomsen (1990). Fully linearized in the small contrasts in the elastic properties and without any additional assumption [such as the V_P/V_S-ratio in equation (2.18)], the approximate reflection coefficient can be written

in the form

$$R_P^{iso}(i) = 1/2\frac{\Delta Z}{\bar{Z}} + 1/2\left\{\frac{\Delta V_P}{\bar{V}_P} - \left(\frac{2\bar{V}_S}{\bar{V}_P}\right)^2 \frac{\Delta G}{\bar{G}}\right\}\sin^2 i + 1/2\frac{\Delta V_P}{\bar{V}_P}\sin^2 i \tan^2 i. \quad (2.19)$$

Because of the transparent and concise form and the clear definition of the assumptions behind them, I will use "Thomsen-style" approximations for different anisotropic media throughout this thesis. In addition to being much more compact and comprehensive, this equation also has the advantage of explicitly using the difference in shear modulus $G = \rho V_S^2$ in its parameterization. From the Biot-Gassmann theory on the effects of pore fluids on rock velocities, it follows that gas charging a rock does not change its shear modulus, and $\frac{\Delta G}{\bar{G}}$ vanishes for fluid-contact interfaces within a rock unit (Wright, 1986; Thomsen, 1990).

A test of equation (2.19) for three models representing different exploration targets is shown in Figure 2.3. Gas-sand AVO anomalies have been divided into three distinguished types by Rutherford and Williams (1989):

Class 1 The normal-incidence *P*-wave reflection coefficient is strongly positive, and the reflection amplitude decreases with offset.

Class 2 Small *P*-wave reflection coefficients, with a large relative amplitude change with offset.

Class 3 Large negative reflection coefficients that become even more largely negative with offset.

The model parameters used in this study are shown in Table 2.1, taken from Kim et. al. (1993). The first model is a Class 1 reflection from the Pennsylvanian Hartshorn formation in the Arkoma Basin. Model 2 corresponds to sediments offshore Louisiana and represents a Class 2 reflection. Model 3 shows parameters computed for Upper Pliocene Delta Front sediments. To challenge the accuracy of equation (2.19), the model parameters have significant relative changes in elastic properties across the boundary. Specifically, the differences in shear velocities and shear modulus are very large in the first two models, which, strictly speaking, violates the assumptions behind approximation (2.19). Nonetheless, as shown in Figure 2.3, the approximations [using the incidence angle as input to equation (2.19), i.e., $i \equiv i_1$] provide a close match to the exact solutions.

Shuey's and Thomsen's approach to linearizing the reflection coefficients can also be extended to shear-waves. The linearized reflection coefficient for the SH–wave mode (polarized perpendicular to the vertical propagation plane) yields

$$R_{SH}^{iso} = -1/2\left(\frac{\Delta\rho}{\bar{\rho}} + \frac{\Delta V_S}{\bar{V}_S}\right) + 1/2\frac{\Delta V_S}{\bar{V}_S}\sin^2 j +$$

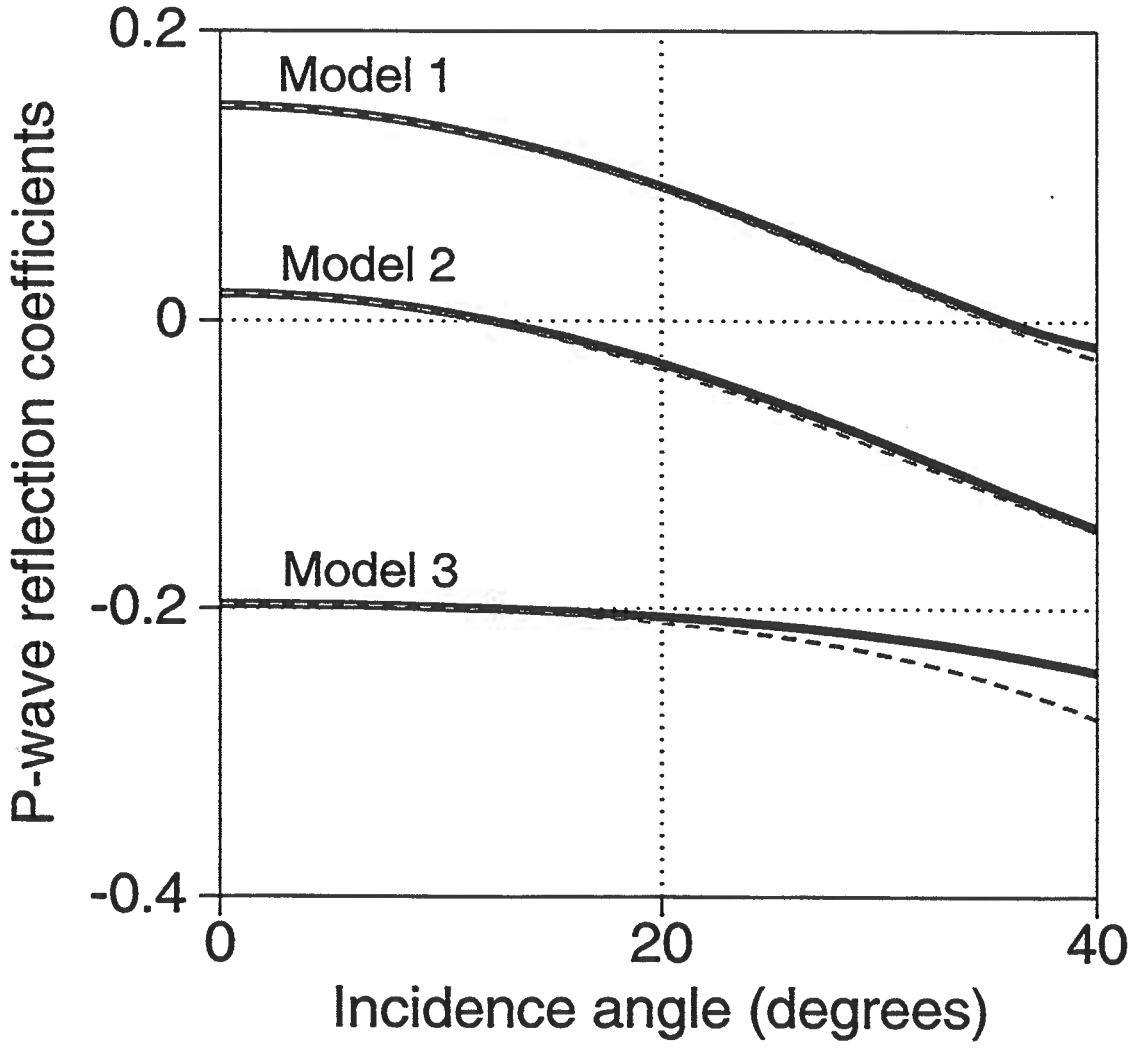

FIG. 2.3. *P*-wave reflection coefficients computed for reflections from three different shale/gas-sand interfaces. The solid lines denote the exact solutions and the dashed lines show the approximations. The model parameters are given in Table 2.1.

	Model 1		Model 2		Model 3	
	shale	sand	shale	sand	shale	sand
V_P	3.30	4.20	2.96	3.49	2.73	2.02
V_S	1.70	2.70	1.38	2.29	1.24	1.23
ρ	2.35	2.49	2.43	2.14	2.35	2.13
σ	0.319	0.148	0.361	0.122	0.370	0.205
$\frac{\Delta Z}{\bar{Z}}$	0.297		0.038		-0.394	
$\frac{\Delta V_P}{\bar{V}_P}$	0.240		0.164		-0.298	
$\frac{\Delta \rho}{\bar{\rho}}$	0.058		-0.127		-0.098	
$\frac{\Delta V_S}{\bar{V}_S}$	0.454		0.496		-0.008	
$\frac{\Delta G}{\bar{G}}$	0.911		0.832		-0.114	
$(2v_s/v_p)^2$	1.376		1.295		1.081	
$\Delta\sigma$	-0.172		-0.239		-0.164	

Table 2.1. Model parameters for Class 1, Class 2 and Class 3 AVO anomalies.

$$1/2\,\frac{\Delta V_S}{\bar{V}_S}\,\sin^2 j\,\tan^2 j\,, \tag{2.20}$$

or, equivalently,

$$\mathrm{R}_{SH}^{\mathrm{iso}} = -1/2\left(\frac{\Delta\rho}{\bar{\rho}} + \frac{\Delta V_S}{\bar{V}_S}\right) + 1/2\,\frac{\Delta V_S}{\bar{V}_S}\,\tan^2 j\,, \tag{2.21}$$

with j denoting the incidence shear-wave angle. The disadvantage of equation (2.21) is that the approximation is not exact for normal incidence. The difference between the vertical-incidence reflection coefficients of different modes will later be attributed to the contribution of (small) anisotropic parameters, and any inaccuracy due to the isotropic approximation can hamper the analysis and inversion for anisotropy coefficients. Therefore, I suggest introducing the shear-wave impedance $Z^S = \rho\beta$ and using the exact normal-incidence reflection coefficient in equation (2.21):

$$\mathrm{R}_{SH}^{\mathrm{iso}} = -1/2\,\frac{\Delta Z^S}{\bar{Z}^S} + 1/2\,\frac{\Delta V_S}{\bar{V}_S}\,\tan^2 j\,. \tag{2.22}$$

From the physical point of view, it is clear that the normal-incidence reflection coefficient in isotropic media is the same for any shear mode because the polarization vector is always parallel to the reflecting interface. For oblique incidence angles, SV-waves generate reflected and transmitted P-waves in addition to shear (SV)-waves, and it is not surprising that the angular variation of the SV-wave reflection coefficient differs

from that in equation (2.22) (Thomsen, 1988; Thomsen, 1993):

$$R_{SV}^{iso} = -1/2\frac{\Delta Z^S}{\bar{Z}^S} + \left(\frac{7}{2}\frac{\Delta V_S}{\bar{V}_S} + 2\frac{\Delta\rho}{\bar{\rho}}\right)\sin^2 j - 1/2\frac{\Delta V_S}{\bar{V}_S}\sin^2 j\tan^2 j\,. \quad (2.23)$$

It is well known that the coupling between transverse and longitudinal waves for oblique incidence angles manifests itself in the dependence of the *P*-wave AVO gradient on the shear-wave velocity (Shuey, 1985). Surprisingly, the opposite is not the case, and the *SV*-wave AVO gradient is independent of the compressional wave velocities under the assumption of small relative changes in the elastic parameters across the reflecting boundary[1].

Equation (2.23), as well as most reflection-coefficient approximations in this paper, shows a simple decomposition of the form (2.15). Here, it is appropriate to make some observations for the particular case of shear-wave amplitude studies. Even more so than for conventional *P*-wave AVO studies, shear-wave AVO analysis is limited to the extraction of the AVO gradient term. Small incidence angles are particularly important for shear-wave studies because the first critical angle is often small. Even moderate incidence angles of about 20° can generate evanescent energy that causes complicated phase and amplitude distortions. Thus, for shear waves, it is often impossible to obtain reliable estimates of the C-term ($C = 1/2\frac{\Delta V_S}{V_S}$) in equation (2.15).

As in the *P*-wave case, the simplicity of the linearized equations helps to quickly identify the contributions of different physical parameters to the reflection response. For instance, we are reminded that only relative differences in elastic parameters influence the reflected seismic signature. For the particular case of the *SH*-wave reflection coefficient, equation (2.21) shows that the relative differences in density and shear-wave velocity have the same influence on the normal-incidence reflection coefficient. Additionally, we recognize that $\frac{\Delta V_S}{V_S}$ is the only term responsible for small- and large-angle variations of the *SH*-wave reflection response. Thus, if amplitudes of *SH*-waves incident at moderate and large angles (> 20°) can be reliably recovered, it is advantageous to plot them as a function of the squared tangent of the incidence angle [see equation (2.21)].

Figures 2.4 and 2.5 show approximate and exact reflection coefficients for *SV*- and *SH*-waves computed for the models shown in Table 2.1. The approximations in Figure 2.4 are computed using equation (2.23), while Figure 2.5 was generated using equation (2.22). The accuracy is satisfactory for all models, especially if one takes into account the significant difference in the shear-wave velocity across the reflecting boundary (Model 1 and Model 2).

[1]The approximate *P*-*P*-transmission coefficient is also independent of the shear-wave velocities. Apparently, *P*-wave AVO is based on a rare physical gratitude.

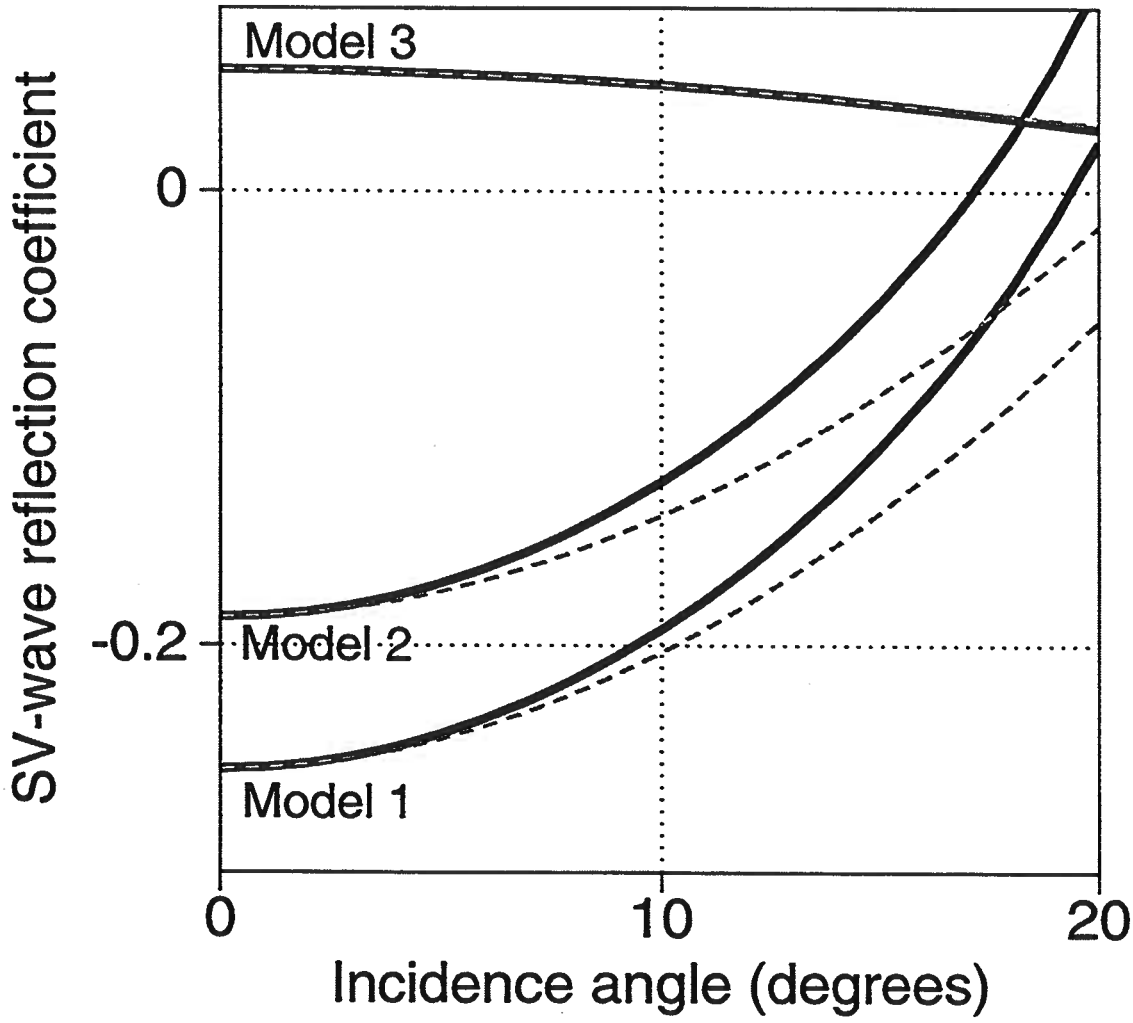

FIG. 2.4. *SV*-wave reflection coefficients computed for reflections from three different models of gas sands. The solid lines denote the exact solution. The dashed lines show the approximations computed using equation (2.23). The models (parameters are given in Table 2.1) have a significant difference in the shear-wave velocity across the boundary.

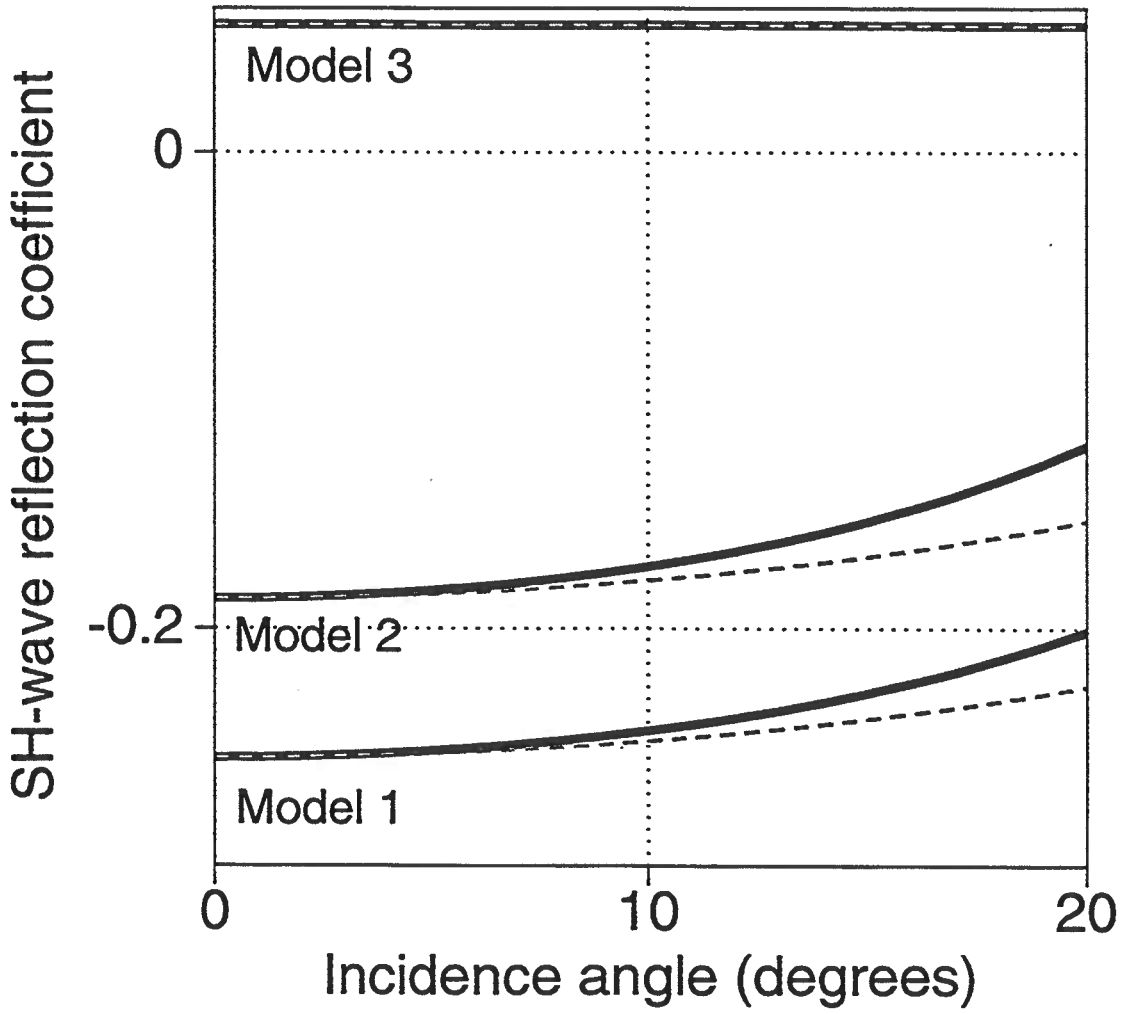

FIG. 2.5. *SH*-wave reflection coefficients computed for reflections from three different shale/gas sand interfaces. The solid lines denote the exact solution. The dashed lines show the approximations computed using equation (2.22). The model parameters are given in Table 2.1. As predicted in equation (2.22), the first two models with positive $\frac{\Delta V_S}{V_S}$ yield positive AVO gradients. Model 3 shows a reflection response independent of the incident angle due to the small value of $\frac{\Delta V_S}{V_S}$.

Chapter 3

REFLECTION AND TRANSMISSION FOR VERTICAL TRANSVERSE ISOTROPY

If the seismic velocities in a medium are angle-dependent, the behavior of elastic waves becomes much more complicated than in the isotropic case. In this chapter, I review and visualize important kinematic and dynamic features of wavefields in the simplest anisotropic model: a transversely isotropic homogeneous medium with a vertical axis of symmetry. In addition, I also refine the published approximation to the *P*-wave reflection coefficient in VTI media (Thomsen, 1993).

3.1 Wave propagation and notation for VTI media

A rigorous mathematical description of wave propagation in VTI media can be found in Musgrave (1970). The key step in his treatment is the substitution of the displacement field **u** of a harmonic plane wave

$$\mathbf{u} = \begin{pmatrix} U_1 \\ U_2 \\ U_3 \end{pmatrix} e^{i(k_j x_j - \omega t)} \tag{3.1}$$

into the equation of motion

$$\rho u_{i,tt} = f_i + \tau_{ij,j} \,. \tag{3.2}$$

Equation (3.2) is derived and discussed, for example, in Aki and Richards (1980); the subscript $(,tt)$ denotes the second temporal derivative and $(,_j)$ indicates the partial derivative with respect to the j-th coordinate. The wave vector $(k_1, k_2, k_3)^T$ can be rewritten in terms of the wavefront normal $(n_1, n_2, n_3)^T$ and the frequency ω:

$$k_j = \frac{\omega}{v} n_j \,.$$

The Christoffel system

$$c_{ijkl}\, n_j\, n_l\, U_k \; - \; \rho v^2 U_i = 0 \,, \tag{3.3}$$

which will be discussed in more detail in subsequent chapters can be obtained from equations (3.1) and (3.2), along with the Hook's law relationship between stress and strain. Equation (3.3) is a familiar eigenvector/eigenvalue problem that can be solved by well-known classical methods. For example, the roots of the characteristic equation (Christoffel equation)

$$\det \left| \, c_{ijkl}\, n_j n_l \; - \rho v^2 \, \delta_{ik} \, \right| = 0 \,, \tag{3.4}$$

where δ_{ik} denotes the Kronecker-delta symbol:

$$\delta_{ik} \equiv \begin{cases} 1 & \text{if } i = k \\ 0 & \text{if } i \neq k \end{cases} ,$$

yield the velocities of the three wave modes as a function of the direction of the wavefront normal.

In VTI media, equation (3.4) simplifies significantly. The three eigenvalues (velocities) are given in White (1983) as a function of the angle θ with the vertical and the five independent stiffness components $c_{11}, c_{33}, c_{55}, c_{66}$ and c_{13}:

$$\rho V_{SH}^2 = c_{66} \sin^2\theta + c_{55} \cos^2\theta ; \tag{3.5}$$

$$2\rho V_{SV}^2 = (c_{11} + c_{55}) \sin^2\theta + (c_{33} + c_{55}) \cos^2\theta - \mathrm{K} ; \tag{3.6}$$

$$2\rho V_P^2 = (c_{11} + c_{55}) \sin^2\theta + (c_{33} + c_{55}) \cos^2\theta + \mathrm{K} , \tag{3.7}$$

with

$$\mathrm{K} = \sqrt{\left((c_{11} - c_{55}) \sin^2\theta - (c_{33} - c_{55}) \cos^2\theta\right)^2 + 4(c_{13} + c_{55})^2 \sin^2\theta \cos^2\theta} .$$

The symmetry of equation (3.3) ensures that for any given phase angle, the polarization vectors U_i of SH-, (quasi) SV- and (quasi) P-waves are mutually orthogonal. However, only the polarization of the SH-wave is strictly orthogonal to the propagation direction while the polarization vectors of the remaining waves are not strictly longitudinal and transverse (Musgrave, 1970; White, 1983).

Expressions stated as a function of stiffness coefficients such as equations (3.5), (3.6) and (3.7) are well suited for numerical computations. On the other hand, they are not very convenient for analyzing the behavior of seismic signatures in different angular ranges. For example, it would be beneficial for surface seismic applications to have a parameter responsible for the shape of the phase velocity curves near vertical. Moreover, expressions in c_{ij} notation are not very helpful in quickly evaluating the magnitude of anisotropy and in separating the influence of anisotropy on the seismic response.

These difficulties motivated Thomsen (1986) to introduce a new set of anisotropy coefficients for VTI media. He suggested replacing the five independent stiffness components by two vertical velocities and three dimensionless anisotropy parameters:

$$V_{P0} \equiv \sqrt{c_{33}/\rho} \tag{3.8}$$

$$V_{S0} \equiv \sqrt{c_{55}/\rho} \tag{3.9}$$

$$\gamma \equiv \frac{c_{66} - c_{55}}{2c_{55}} \tag{3.10}$$

$$\epsilon \equiv \frac{c_{11} - c_{33}}{2c_{33}} \tag{3.11}$$

$$\delta \equiv \frac{(c_{13}+c_{55})^2-(c_{33}-c_{55})^2}{2c_{33}(c_{33}-c_{55})} . \tag{3.12}$$

V_{P0} and V_{S0} are the vertical velocities of P-waves and shear waves, respectively. Note that both shear waves have the same vertical velocity, as can be seen by setting $\theta = 0$ in equations (3.5) and (3.6). SH-wave propagation is completely described by parameters V_{S0} and γ while P-wave and SV-wave propagation depends on four parameters: V_{P0}, V_{S0}, ϵ and δ. Anisotropy parameters ϵ, δ and γ are dimensionless and go to zero in isotropic media.

The phase-velocity equations (3.5), (3.6) and (3.7) as well as expressions for other seismic signatures can be rewritten in terms of Thomsen's parameters. Tsvankin (1996b) shows that these parameters are also perfectly suitable to describe wave propagation in VTI media of any strength of anisotropy. Obtaining the corresponding expressions for isotropic media (with velocities V_{P0} and V_{S0}) can then be achieved by simply setting the anisotropy coefficients ϵ, δ and γ to zero. Elliptical anisotropy (i.e., a medium with elliptical slowness surfaces and elliptical wavefronts) is introduced by setting $\epsilon = \delta$. Moreover, one of the advantages of Thomsen's notation is the simplification achieved by considering the limit of weak anisotropy, for which the dimensionless anisotropy parameters are small in magnitude ($|\epsilon|, |\delta|, |\gamma| << 1$). This assumption is justified by the observation that most rocks exhibit small values of the anisotropy coefficients (< 0.2), if probed by waves in the frequency band typically used in seismic exploration [see Table 1 in Thomsen (1986)].

Using the assumption of weak anisotropy, the phase velocities of waves propagating in VTI media can be linearized in the anisotropy coefficients ϵ, δ and γ (Thomsen, 1986):

$$V_P(\theta) = V_{P0}\left[1+\delta\sin^2\theta\cos^2\theta+\epsilon\sin^4\theta\right] ; \tag{3.13}$$

$$V_{SV}(\theta) = V_{S0}\left[1+\frac{V_{P0}^2}{V_{S0}^2}(\epsilon-\delta)\sin^2\theta\cos^2\theta\right] ; \tag{3.14}$$

$$V_{SH}(\theta) = V_{S0}\left[1+\gamma\sin^2\theta\right] . \tag{3.15}$$

Equations (3.13)-(3.15) explain the influence of anisotropy on seismic wavefields in a concise analytical way. Here, I want to additionally visualize some of the differences between isotropic and anisotropic wavefields. Because rays correspond to the trajectory of high-frequency energy, the behavior of the wavefield can be conveniently characterized and described by displaying the raypaths and points along the raypaths at equal traveltimes (i.e., wavefronts). Figure 3.1 shows rays traced from a point source embedded in a homogeneous medium with the vertical P-wave velocity $V_{P0} = 2.6\,\mathrm{km/s}$ and vertical shear velocity $V_{S0} = 2.0\,\mathrm{km/s}$. The anisotropy simulated in this model is described by the parameters $\epsilon = 0.15$ and $\delta = -0.1$. The surface formed at propagation time $t = 0.75\,\mathrm{s}$ by arrivals of the P-wave is indicated by a white continuous line. The black lines emitted from the source at 2.5-km horizontal

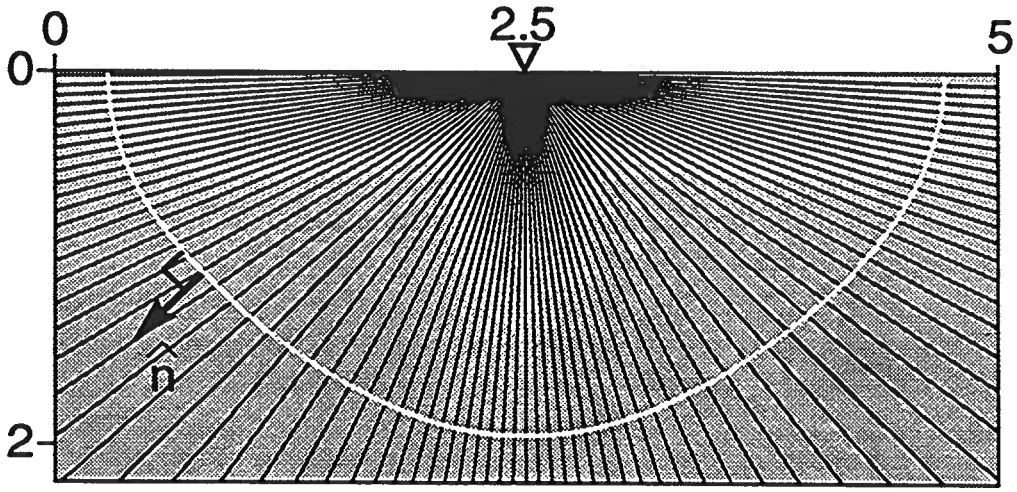

FIG. 3.1. Vertical section showing P-wave propagation in a homogeneous VTI medium. Shown are rays traced from a point source at 2.5 km lateral position. The white continuous contour denotes a wavefront at $t = 0.75\,\mathrm{s}$ propagation time. Note that, in general, the normal $\hat{n}$ to the wavefront does not coincide with the ray direction.

position denote seismic rays. Several features of Figure 3.1 differ significantly from the familiar behavior of rays and wavefronts in isotropic homogeneous media. For example, the wavefront is not circular. In particular, the P-wavefront is more advanced in the horizontal direction than in the vertical direction. From the definition of ϵ, one can show that

$$\epsilon \approx \frac{V_P(\theta = 90^\circ) - V_{P0}}{V_{P0}}; \tag{3.16}$$

hence, one can estimate ϵ by simply comparing the horizontal and vertical advance of the P-wave wavefronts. Let us now discuss P-wave propagation close to vertical in more detail. From equation (3.13), it is obvious that δ is responsible for the P-wave propagation near vertical. A decrease in velocity, as indicated by the reduced advance of the wavefront in Figure 3.1 is caused by a negative value of δ. A concentration of rays is seen in the horizontal and vertical directions for the P-wave. Figure 3.1 not only describes the geometrical position of the wavefront at a specific time, it also indicates the dynamic properties of the wavefield. More specifically, the ray density makes visual the phenomena of energy focusing and defocusing (Tsvankin & Chesnokov, 1990; Tsvankin, 1995a). Energy increases in regions with high concentration of rays (or, equivalently, a high concentration of group velocity vectors). Conversely, a low concentration of rays indicates energy defocusing.

The degree of anisotropy is commonly characterized by the absolute value of Thomsen's parameters ϵ and δ. Figure 3.2a shows rays and wavefronts for Green River Shale, a medium that can be considered to be moderately to strongly anisotropic

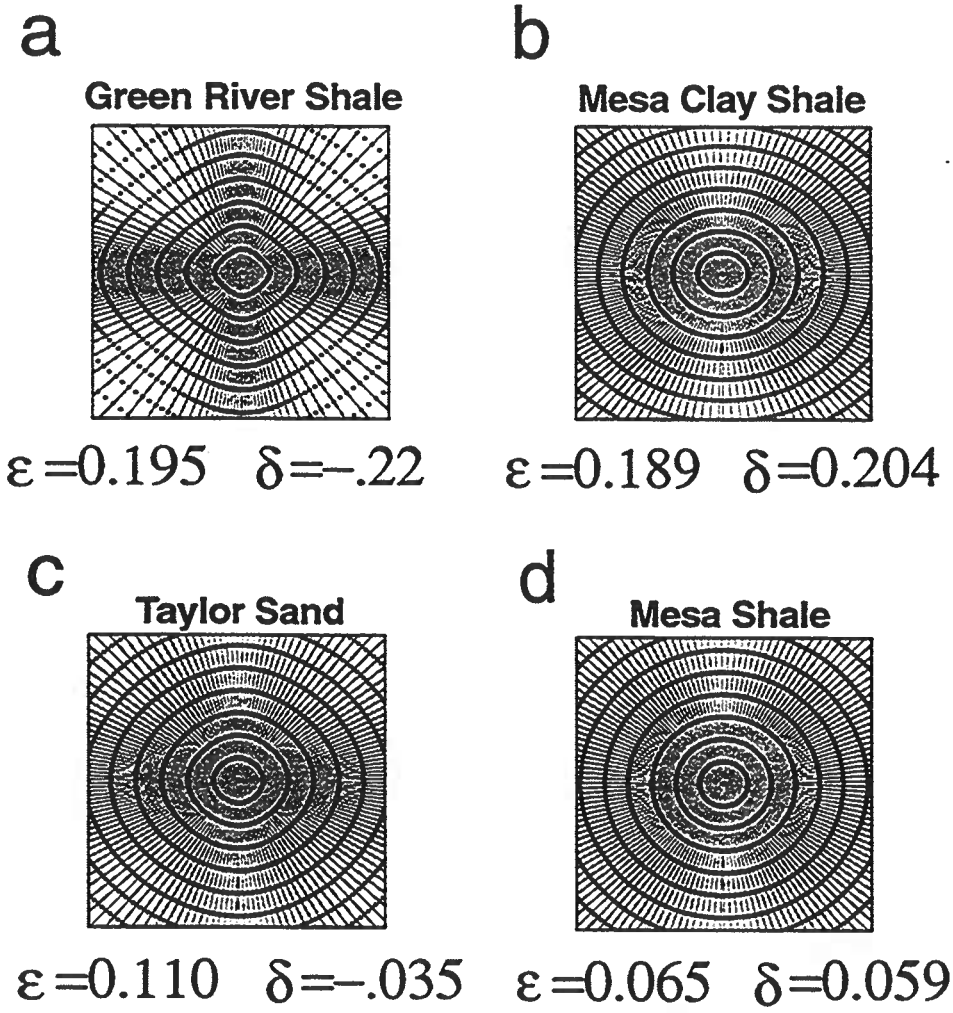

FIG. 3.2. Vertical sections showing rays and wavefronts for P-wave propagation in homogeneous anisotropic models. (a) $V_{P0} = 3.33\,\mathrm{km/s}$; (b) $V_{P0} = 3.79\,\mathrm{km/s}$; (c) $V_{P0} = 3.37\,\mathrm{km/s}$; (d) $V_{P0} = 3.38\,\mathrm{km/s}$.

($\epsilon = 0.195, \delta = -0.22$). The spatial dimension of the model is 1 km × 1 km. Nine wavefronts, uniformly sampled in time, are displayed. *P*-waves for a medium with similar absolute values of ϵ and δ ($\epsilon = 0.189, \delta = 0.204$) are shown in Figure 3.2b. Figures 3.2c and 3.2d illustrate wave propagation in media with moderate anisotropy ($|\epsilon| < 0.2, |\delta| < 0.2$). For AVO analysis where the overburden has VTI anisotropy, it is important to understand the influence of anisotropy on the radiation pattern. The angular energy distribution is not correlated with the absolute values of ϵ and δ. In fact, the shape of the energy radiation pattern is much more controlled by the difference between ϵ and δ than by the individual values of the anisotropic coefficients (Tsvankin, 1995a). This explains why the ray-density distribution is significantly more uniform for the Mesa Clay Shale than for Green River Shale (see Figures 3.2a and 3.2b). Note that the more weakly anisotropic Taylor Sandstone exhibits more pronounced angular changes in ray-density than does the "stronger" anisotropic material Mesa Clay Shale. In other words, the common notion of weak anisotropy is meaningless when talking about the shape of the radiation pattern. As a general rule, for $(\epsilon - \delta) < 0$, one can expect increasing *P*-wave amplitude away from vertical. The maximum energy concentration is obtained approximately at 45 degrees from vertical; then the energy decreases sharply towards horizontal. Conversely, for $(\epsilon - \delta) > 0$ (the most common case), transverse isotropy causes *P*-wave amplitudes to decrease away from the symmetry axis, with a minimum of energy density near 45 degrees, followed by a sharp increase when approaching the horizontal. An analytic and quantitative analysis of *P*-wave amplitude patterns can be found in (Tsvankin, 1995a).

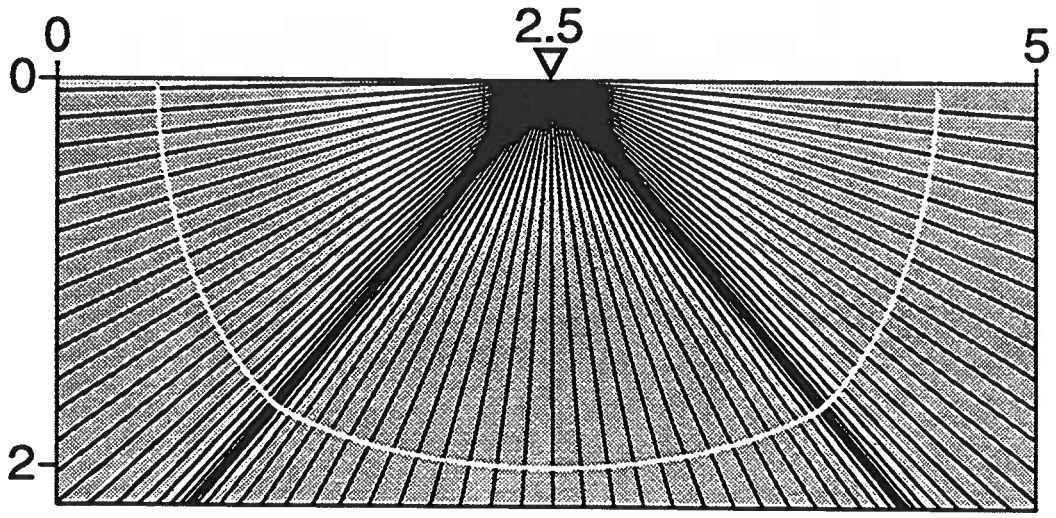

FIG. 3.3. *SV*-wave propagation in a homogeneous VTI medium. Shown are rays traced from a point source at 2.5 km lateral position. The white continuous contour denotes a wavefront at $t = 1.0$ s propagation time. The wavefront has the same vertical and horizontal distance from the source, i.e., $V_{SV}(0°) = V_{SV}(90°)$.

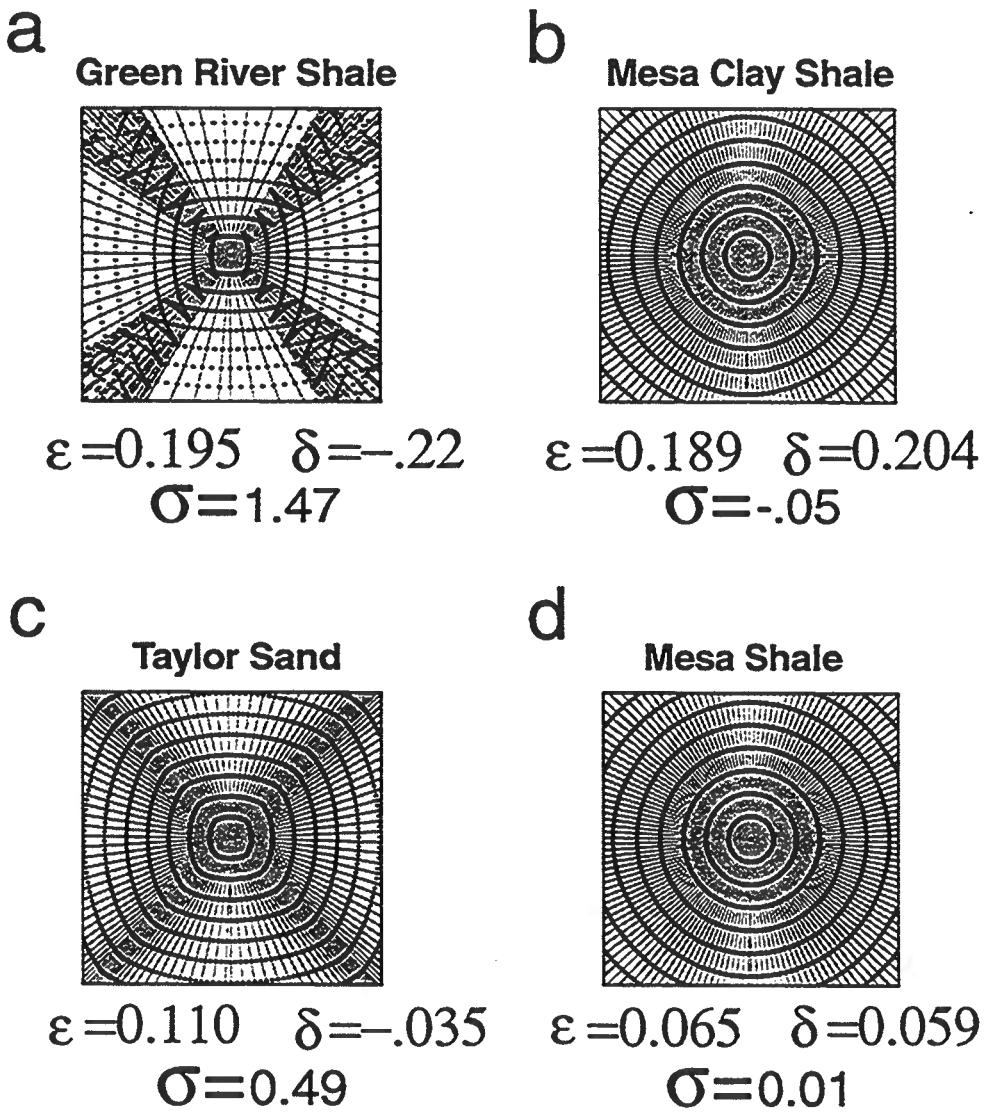

FIG. 3.4. Vertical sections showing rays and wavefronts for *SV*-wave propagation in homogeneous anisotropic models. (a) $V_{P0} = 3.33\,\text{km/s}$, $V_{S0} = 1.77\,\text{km/s}$; (b) $V_{P0} = 3.79\,\text{km/s}$, $V_{S0} = 2.07\,\text{km/s}$; (c) $V_{P0} = 3.37\,\text{km/s}$, $V_{S0} = 1.83\,\text{km/s}$; (d) $V_{P0} = 3.38\,\text{km/s}$, $V_{S0} = 2.44\,\text{km/s}$.

Figure 3.3 shows SV-rays and the SV-wavefront at $t = 1\,\mathrm{s}$ traveltime for the same model as in Figure 3.1. The influence of anisotropy on SV-wave propagation is even more pronounced than that on the P-wave propagation in Figure 3.1. First, the wavefronts are clearly non-circular and have rhombic appearance. A sharp increase of ray density is visible at about 45°. The same focusing of rays can be observed for Taylor Shale (Figure 3.4c), while the wavefront of the Green River shale (Figure 3.4a) is clearly triplicated. Again, as obvious by comparison with the wavefront snapshots of Mesa Clay Shale and Mesa Shale (Figures 3.4b and 3.4d), is not the absolute value of ϵ or δ that determines the shape and energy distribution of the wavefield. Tsvankin and Thomsen (1994) and Tsvankin (1995a) found that the most important factor describing the phase velocity and energy radiation of SV-waves is a combination of anisotropic parameters and the ratio of the vertical velocities, denoted by σ.

$$\sigma \equiv \frac{V_{P0}^2}{V_{S0}^2}(\epsilon - \delta) \tag{3.17}$$

A more detailed qualitative analysis of the relation between cusp sizes and σ is given in Rüger (1996)

SH wave propagation is simulated in Figure 3.5. The wavefront is elliptical, with semi-axes determined by $V_{SH}(\theta = 0°)$ and $V_{SH}(\theta = 90°)$. From the definition of γ [equation (3.10)], it follows that

$$\gamma \approx \frac{V_{SH}(\theta = 90°) - V_{S0}}{V_{S0}}, \tag{3.18}$$

For positive values of γ (the most common case), the SH-wavefront is more advanced horizontally than vertically. Additionally, only very minor distortions in ray density are visible (Tsvankin, 1995a).

3.2 Reflection and transmission at horizontal interfaces – exact expressions

The angular dependence of velocity will obviously influence the reflection coefficient. For reflections off the top of a VTI layer, it is easy to recognize that the reflection coefficients and the AVO response are azimuthally invariant; i.e., for a given angle of incidence, the reflection response does not vary with azimuth (measured with respect to the x_1-axis). This is true for both isotropic and VTI layers above and below the reflector. Furthermore, one has to consider only the coupling of P- and SV-waves at the interface. The third mode, the SH-wave, is polarized perpendicular to the incidence plane and is fully decoupled from P- and SV-waves. Thus, the continuity requirements at a plane horizontal interface lead to four boundary conditions that determine the transmission and reflection coefficients for the P- and SV-waves.

Reflection and transmission in anisotropic media was first discussed in Henneke (1972) and Keith and Crampin (1977). An exact algebraic solution to the VTI

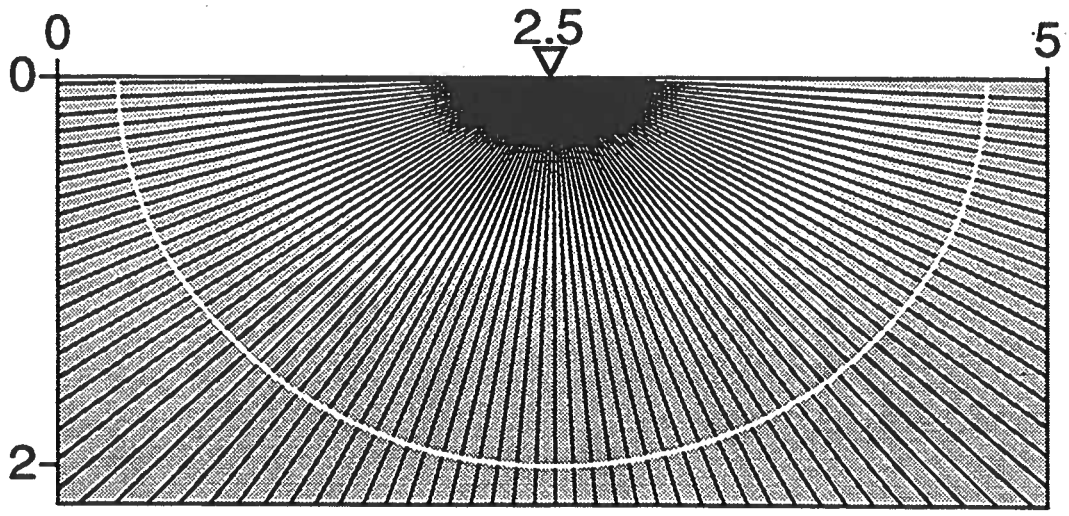

FIG. 3.5. Vertical section showing *SH*-wave propagation in a homogeneous VTI medium. The wavefront is shown for $t = 1.0\,\mathrm{s}$ propagation time. *SH*-anisotropy is elliptical and the wavefront forms an ellipse.

reflection/transmission problem has been developed by Daley and Hron (1977). Unfortunately, I find their derivations very cumbersome to reproduce. A different analytic expression, although not expressed in a concise form, has been derived by Graebner (1992). Graebner's approach is particularly attractive because the reflection and transmission coefficients are parameterized as a function of the horizontal slowness (the ray parameter p), which is preserved during the reflection and transmission process as a consequence of Snell's law. Using p as the argument is very convenient for numerical computations. First, many reflectivity programs are parameterized in horizontal slowness; similarly, ray-tracing algorithms in stratified media use the preservation of horizontal slowness for each individual ray for efficient computation. Secondly, trigonometric functions that are time-consuming to evaluate numerically are completely avoided. This is not the case if the scattering coefficients are evaluated as functions of phase or group angles. Finally, as will become obvious in the next chapter, Graebner's solution can be easily extended to transversly isotropic media with a horizontal axis of symmetry.

The following is a modified representation of Graebner's solution to the VTI reflection coefficient (see Graebner, 1992) in c_{ij}-notation. Because of the azimuthal invariance of the reflection coefficient, it is sufficient to limit the derivation to the $[x_1, x_3]$-plane. The Christoffel equation (3.4) can be written as a function of the horizontal slowness p and vertical slowness q (with $p^2 + q^2 = 1/v^2$) as

$$\det \begin{vmatrix} c_{11}p^2 + c_{55}q^2 - \rho & (c_{13} + c_{55})p\,q \\ (c_{13} + c_{55})p\,q & c_{33}q^2 + c_{55}p^2 - \rho \end{vmatrix} = 0\,. \tag{3.19}$$

This equation can be solved for the vertical slownesses of the individual wave modes:

$$\begin{aligned} q_\alpha &= \frac{1}{\sqrt{2}}\sqrt{K_1 - \sqrt{K_1^2 - 4K_2K_3}} \\ q_\beta &= \frac{1}{\sqrt{2}}\sqrt{K_1 + \sqrt{K_1^2 - 4K_2K_3}} \quad \text{, with} \\ K_1 &= \frac{\rho}{c_{33}} + \frac{\rho}{c_{55}} - \left(\frac{c_{11}}{c_{55}} + \frac{c_{55}}{c_{33}} - \frac{(c_{13}+c_{55})^2}{c_{33}c_{55}}\right)p^2 \\ K_2 &= \frac{c_{11}}{c_{33}}p^2 - \frac{\rho}{c_{33}} \quad \text{and} \\ K_3 &= p^2 - \frac{\rho}{c_{55}} \,. \end{aligned} \tag{3.20}$$

(Note that there is a misprint in the equation for K_1 in Graebner, 1992.) Here, q_α is the vertical slowness of a plane P-wave with amplitude U_α

$$\mathbf{u}_P = U_\alpha \begin{pmatrix} l_\alpha \\ 0 \\ m_\alpha \end{pmatrix} e^{i\omega(px_1 + q_\alpha x_3 - t)} \,, \tag{3.21}$$

and q_β denotes the vertical slowness of the corresponding SV-wave:

$$\mathbf{u}_{SV} = U_\beta \begin{pmatrix} l_\beta \\ 0 \\ m_\beta \end{pmatrix} e^{i\omega(px_1 + q_\beta x_3 - t)} \,. \tag{3.22}$$

Substituting the vertical slownesses into equation (3.19) yields the following expression for the direction cosines of the polarization vectors:

$$\begin{aligned} l_\alpha &= \sqrt{\frac{a_{33}q_\alpha^2 + a_{55}p^2 - 1}{a_{11}p^2 + a_{55}q_\alpha^2 - 1 + a_{33}q_\alpha^2 + a_{55}p^2 - 1}} \\ m_\alpha &= \sqrt{\frac{a_{11}p^2 + a_{55}q_\alpha^2 - 1}{a_{11}p^2 + a_{55}q_\alpha^2 - 1 + a_{33}q_\alpha^2 + a_{55}p^2 - 1}} \\ l_\beta &= \sqrt{\frac{a_{11}p^2 + a_{55}q_\beta^2 - 1}{a_{11}p^2 + a_{55}q_\beta^2 - 1 + a_{33}q_\beta^2 + a_{55}p^2 - 1}} \\ m_\beta &= \sqrt{\frac{a_{33}q_\beta^2 + a_{55}p^2 - 1}{a_{11}p^2 + a_{55}q_\beta^2 - 1 + a_{33}q_\beta^2 + a_{55}p^2 - 1}} \,, \end{aligned} \tag{3.23}$$

with $a_{ij} = c_{ij}/\rho$. Polarization vectors and vertical slownesses have to be found on both sides of the interface.

To evaluate the vector of reflection and transmission coefficients corresponding

to an incident P-wave

$$\mathbf{R} = (R_{PP}, R_{PS}, T_{PP}, T_{PS})^T \ ,$$

the following matrix system has to be solved:

$$\mathbf{M}\,\mathbf{R} = \mathbf{b} \tag{3.24}$$

Elements m_{ij} of matrix $\mathbf{M}$ are related to the parameters stated above as follows:

$$\begin{array}{llll} m_{11} = l_\alpha^{(1)}; & m_{12} = m_\beta^{(1)}; & m_{13} = -l_\alpha^{(2)}; & m_{14} = -m_\beta^{(2)}; \\ m_{31} = m_\alpha^{(1)}; & m_{32} = -l_\beta^{(1)}; & m_{33} = m_\alpha^{(2)}; & m_{34} = -l_\beta^{(2)}; \end{array}$$

$$\begin{array}{ll} m_{21} = pl_\alpha^{(1)} a_{13}^{(1)} + q_\alpha^{(1)} m_\alpha^{(1)} a_{33}^{(1)}; & m_{22} = pm_\beta^{(1)} a_{13}^{(1)} - q_\beta^{(1)} l_\beta^{(1)} a_{33}^{(1)}; \\ m_{23} = -(pl_\alpha^{(2)} a_{13}^{(2)} + q_\alpha^{(2)} m_\alpha^{(2)} a_{33}^{(2)}); & m_{24} = -(pm_\beta^{(2)} a_{13}^{(2)} - q_\beta^{(2)} l_\beta^{(2)} a_{33}^{(2)}); \\ m_{41} = a_{55}^{(1)} (q_\alpha^{(1)} l_\alpha^{(1)} + pm_\alpha^{(1)}); & m_{42} = a_{55}^{(1)} (q_\beta^{(1)} m_\beta^{(1)} - pl_\beta^{(1)}); \\ m_{43} = a_{55}^{(2)} (q_\alpha^{(2)} l_\alpha^{(2)} + pm_\alpha^{(2)}); & m_{44} = a_{55}^{(2)} (q_\beta^{(2)} m_\beta^{(2)} - pl_\beta^{(2)}). \end{array}$$

The superscripts $()^{(1)}$ $()^{(2)}$ refer to the upper and lower layer, respectively. Vector $\mathbf{b}$ can be expressed in terms of m_{ij} as

$$\mathbf{b} = (-m_{11}, -m_{21}, m_{31}, m_{41})^T \ .$$

Using Cramer's rule, the solution can be stated in analytic form:

$$\mathbf{R} = \frac{1}{\det \mathbf{M}} \begin{pmatrix} M_{11} & M_{12} & M_{13} & M_{14} \\ M_{21} & M_{22} & M_{23} & M_{24} \\ M_{31} & M_{32} & M_{33} & M_{34} \\ M_{41} & M_{42} & M_{43} & M_{44} \end{pmatrix}^T \cdot \mathbf{b} \tag{3.25}$$

Elements M_{ij} denote the cofactors of m_{ij}. The first element of vector $\mathbf{R}$ represents the P-P reflection coefficient. The numerical evaluation of equation (3.25) can be simplified by identifying some internal block symmetries in matrix $\mathbf{M}$ (Graebner, 1992). The exact reflection coefficients shown in this thesis are evaluated using equation (3.25). On the other hand, this solution cannot be represented in a concise form that reveals the influence of the individual model parameters on the scattering coefficients, and motivates analysis of simplified approximations similar to the ones developed for isotropic media.

3.3 Reflection and transmission at dipping interfaces

Reflection, refraction and mode conversion at dipping interfaces are surprisingly more complex phenomena in anisotropic models. Applying Snell's law, a straightforward procedure in isotropic media, becomes a real challenge both analytically and nu-

merically, especially if arbitrary structural dips and general anisotropy are considered. Here, I want to sketch a straightforward approach for computing the scattering coefficients for waves incident in the dip-plane of reflectors.

Conceptually, this reflection problem can be best described by considering the slowness surfaces (i.e., the loci of endpoints of slowness vectors) on both sides of the interface. The phases of the incident and scattered waves have to be identical at every point along the interface, yielding two conditions (Henneke, 1972).

- The slowness vectors of reflected and refracted waves must lie in the plane that contains the slowness vector of the incidence wave and normal to the interface. This is true even in general anisotropic three-dimensional media.

- The projection of the slowness vector onto the boundary is identical for each wavetype (Snell's law).

The tangential slowness component p_l can be evaluated by the following rotation of the original slowness vector.

$$p_l = p_1 \cos\phi + p_3 \sin\phi, \tag{3.26}$$

where ϕ is the dip of the interface. Then, we use p_l to solve for the four slowness vectors of the reflected and transmitted P- and SV-waves, represented by their components in the x_1- and x_3-coordinates. In isotropic media, such a procedure is straightforward and can be performed analytically. However in anisotropic media, resolving the slownesses requires solving a quartic or sextic equation by numerical methods. Then, the roots have to be associated with the individual wave modes. Upgoing and downgoing waves need to be identified by computing the group-velocity directions. Note that a negative value of a vertical slowness component (with respect to the interface) does not necessarily imply that the energy is propagating in the (negative) downward direction (Musgrave, 1970).

Unlike the procedure designed to continue the wavefield kinematically, the evaluation of the reflection and transmission coefficients involves searching for all polarizations and slownesses of waves generated by the incident wave. These (in general complex) quantities, together with the stiffness tensors on both sides of the interfaces, need to be rotated into a new coordinate system with unit vectors parallel and normal to the interface. Once the vertical slownesses and the polarizations have been computed in the rotated coordinate system, the kinematic and dynamic boundary conditions [equations (2.5) and (2.8)] yield a (generally complex) linear system of equations of the form (3.24), which can be inverted numerically.

3.4 Approximate reflection and transmission coefficients

The exact solution of the reflection/transmission problem [equation (3.25)] is too complex to comprehend the influence of anisotropy on the reflection coefficient.

Numerical studies by Wright (1987) showed that the influence of anisotropy on the reflection coefficient is not negligible. Analytic work by Banik (1987) confirmed that anisotropy has a first-order influence on *P*-wave AVO gradients. Thomsen (1993) provided a more general solution for the whole range of pre-critical incidence angles, valid for small contrasts in elastic parameters across the boundary and weak anisotropy. In this section, Thomsen's approximation will be reproduced in a modified and corrected form.

The first step in Thomsen's analysis is to set up the kinematic and dynamic boundary conditions [equations (2.5) and (2.8), respectively], for both incident *P*- and *SV*-waves. I use the parameterization introduced in Chapter 2 to form the set of linear equations

$$\mathbf{M} \begin{pmatrix} R_P & R_{SP} \\ T_P & T_{SP} \\ R_{PS} & R_S \\ T_{PS} & T_S \end{pmatrix} = \mathbf{b} \, . \tag{3.27}$$

Due to the considerable size and complexity of the matrices and vectors considered in this derivation, I show the individual elements of the 4×4 matrix M and the 4×2 matrix b in Appendix A. The boundary conditions in equation (3.27) that correspond to an incident *P*-wave are given by equations (2.6), (2.9) and (2.10). Note that R_{SP} and T_{SP} are the amplitudes of the reflected and transmitted *P*-waves generated by an incident *SV*-wave of unit amplitude. Numerically, the inversion of matrix M is the main step in recovering the scattering coefficients. To derive concise analytic expressions, Thomsen (1993) proposed an alternative approach. He considers a boundary between two weakly anisotropic VTI media with a small percentage difference in the elastic properties across the boundary. Specifically, let us introduce seven small quantities d_i ($|d_i| << 1$ $(i = 1, 2, ..7)$):

$$\begin{aligned} d_1 &\equiv \frac{\Delta V_{P0}}{\bar{V}_{P0}} \qquad d_2 \equiv \frac{\Delta V_{S0}}{\bar{V}_{S0}} \\ d_3 &\equiv \frac{\Delta \rho}{\bar{\rho}} \\ d_4 &\equiv \delta_1 \qquad d_5 \equiv \epsilon_1 \\ d_6 &\equiv \delta_2 \qquad d_7 \equiv \epsilon_2 \, , \end{aligned} \tag{3.28}$$

and the operator

$$\Delta \equiv d_j \frac{\partial}{\partial d_j} \, ,$$

where the partial derivative is evaluated for $d_j = 0$ $(j = 1, 2, ..7)$. As in Chapter 2, the average value and the difference in vertical *P*-wave velocity, for example, are defined

as

$$\begin{aligned} \bar{V}_{P0} &= 1/2\,(V_{P0_1} + V_{P0_2}) \\ \Delta V_{P0} &= V_{P0_2} - V_{P0_1}\,, \end{aligned} \tag{3.29}$$

and correspondingly for $\bar{V}_{S0}$, ΔV_{S0}, etc. Instead of solving equation (3.27) for a wave incident at phase angle i, let us first consider a plane wave incident at the same incidence angle upon the "average" (or "unperturbed") model, i.e., the model that can be obtained by setting all small quantities d_j to zero. In this case, equation (3.27) can be rewritten in the unperturbed form

$$\mathbf{M^u R^u = b^u}\,, \tag{3.30}$$

where the superscript u stands for "unperturbed". Obviously, $\mathbf{M^u}$, $\mathbf{R^u}$ and $\mathbf{b^u}$ are simpler than $\mathbf{M}$, $\mathbf{R}$ and $\mathbf{b}$. For example, each column of $\mathbf{R^u}$ has only one nonzero component because no reflected and converted energy is generated at the "transparent" boundary between the two identical layers. This suggests rewriting equation (3.27) in the following linearized form:

$$(\mathbf{M^u} + \mathbf{\Delta M})\,(\mathbf{R^u} + \mathbf{\Delta R}) = (\mathbf{b^u} + \mathbf{\Delta b}) \tag{3.31}$$

The quantity of interest is $\mathbf{\Delta R}$ which, to a first approximation, can be written as

$$\mathbf{\Delta R} = (\mathbf{M^u})^{-1}\,(\mathbf{\Delta b} - \mathbf{\Delta M\,R^u})\,. \tag{3.32}$$

Using Cramer's rule, one can find the inverse of $\mathbf{M^u}$. I solved equation (3.32) and obtained the following solution for the most important element of $\mathbf{\Delta R}$, the *P-P* reflection coefficient:

$$\begin{aligned} R_{\mathrm{P}}^{\mathrm{VTI}}(\theta) &= \frac{1}{2}\frac{\Delta Z}{\bar{Z}} + \frac{1}{2}\left\{\frac{\Delta V_{P0}}{\bar{V}_{P0}} - \left(\frac{2\bar{V}_{S0}}{\bar{V}_{P0}}\right)^2 \frac{\Delta G}{\bar{G}} + \Delta\delta\right\}\sin^2\theta + \\ &\quad \frac{1}{2}\left\{\frac{\Delta V_{P0}}{\bar{V}_{P0}} + \Delta\epsilon\right\}\sin^2\theta\tan^2\theta\,, \end{aligned} \tag{3.33}$$

where θ denotes the incident phase angle [1], $Z \equiv \rho V_{P0}$ is the vertical *P*-wave impedance, and $G \equiv \rho V_{S0}^2$ is the vertical shear modulus. The differences in the anisotropy coefficients across the boundary are written as $\Delta\delta \equiv (\delta_2 - \delta_1)$, $\Delta\epsilon \equiv (\epsilon_2 - \epsilon_1)$. Equation (3.33) differs from Thomsen's result in that here, the difference in anisotropy parameter $\Delta\delta$ does not appear in the $\sin^2\theta\tan^2\theta$-term [2]. The presence of $\Delta\delta$ in Thomsen's result may cause inaccuracies at large angles; specifically, for nonzero val-

[1] In this linear approximation, it is however valid to interchange the incidence angle with the average of the incidence and the refracted angles.

[2] The extra $\Delta\delta$ term in Thomsen's equation turned out to be caused by an error at the final step of his derivation

ues of $\Delta\delta$, Thomsen's approximation does not work well for angles larger than 20° and breaks down for angles greater than 45° where the $\sin^2\tan^2$-term dominates over the AVO-gradient term. Equation (3.33) was discussed in detail in Blangy (1994), but with the wrong $\sin^2\theta\tan^2\theta$-term. The newly derived P-wave reflection-coefficient approximation is consistent with observations by Kim et. al. (1993) that $\Delta\epsilon$ dominates the behavior of their numerically computed AVO curves for large angles of incidence.

If Z^S denotes the vertical shear impedance ($Z^S \equiv \rho V_{S0}$), the corresponding expression for the SV-mode reflection coefficient is given by

$$\mathrm{R}_{SV}^{\mathrm{VTI}} = -1/2\,\frac{\Delta Z^S}{\bar{Z}^S} + \left\{\frac{7}{2}\frac{\Delta V_{S0}}{\bar{V}_{S0}} + 2\frac{\Delta\rho}{\bar{\rho}} + \frac{1}{2}\left(\frac{\bar{V}_{P0}}{\bar{V}_{S0}}\right)^2(\Delta\epsilon - \Delta\delta)\right\}\sin^2 j - 1/2\,\frac{\Delta V_{S0}}{\bar{V}_{S0}}\sin^2 j\tan^2 j\,. \tag{3.34}$$

Recall that in the limit of weak anisotropy, the angular variation of the SV-wave phase velocity is governed by $\sigma = \left(\frac{V_{P0}}{V_{S0}}\right)^2(\epsilon - \delta)$ [see equation (3.14)]; the same combination of parameters determines the influence of anisotropy on the small-angle term in equation (3.34). For a typical ratio of $\frac{V_{P0}}{V_{S0}} \approx 2$, the difference in $(\epsilon - \delta)$ is of comparable importance to the AVO gradient as the relative difference in density and vertical shear velocity.

The SH-wave reflection problem can be treated in a way similar to that in the study of P/SV scattering. The solution for the SH-wave reflection coefficient shows the following dependence on the contrast in anisotropy parameter γ across the boundary:

$$\mathrm{R}_{SH}^{\mathrm{iso}} = -1/2\,\frac{\Delta Z^S}{\bar{Z}^S} + 1/2\left(\frac{\Delta V_{S0}}{\bar{V}_{S0}} + \Delta\gamma\right)\tan^2 j\,, \tag{3.35}$$

More details of this derivation, including the inversion of matrix $\mathbf{M}^{\mathbf{u}}$, the linearized polarization vectors and reflected and refracted angles can be found in Appendix A. Appendix A also shows the remaining reflection and transmission coefficients of pure and converted modes.

3.5 Influence of VTI anisotropy on *P*-wave AVO

Approximation (3.33) is remarkably simple while still being accurate even for large incidence angles because no small-angle approximation was used in its derivation. Moreover, it allows us to decompose the reflection coefficient as

$$R_{\mathrm{P}}^{\mathrm{VTI}}(\theta) = R_{\mathrm{P}}^{\mathrm{iso}}(\theta) + R_{\mathrm{P}}^{\mathrm{ani}}(\theta)\,, \tag{3.36}$$

where $R_{\mathrm{P}}^{\mathrm{iso}}(\theta)$ is the reflection coefficient in the absence of anisotropy ($\epsilon = 0$, $\delta = 0$), and $R_{\mathrm{P}}^{\mathrm{ani}}$ is the anisotropic term given by

$$R_{\mathrm{P}}^{\mathrm{ani}}(\theta) = \frac{1}{2}(\delta_2 - \delta_1)\sin^2\theta + \frac{1}{2}(\epsilon_2 - \epsilon_1)\sin^2\theta\tan^2\theta\,. \tag{3.37}$$

Equations (3.36) and (3.37) make it possible to draw the following conclusions (see also Thomsen, 1993):

- In Thomsen's (1986) notation, anisotropy does not have any influence on the reflection coefficient for vertically incident waves (i.e, the normal-incidence reflection coefficient is identical to that of a wave incident on the interface between the corresponding isotropic layers with velocities V_{P0} and V_{S0}).

- The parameter δ controls the $\sin^2\theta$ term, which determines the small-angle reflection coefficient, while ϵ is responsible for the $\sin^2\theta\tan^2\theta$, which becomes influential at larger incidence angles. This is a manifestation of the well-known fact that δ controls the influence of anisotropy on near-vertically traveling P-waves, while ϵ dominates near-horizontal wave propagation.

- There is no influence of the shear-wave vertical velocity V_{S0} on $R_{\mathrm{P}}^{\mathrm{ani}}$, although V_{S0} does make a contribution to $R_{\mathrm{P}}^{\mathrm{iso}}$.

- If there exists no contrast in δ and ϵ across the interface, the approximate reflection coefficient coincides with the one for purely isotropic media.

- Anisotropy has a pronounced influence on the reflection coefficients if the relative changes in (isotropic) elastic parameters are smaller or of comparable in size.

To illustrate the accuracy of equation (3.33), I show the P-wave reflection coefficients for the same shale/sandstone models as in Chapter 2 (see Table 2.1), but the shale-overburden is assumed to have VTI symmetry; the magnitude of anisotropy ($\delta = 0.120$ and $\epsilon = 0.133$) is chosen according to Kim et. al. (1993). Figure 3.6 illustrates the accuracy of equation (3.33) as compared with the exact solution and the corresponding (exact) isotropic reflection coefficient ($\delta = 0$ and $\epsilon = 0$). Here and in all subsequent plots, "incidence angle" denotes the phase angle of the incident wave. The examples in Figure 3.6 show that the presence of anisotropy can substantially change the slope of the AVO gradient. Note that the approximation and the exact reflection curves are close to each other for the first two models. Most importantly, the approximation precisely describes the departure of the reflection coefficient curves away from the isotropic ones and, therefore, correctly predicts the influence of anisotropy. As expected from the fair performance of the corresponding isotropic approximation (2.19) at large angles of incidence (see Figure 2.3), the accuracy of equation (3.33) is lower in the third model. However, the approximation still predicts the correct trend; for example, it predicts that the AVO gradient does not change

much compared to that for the isotropic curve and that the anisotropy has a more significant impact on the reflection-coefficients for higher angles of incidence. Thus, even in this case, the approximation is helpful in understanding the influence of anisotropy on the AVO response.

The examples are repeated for a higher value of anisotropy parameter $\epsilon = 0.233$ in Figure 3.7. As expected from the influence of ϵ in equation (3.33), the differences between the curves in Figures 3.6 and 3.7 are restricted to large angles of incidence while the accuracy of the approximations remains essentially unchanged.

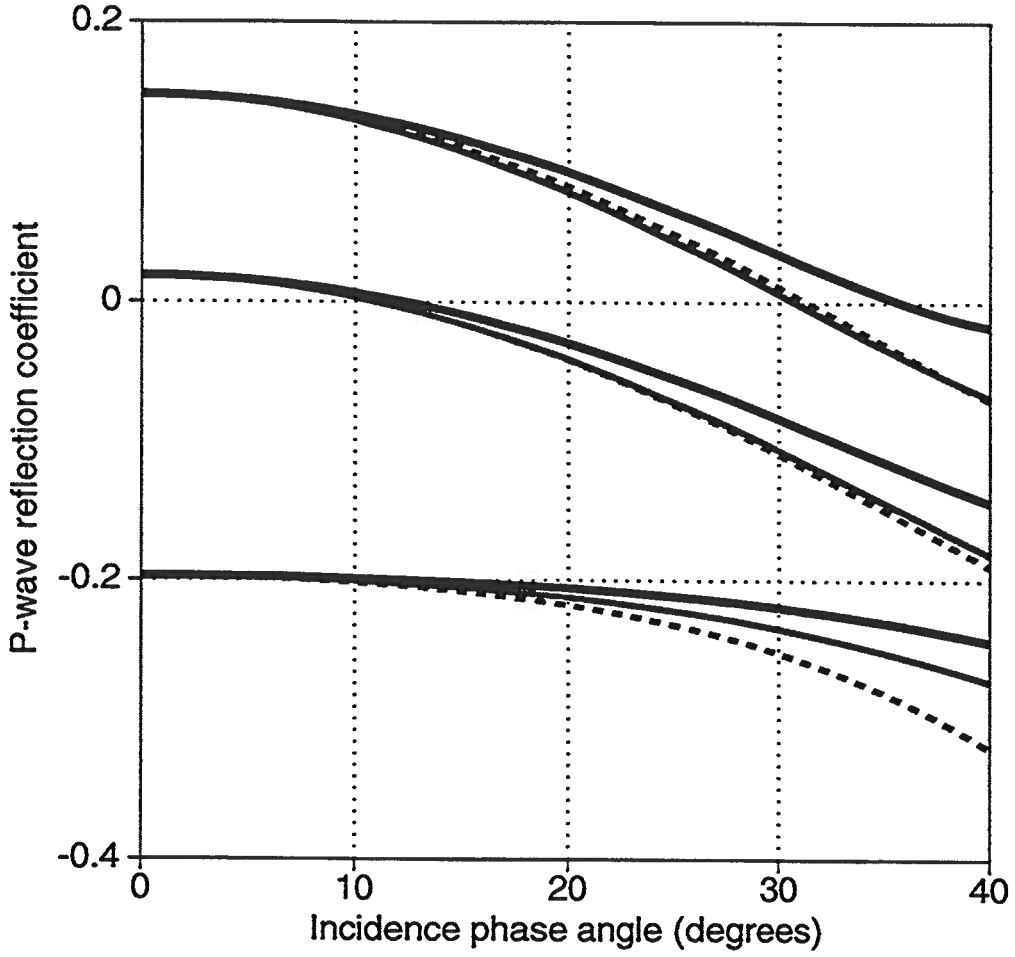

FIG. 3.6. *P*-wave reflection coefficient curves for the three models shown in Table 2.1. The black line denotes the exact isotropic reflection coefficient and the thinner gray line shows the exact reflection coefficient after introducing vertical transverse isotropy into the shale overburden ($\delta = 0.12, \epsilon = 0.133$). The approximation [equation (3.33)] is shown by the dashed line.

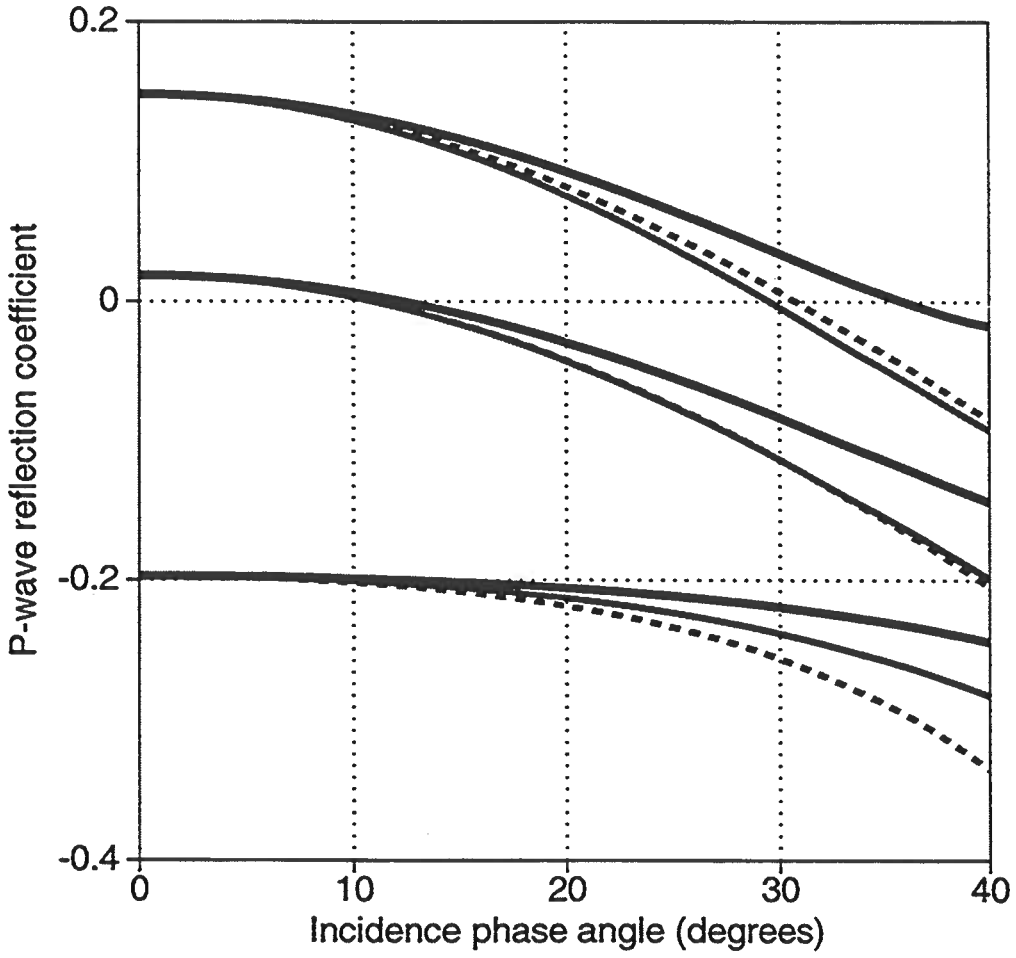

FIG. 3.7. The same P-wave reflection coefficient curves as the ones shown in Figure 3.6, but for a larger magnitude of anisotropy in the shale layer ($\delta = 0.12, \epsilon = 0.233$).

Chapter 4

HORIZONTAL TRANSVERSE ISOTROPY – THE SYMMETRY PLANES

Most upper-crustal media and certain reservoir rocks of interest to hydrocarbon exploration show azimuthal anisotropy of various types and strength (Crampin, 1985), implying that the angular dependence of reflection coefficients may change with azimuth. The "first-order" model for azimuthal anisotropy is transverse isotropy with a horizontal axis of symmetry (HTI). Physical reasons for a medium of HTI symmetry include systems of parallel vertical cracks embedded in an isotropic matrix, similar to the medium shown in Figure 4.1 and/or vertically dipping shale sequences.

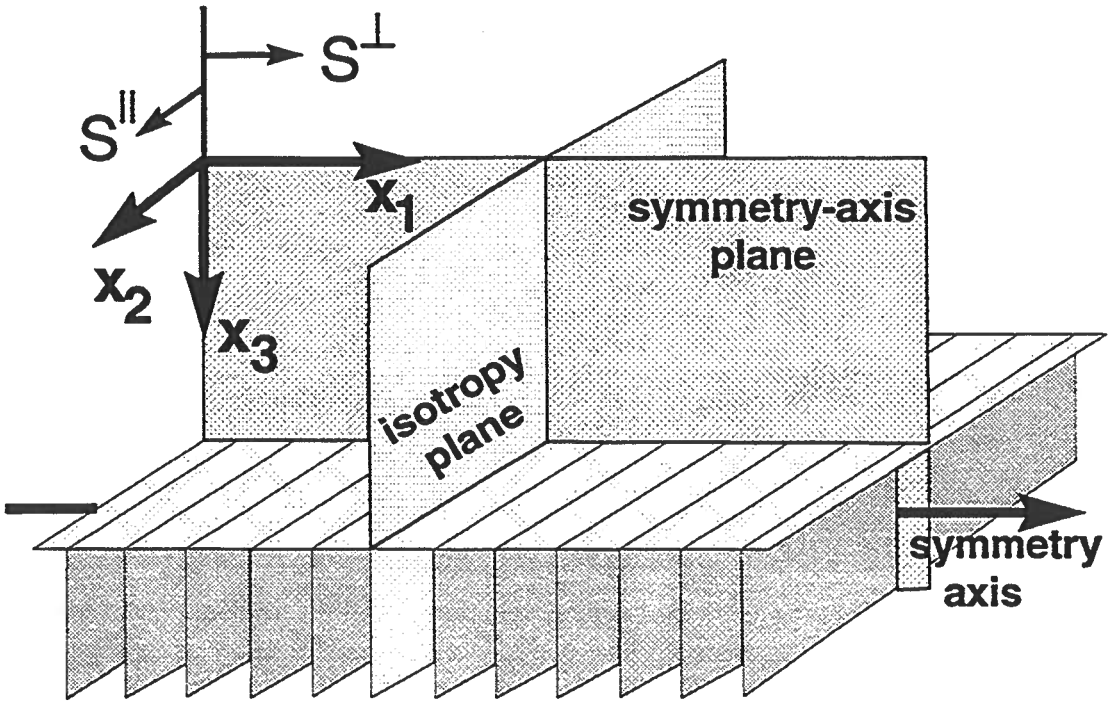

FIG. 4.1. Sketch of an HTI model. *P*-wave reflections in the two vertical symmetry planes, here called the *symmetry-axis* plane and the *isotropy* plane, are discussed in the text. Shear waves polarized parallel and normal to the isotropy plane have different vertical velocities.

Let us assume that the symmetry axis of the HTI model is parallel to the x_1-direction. The $[x_1, x_3]$-plane, which contains the symmetry axis, is hereafter referred to as the "symmetry-axis plane." Waves confined to the plane normal to the symmetry axis do not exhibit any velocity variations with propagation angle; hence, this plane is the so-called "isotropy plane" or "fracture plane." Shear waves propagating in the isotropy plane can travel with two different velocities, depending on whether their polarization vector is confined to the isotropy plane.

Analytic expressions for reflection coefficients, either exact or approximate, are mostly restricted to VTI models (Daley & Hron, 1977; Banik, 1987; Graebner, 1992; Thomsen, 1993; Blangy, 1994). Studies of *P*-wave AVO signatures in HTI media have been of a purely empirical nature without any analytic study of the AVO response (e.g., Lefeuvre, 1994). The analysis presented in this thesis fills in this gap by complementing exact numerical results with concise analytic expressions. I begin with a numerical study of the exact reflection coefficients for various azimuths. Then I discuss the angular dependence of pure-mode reflection coefficients in the isotropy plane and, subsequently, exploit analogies between VTI and HTI media to extend the AVO analysis for VTI media to HTI symmetry-axis planes.

4.1 Significance of the HTI model

A plane *P*-wave incident on an HTI medium outside the symmetry-axis and isotropy planes generates three plane waves with mutually orthogonal polarization directions in the lower medium:

- A (quasi-longitudinal) *P*-wave polarized approximately along its propagation direction. Its polarization vector is confined to the plane containing the slowness vector and the symmetry axis.

- A shear wave polarized within the isotropy plane, referred to as $S^{\parallel}$-wave (the fast mode in the vertical direction).

- A shear wave polarized in the plane formed by the slowness vector and the symmetry axis, here called the $S^{\perp}$-wave (the slow mode in the vertical direction).

Boundary conditions have to be applied to solve for the reflection and transmission coefficients. As for the isotropic and VTI energy-partitioning problems discussed above, these conditions are the continuity of particle displacement, shear and normal traction. After evaluating vertical slownesses, polarizations and phase velocities for all generated wave types and substituting them into the boundary conditions, we obtain a system of six linear equations for the reflection/transmission coefficients.

Based on this approach, I implemented an algorithm to compute the exact reflection and transmission coefficients for interfaces between two HTI media with the same direction of the symmetry axis. In Figure 4.2, reflection-coefficient curves are shown for azimuths of $0, 30, 60$ and $90°$ measured with respect to the symmetry direction. In

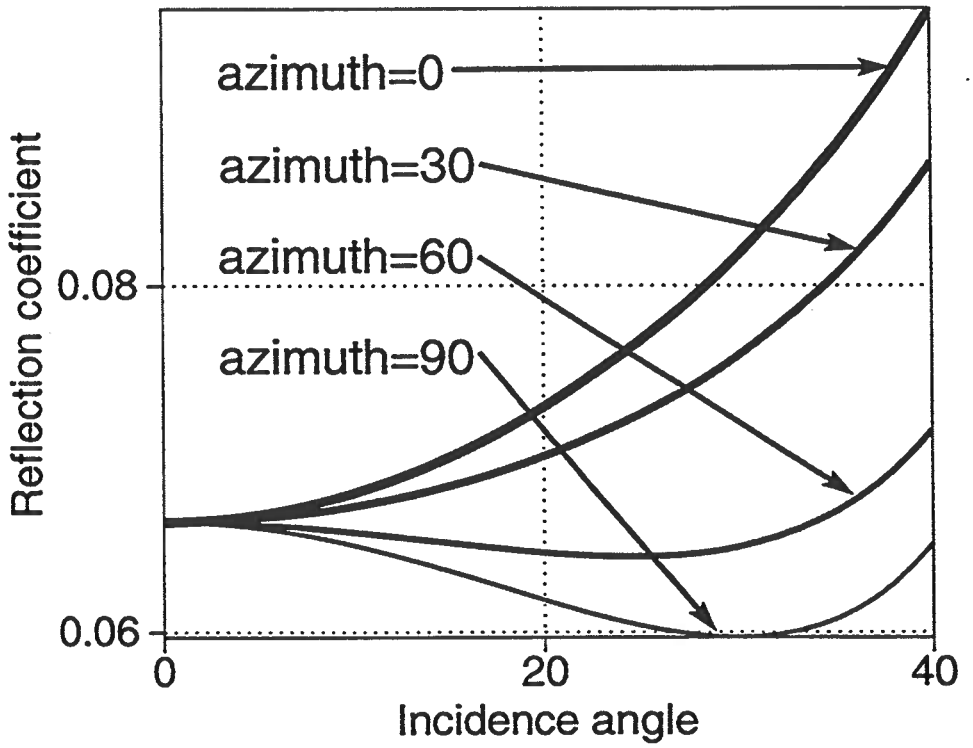

FIG. 4.2. Reflection coefficient as a function of the incidence and azimuthal angles for a boundary between an isotropic overburden and an HTI medium. The azimuth is measured with respect to the symmetry axis. $V_{P0_1} = 2.26$, $V_{S0_1} = 1.428$, $\rho_1 = 2.6$, $\epsilon_1 = 0$, $\delta_1 = 0$, $\gamma_1 = 0$, $V_{P0_2} = 2.37$, $V_{S0_2} = 1.36$, $\rho_2 = 2.7$, $\epsilon_2 = 0.05$, $\delta_2 = 0.02$ and $\gamma_2 = 0.1$. V_{P0} and V_{S0} are symmetry-direction velocities, and δ_2, ϵ_2 and γ_2 are the generic Thomsen parameters defined with respect to the horizontal symmetry axis of the second medium.

this experiment, the upper medium is purely isotropic. The azimuthal change in the absolute value, as well as in the slope of the reflection coefficient, are rather significant. Only for normal incidence do the curves coincide.

Clearly, evaluating reflection coefficients for HTI media is more complicated than for VTI media. However, as indicated by the above example (Figure 4.2), ignoring the presence of anisotropy in HTI media has the potential of severely distorting conventional AVO analysis. On the other hand, a careful study of the reflection response in HTI media can provide additional information for the estimation of physical properties of the medium.

In general, exact evaluation of the HTI reflection coefficient at arbitrary azimuth requires a numerical calculation. The next sections describe how to obtain an analytic solution and useful approximations to the reflection coefficients for incident P-waves confined to the isotropy and symmetry-axis planes. Comparison of these symmetry-plane coefficients can then help in estimating the magnitude of the azimuthal change and relate it to the anisotropy of the subsurface.

4.2 P-wave reflections in HTI isotropy-planes

Two different shear waves can propagate in HTI media. An incident P-wave confined to the isotropy (fracture) plane excites the $S^{\parallel}$-mode polarized within this plane. This shear wave travels with a different speed than that of the $S^{\perp}$-wave generated by an incident P-wave confined to the symmetry-axis plane.

It is straightforward to compute the exact P-P reflection coefficients in the isotropy plane using existing solutions for isotropic media. For example, one can use the exact analytic representation of the P-P reflection coefficient given by Aki and Richards (1980) [equation (2.12)], by simply inserting the proper (fracture-plane) velocities.

It is important to note that due to the difference in the velocities of $S^{\parallel}$ and $S^{\perp}$ waves, several different parameterizations can be used to represent approximate solutions to the reflection problem in HTI media. To avoid any confusion, I explicitly state the meaning of the parameters used in the remainder of this paper by relating them to the stiffness elements (in Voigt notation; see, for example, Musgrave, 1970), defined for the coordinate frame shown in Figure 4.1, i.e., for the symmetry axis pointing in the x_1-direction:

$$\begin{aligned} \beta &= \sqrt{\frac{c_{44}}{\rho}}; \\ \alpha &= \sqrt{\frac{c_{33}}{\rho}}; \\ G &= \rho\beta^2; \\ Z &= \rho\alpha\,. \end{aligned} \tag{4.1}$$

Here, β and α are the isotropy-plane velocities of the $S^{\|}$-wave and the compressional wave, respectively. G denotes shear modulus corresponding to the vertically propagating $S^{\|}$-wave, and Z denotes the vertical P-wave impedance. Note that β in equation (4.1) refers to the fast vertical shear-wave velocity and, in general, is different from V_{S0}, the velocity of shear waves propagating in the symmetry-axis direction.

Now we can state the approximate solution for the P-P reflection coefficient in the isotropy plane. Using the parameterization from equation (4.1), we find the reflection coefficient for P-waves incident in the isotropy plane:

$$R_{\mathrm{P}}^{\mathrm{strike}}(\theta) = \frac{1}{2}\frac{\Delta Z}{\bar{Z}} + \frac{1}{2}\left\{\frac{\Delta\alpha}{\bar{\alpha}} - \left(\frac{2\bar{\beta}}{\bar{\alpha}}\right)^2 \frac{\Delta G}{\bar{G}}\right\}\sin^2\theta + \frac{1}{2}\left\{\frac{\Delta\alpha}{\bar{\alpha}}\right\}\sin^2\theta\tan^2\theta\,. \tag{4.2}$$

In essence, equation (4.2) is just the classical approximate reflection coefficient for interfaces between isotropic media [see equation (2.19)] with the faster S-wave vertical velocity playing the role of V_S. Below, I show the corresponding shear-wave reflection coefficients obtained in the same way.

4.3 Limited VTI/HTI analogy

Consider the VTI and HTI models shown in Figure 4.3. As before, the symmetry axis of the VTI model points in the x_3-direction, whereas the symmetry axis of the HTI model coincides with the x_1-axis. In both cases, the stiffness tensor has five independent components; if the physical cause of the anisotropy is known, some of the components may be related to each other. In the coordinate-system frame shown in Figure 4.3 (the x_3-axis is pointing downwards), we can represent the elastic stiffnesses as symmetric 6×6 matrices $\mathbf{C}_{\mathrm{VTI}}$ and $\mathbf{C}_{\mathrm{HTI}}$ (Musgrave, 1970):

$$\mathbf{C}_{\mathrm{VTI}} = \begin{pmatrix} c_{11} & (c_{11}-2c_{66}) & c_{13} & & & \\ (c_{11}-2c_{66}) & c_{11} & c_{13} & & & \\ c_{13} & c_{13} & c_{33} & & & \\ & & & c_{55} & & \\ & & & & c_{55} & \\ & & & & & c_{66} \end{pmatrix} \tag{4.3}$$

$$\mathbf{C}_{\mathrm{HTI}} = \begin{pmatrix} c_{11} & c_{13} & c_{13} & & & \\ c_{13} & c_{33} & (c_{33}-2c_{44}) & & & \\ c_{13} & (c_{33}-2c_{44}) & c_{33} & & & \\ & & & c_{44} & & \\ & & & & c_{55} & \\ & & & & & c_{55} \end{pmatrix}. \tag{4.4}$$

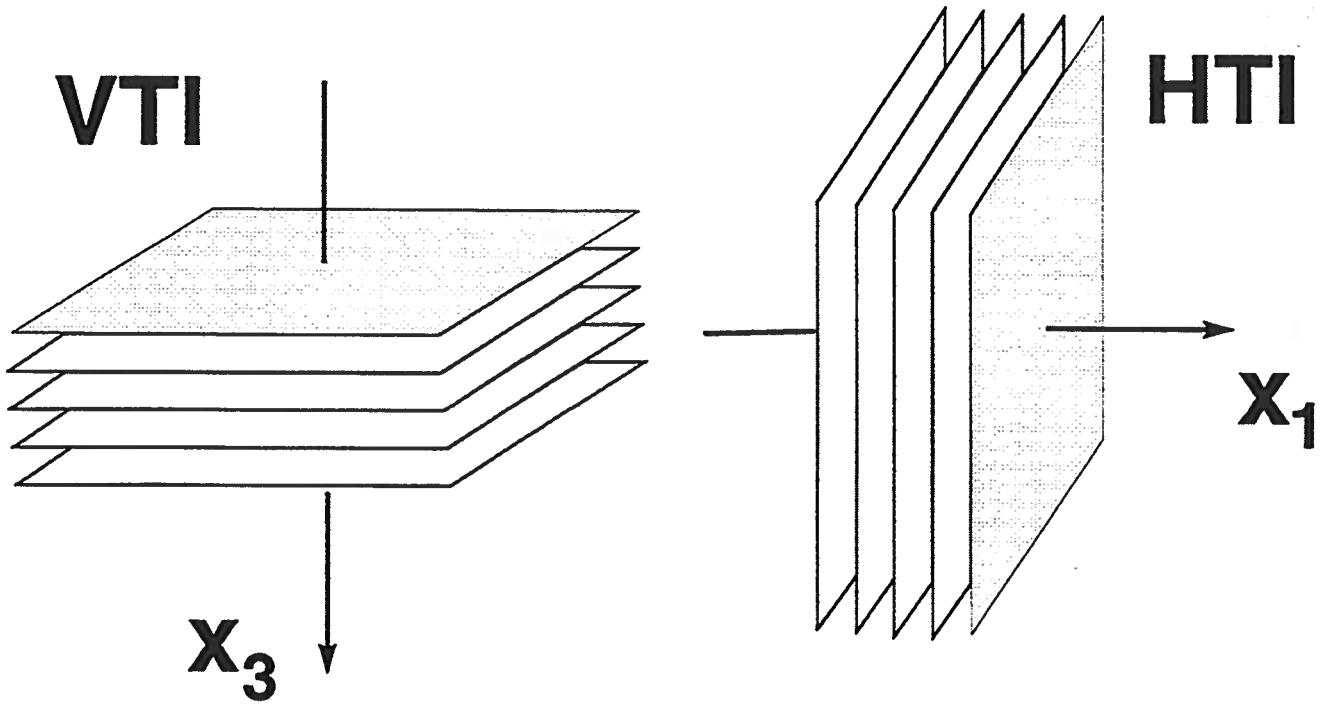

FIG. 4.3. The analogy between VTI and HTI models helps to extend solutions for VTI reflection coefficients to the symmetry-axis plane of HTI media.

Although both models are of the same symmetry type, the $\mathbf{C}_{\mathrm{VTI}}$ and $\mathbf{C}_{\mathrm{HTI}}$ stiffness matrices differ due to the different direction of the symmetry axis (the symmetry axes of the VTI and HTI models are pointing in the x_3- and x_1-direction, respectively). For example, c_{55} is identical to c_{44} in VTI models while c_{55} equals c_{66} in HTI models. Propagation of body waves in elastic media is governed by the Christoffel equation (3.4):

$$[\, c_{ijkl}\, p_j\, p_l - \rho\, \delta_{ik}\,]\, U_k = 0\,, \tag{4.5}$$

where p_i are the slowness components and U_k is the polarization vector. Using the two-index notation and inserting $\mathbf{C}_{\mathrm{VTI}}$ and $\mathbf{C}_{\mathrm{HTI}}$ into equation (4.5) generally yields two different solutions for waves propagating in VTI and HTI media. However, the key observation that will allow us to find kinematic seismic signatures and the reflection coefficients in a straightforward way is that equation (4.5), applied to wave propagation in the $[x_1, x_3]$-plane, is *identical* for both VTI and HTI models. Using the Voigt recipe to switch to the two-index notation (Musgrave, 1970), we rewrite equation (4.5) for in-plane polarized waves in media of either VTI symmetry [see equation (3.19)] or HTI symmetry as

$$\begin{bmatrix} c_{11}p_1^2 + c_{55}p_3^2 - \rho & (c_{13}+c_{55})p_1\, p_3 \\ (c_{13}+c_{55})p_1 p_3 & c_{33}p_3^2 + c_{55}p_1^2 - \rho \end{bmatrix} \begin{bmatrix} U_1 \\ U_3 \end{bmatrix} = 0\,. \tag{4.6}$$

Equation (4.6) provides the solution for the slowness and the polarization vectors of P- and $S^{\perp}$-wave propagation in the $[x_1, x_3]$-plane of VTI and HTI media. Thus, all equations describing velocities, traveltime, polarization and stresses for waves propagating in the $[x_1, x_3]$-plane are identical for media with the symmetry axis pointing in either the x_1 (HTI) or the x_3 (VTI) direction. Moreover, in transversely isotropic media, seismic signatures are a function of the angle with the symmetry axis and we can use the solutions in the symmetry-axis plane for any phase vector that makes the same angle with the symmetry axis. Hence the equivalence between VTI and HTI symmetries can be used not only for seismic signatures within the symmetry-axis plane, but also for any arbitrary azimuthal direction.

4.4 New anisotropy parameters for HTI media

As suggested by the discussion above, for any HTI model there exists an "equivalent" VTI model that has the same kinematic properties and polarizations of P- and $S^{\perp}$-waves in the $[x_1, x_3]$-plane. Thus, P- and $S^{\perp}$-wave propagation in the $[x_1, x_3]$-plane (i.e., the symmetry-axis plane) of HTI media can be described by the known VTI equations using the elastic stiffness components c_{ij} or, alternatively, using Thomsen's parameters $\epsilon^{(V)}$ and $\delta^{(V)}$ defined with respect to vertical in the same way as in VTI media:

$$\epsilon^{(V)} \equiv \frac{c_{11} - c_{33}}{2c_{33}};$$

$$\delta^{(V)} \equiv \frac{(c_{13}+c_{55})^2-(c_{33}-c_{55})^2}{2c_{33}(c_{33}-c_{55})} . \quad (4.7)$$

The coefficients $\epsilon^{(V)}$ and $\delta^{(V)}$ of the equivalent VTI model are different from the generic coefficients ϵ and δ defined with respect to the horizontal symmetry axis. The VTI and HTI anisotropy parameters can be related in the following way:

$$\begin{aligned} \epsilon^{(V)} &= -\frac{\epsilon}{1+2\epsilon}; \\ \delta^{(V)} &= \frac{\delta - 2\epsilon\left(1+\frac{\epsilon}{f}\right)}{(1+2\epsilon)\left(1+\frac{2\epsilon}{f}\right)}, \end{aligned} \quad (4.8)$$

where

$$f \equiv 1-(V_{S0}/V_{P0})^2 .$$

Both V_{S0} and V_{P0} are measured along the horizontal symmetry axis. Figures 4.4a-c illustrate why the new set of anisotropy parameters (besides allowing allowing the description of seismic signatures with already known VTI equations) is convenient for describing seismic reflection signatures in HTI media. Similar to Figure 3.1, the black lines in Figure 4.4a denote *P*-wave rays propagating in a VTI medium. Shown in white are two wavefronts; the continuous line corresponds to points at 0.75 s traveltime along the VTI rays while the dashed circle indicates a classical wavefront in isotropic media with angularly invariant velocity V_{P0}. Also indicated in Figure 4.4a is the significance of Thomsen's parameters. The difference between the dashed and continuous white wavefronts for horizontal propagation is governed by the value of Thomsen's parameter ϵ, while a negative value of δ, for example, means that the "anisotropic" (continuous) wavefront is less advanced for near-vertical propagation than the dashed "isotropic" wavefront.

Wave propagation in HTI media (see Figure 4.4b) can be simply illustrated by a 90° rotation of Figure 4.4a. Note that ϵ again indicates the difference between vertical and horizontal *P*-wave velocities, and the vertical velocity can be expressed as a function of V_{P0} and ϵ. On the other hand, δ describes the departure from the isotropic wavefront close to horizontal, an angular region that is not of importance in surface seismic applications. It is hence desirable to introduce a new set of parameters that describes

1. the vertical *P*-wave velocity
2. the departure from isotropy for near vertical propagation
3. the difference between vertical and horizontal wave velocities.

As shown in Figure 4.4c, this is accomplished by the set of parameters α, $\delta^{(V)}$ and $\epsilon^{(V)}$. The reference isotropic wavefront is now computed with the vertical velocity α and is shown as a dashed white circle in Figure 4.4c. For the particular model shown in this figure, both anisotropy parameters $\delta^{(V)}$ and $\epsilon^{(V)}$ are negative.

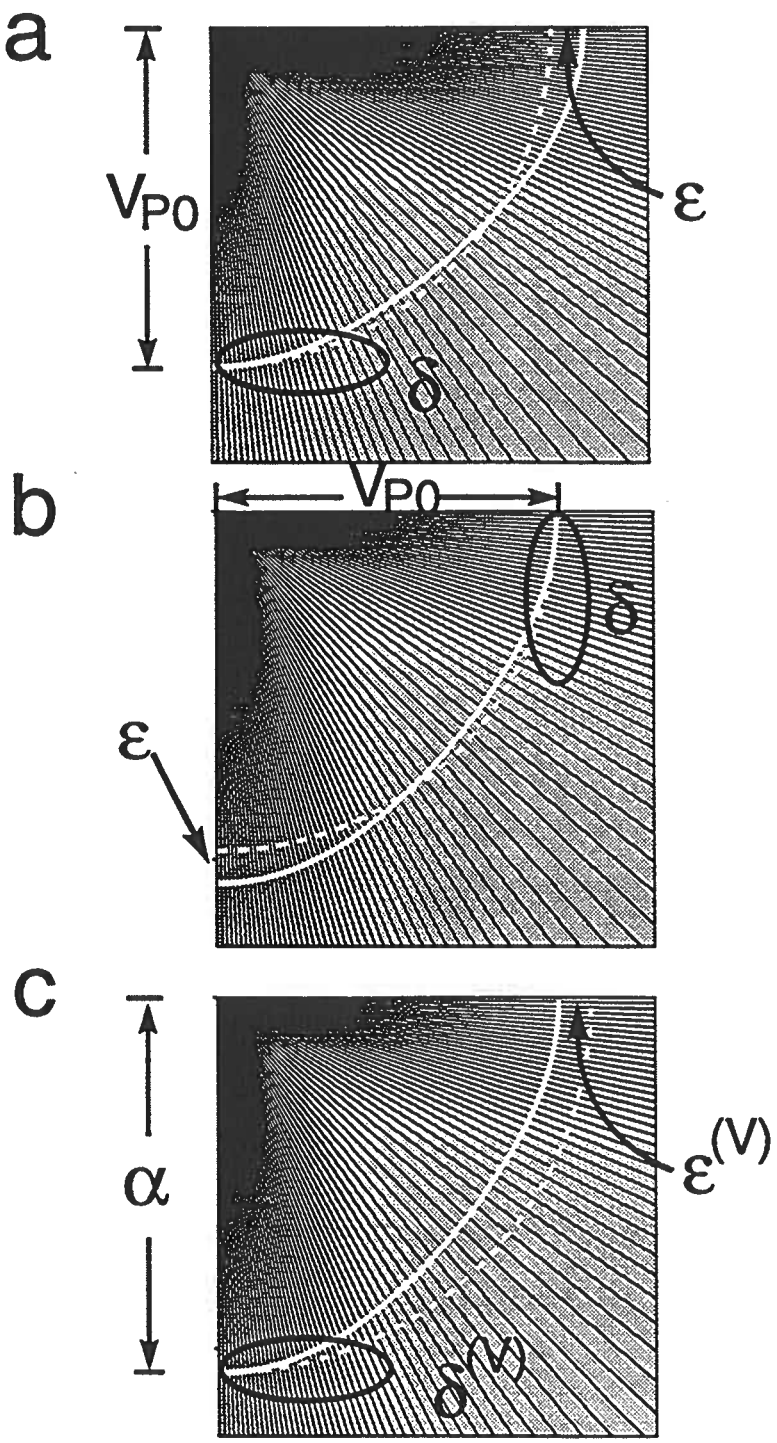

FIG. 4.4. *P*-wave propagation in VTI (a) and HTI (b,c) media and corresponding medium parameterization.

	c_{ij} – notation	generic Thomsen notation (exact)	(weak anisotropy)
α	$\sqrt{c_{33}/\rho}$	$V_{P0}\sqrt{1+2\epsilon}$	$V_{P0}(1+\epsilon)$
β	$\sqrt{c_{44}/\rho}$	$V_{S0}\sqrt{1+2\gamma}$	$V_{S0}(1+\gamma)$
$\beta^{\perp}$	$\sqrt{c_{55}/\rho}$	V_{S0}	V_{S0}
$\delta^{(V)}$	$\frac{(c_{13}+c_{55})^2-(c_{33}-c_{55})^2}{2c_{33}(c_{33}-c_{55})}$	$\frac{\delta-2\epsilon(1+\epsilon/f)}{(1+2\epsilon)(1+2\epsilon/f)}$	$\delta-2\epsilon$
$\epsilon^{(V)}$	$\frac{c_{11}-c_{33}}{2c_{33}}$	$-\frac{\epsilon}{1+2\epsilon}$	$-\epsilon$
$\gamma^{(V)}$	$\frac{c_{66}-c_{44}}{2c_{44}}$	$-\frac{\gamma}{1+2\gamma}$	$-\gamma$
γ	$\frac{c_{44}-c_{66}}{2c_{66}}$	γ	γ

Table 4.1. Anisotropy parameters used to study HTI media and their relation to the generic Thomsen parameters. The c_{ij} representation corresponds to the symmetry axis pointing in the x_1-direction. Parameter f in the equation for $\delta^{(V)}$ is given by $f = 1 - V_{S0}^2/V_{P0}^2$.

For completeness, it should be mentioned that the discussion above can be naturally extended to $S^{\parallel}$-wave propagation in the $[x_1, x_3]$-plane of HTI media. Thomsen's parameter $\gamma^{(V)}$ of the equivalent VTI model (with the corresponding vertical velocity of the fast shear wave $S^{\parallel}$) is defined as

$$\gamma^{(V)} = \frac{c_{66} - c_{44}}{2c_{44}} \tag{4.9}$$

and is related to the generic parameter γ defined with respect to the horizontal symmetry axis as

$$\gamma^{(V)} = -\frac{\gamma}{1+2\gamma}\,. \tag{4.10}$$

Table 4.1 summarizes the coefficients used in this thesis and relates them to the generic Thomsen parameters. Both the exact and approximate (weak-anisotropy) relationships are given.

4.5 *P*-wave reflections in the symmetry-axis plane

The boundary conditions that have to be inverted to obtain the reflection and transmission coefficients are functions of the stiffness-, slowness- and polarization components that are identical for both the HTI and its equivalent VTI model. Therefore, all information required to determine *SV*- and *P*-*P* reflection coefficients is available without any derivation. The exact solution of the VTI reflection problem is valid for reflections in HTI media, as long as the incident wave (of any type) propagates within the symmetry-axis plane. Furthermore, this solution is also valid for interfaces between VTI and HTI media, no matter whether the HTI medium is above or

below the boundary. Exact numerical algorithms designed to evaluate reflection and transmission coefficients in VTI media can thus be used without any modification to compute the reflection response of waves propagating in the symmetry-axis plane of HTI models. For example, algorithms based on Graebner's (1992) exact VTI solution for the reflection/transmission coefficients [equation (3.25)] can be applied to the symmetry-axis plane reflections by simply inserting the correct stiffness coefficients for the HTI model.

One note of caution. The analogy between VTI and HTI media as stated in this work does *not* imply that the value of the reflection coefficients, phase velocities or polarization is identical for VTI and HTI-symmetry-axis plane propagation if the HTI medium is obtained by a 90° rotation of the VTI model. The "equivalent" VTI model introduced above does *not* result from a rotation of the HTI medium but simply denotes the VTI medium that has the same propagation properties for waves traveling in the $[x_1, x_3]$-plane as does the actual HTI model.

The principle of relating properties in the symmetry-axis plane of HTI media with those of VTI media can be applied to equation (3.33), the approximate solution for the *P*-wave VTI reflection coefficient. Then, the approximate *P*-wave reflection coefficient for waves incident within the symmetry-axis plane is given by:

$$\begin{aligned} R_{\mathrm{P}}^{\mathrm{sym}}(\theta) \;=\; & \frac{1}{2}\frac{\Delta Z}{\bar{Z}} + \\ & \frac{1}{2}\left\{\frac{\Delta\alpha}{\bar{\alpha}} - \left(\frac{2\bar{\beta}^{\perp}}{\bar{\alpha}}\right)^2 \frac{\Delta G^{\perp}}{\bar{G}^{\perp}} + \Delta\delta^{(V)}\right\}\sin^2\theta \; + \\ & \frac{1}{2}\left\{\frac{\Delta\alpha}{\bar{\alpha}} + \Delta\epsilon^{(V)}\right\}\sin^2\theta\tan^2\theta \; . \end{aligned} \tag{4.11}$$

Anisotropy coefficients $\delta^{(V)}$ and $\epsilon^{(V)}$ are introduced in equation (4.7) and the superscripts in $\beta^{\perp}$ and $G^{\perp}$ indicate that these quantities correspond to the $S^{\perp}$-wave polarized in the symmetry-axis plane (the SV-wave in the equivalent VTI model); i.e., $\beta^{\perp} = \sqrt{c_{55}/\rho}$ and $G^{\perp} = \rho\beta^{\perp 2}$. The accuracy of approximation (4.11) is identical to the approximation of the VTI *P*-wave reflection coefficient shown in equation (3.33). Also recall that unlike the published VTI approximations, approximations (3.33) and (4.11) are not restricted to small angles of incidence.

Approximation (4.11) provides the first analytic approximation for reflection coefficients in azimuthally anisotropic media. It is simple and concise and allows a profound insight into the physics of the reflection process. The purpose of this analytic study, however, is to understand the azimuthal change in the reflection problem. Therefore, it is important to relate the shear modulus $G^{\perp}$ and the shear velocity $\beta^{\perp}$ of the equivalent VTI model to the properties in the isotropy plane [equation (4.1)]. In the symmetry-axis plane, the *P*-wave is coupled with the $S^{\perp}$-wave which has a different velocity than that of the shear-wave confined to the isotropy plane. The difference between $S^{\parallel}$- and $S^{\perp}$-wave vertical speeds can be expressed through parameter $\gamma^{(V)}$

or, equivalently, through the shear-wave splitting parameter γ. Here, I choose the latter because of its direct relationship to the crack density (this is discussed in more detail below). Using the definition of γ, we find

$$\begin{aligned} \beta^{\perp} &= \beta(1-\gamma) \\ G^{\perp} &= G(1-2\gamma)\,. \end{aligned} \tag{4.12}$$

With this set of parameters, equation (4.11) becomes:

$$\begin{aligned} R_{\mathrm{P}}^{\mathrm{sym}}(\theta) &= \frac{1}{2}\frac{\Delta Z}{\bar{Z}} + \\ &\frac{1}{2}\left\{\frac{\Delta\alpha}{\bar{\alpha}} - \left(\frac{2\bar{\beta}}{\bar{\alpha}}\right)^2\left(\frac{\Delta G}{\bar{G}} - 2\Delta\gamma\right) + \Delta\delta^{(V)}\right\}\sin^2\theta + \\ &\frac{1}{2}\left\{\frac{\Delta\alpha}{\bar{\alpha}} + \Delta\epsilon^{(V)}\right\}\sin^2\theta\tan^2\theta\,, \end{aligned} \tag{4.13}$$

where θ again denotes the incident phase angle.

Both equations (4.13) and (4.11) are valid for HTI media caused by any physical reason. Specifically, their derivation did not assume that the anisotropy is due to vertically aligned cracks. [Schoenberg and Sayers (1995) and Thomsen (1995) have shown that the anisotropy coefficients $\delta^{(V)}, \epsilon^{(V)}$ and γ are not independent in the case of anisotropy introduced by vertically aligned, thin cracks of circular shape.]

The most important message of equation (4.13) is that the contrasts in the anisotropy parameters $\delta^{(V)}$ and γ have a non-negligible, first-order influence on the angular dependence of the reflection coefficient. In fact, if we approximate $\bar{\beta}/\bar{\alpha}$ by $1/2$, the contrast in γ is twice as important as the P-wave contrast $\frac{\Delta\alpha}{\bar{\alpha}}$ in the gradient ($\sin^2\theta$)-term. This raises hopes that a proper inversion procedure may be able to extract these parameters from the AVO-response in the symmetry-axis plane or from the azimuthal variation in the reflection coefficient.

Equation (4.13) is valid for pre-critical incidence on an interface between two weakly anisotropic HTI media with the same symmetry-axis direction and small jumps in the elastic properties across the boundary. Before estimating the accuracy of equation (4.13), a question to be answered is what values of $\epsilon^{(V)}$, $\delta^{(V)}$ and γ can be regarded as physically reasonable. Values of γ obtained in field and laboratory experiments have been positive and generally much smaller than unity ($1 >> \gamma >= 0$) (Crampin, 1984b). In rocks with negligible equant porosity and very thin, fluid-filled cracks $\epsilon^{(V)} = 0$ (Thomsen, 1995); otherwise, $\epsilon^{(V)}$ is small in magnitude and negative ($-1 << \epsilon^{(V)} < 0$) (Tsvankin, 1996c). On the other hand, $\delta^{(V)}$ can be positive or negative.

A special case investigated in more detail in Chapter 8 is that of HTI symmetry caused by vertically aligned, penny-shaped cracks. In this case, the three anisotropy parameters are not independent, and a constraint that couples these parameters is derived in Schoenberg and Sayers (1995) and Thomsen (1995). Using this relation between the anisotropy parameters, Tsvankin (1996c) has shown that $\delta^{(V)}$ is negative

	$\frac{\Delta\alpha}{\bar{\alpha}}$	$\frac{\Delta Z}{\bar{Z}}$	$\frac{\Delta G}{\bar{G}}$	$\delta^{(V)}$	$\epsilon^{(V)}$	γ
Model1	0.1	0.1	0.1	-0.1	0	0
Model2	0.1	0.1	0.1	0.1	0	0
Model3	0.1	0.1	0.1	0	-0.1	0
Model4	0.1	0.1	0.1	0	0	0.1
Model5	0.1	0.1	0.1	0.1	-0.1	0.1
Model6	0.1	0.1	0.1	-0.1	-0.1	0.1
Model7	-0.1	-0.1	-0.1	-0.1	0	0
Model8	-0.1	-0.1	-0.1	0.1	0	0
Model9	-0.1	-0.1	-0.1	0	-0.1	0
Model10	-0.1	-0.1	-0.1	0	0	0.1
Model11	-0.1	-0.1	-0.1	-0.1	-0.1	0.1
Model12	-0.1	-0.1	-0.1	0.1	-0.1	0.1

Table 4.2. Models used to test the accuracy of the approximate reflection coefficients equations (4.13) and (4.2). The upper medium is isotropic, the lower medium has the following parameters: $\alpha_2 = 2.5, \beta_2 = 1.5$ and $\rho_2 = 2.7$. α_2 is the compressional vertical velocity, β_2 is the faster shear-wave vertical velocity and ρ_2 is the density.

for a ratio of the vertical velocities $\beta^{\perp}/\alpha < .707$.

Equation (4.13) is linearized in nine small quantities $\frac{\Delta\alpha}{\bar{\alpha}}, \frac{\Delta Z}{\bar{Z}}$, etc. A total of 45 unknown quadratic terms are dropped in the derivation, and it is not clear how the accuracy of the approximation depends on the medium parameters. In particular, we need to study the accuracy of equation (4.13) for different values of anisotropy parameters $\epsilon^{(V)}$, $\delta^{(V)}$ and γ. Figures 4.5 and 4.6 show the reflection coefficients evaluated at boundaries between isotropic and HTI media for incidence angles up to 40°. Approximations are shown for *P*-wave reflections in both the symmetry-axis plane and the isotropy plane, along with the exact solutions. The model parameters are listed in Table 4.2. The same vertical velocities $\alpha_2 = 2.5$ km/s, $\beta_2 = 1.5$ km/s [equation (4.1)] and a density of 2.7 g/cm^3 in the lower media are used in all these examples. In Figure 4.5, the small contrasts in elastic parameters $\frac{\Delta\alpha}{\bar{\alpha}}$, $\frac{\Delta Z}{\bar{Z}}$ and $\frac{\Delta G}{\bar{G}}$ are positive; in Figure 4.6, all of them are negative. To perform a representative test of equation (4.13) and to study the sensitivity of the approximation with respect to the individual parameters, some models have only one nonzero anisotropic parameter. The tests are done for general HTI media; in the particular case of HTI anisotropy caused by vertically aligned, penny-shaped cracks, the anisotropy coefficients $\epsilon^{(V)}$, $\delta^{(V)}$ and γ are not independent. Several such models will be considered in Chapter 8.

Recall that the isotropy-plane approximation is identical to the conventionally-used approximation for *P*-wave reflection coefficients in isotropic media. The accuracy of the symmetry-axis-plane approximation (4.13) is generally lower than that for the isotropy plane. This is caused by the additional linearizations in anisotropy coefficients and the design of the approximation: instead of using the exact $S^{\perp}$-wave velocity, I

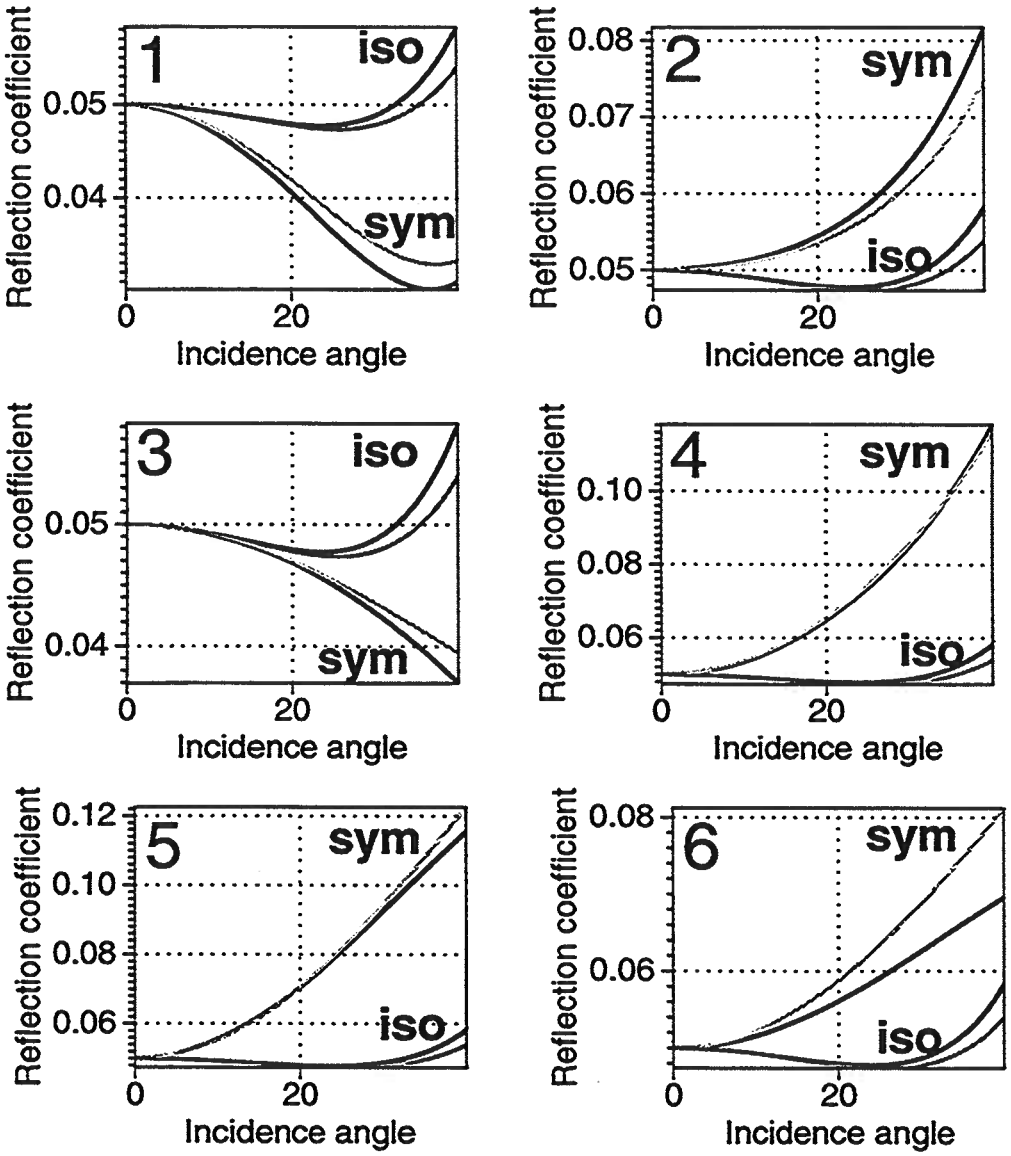

FIG. 4.5. Reflection coefficient for an isotropic layer overlying an HTI medium. Shown are the exact solutions (black) and the approximations based on equations (4.2) and (4.13) (gray) for both symmetry-axis-plane (sym) and isotropy-plane (iso) reflections. Table 4.2 lists the model parameters. $\frac{\Delta\alpha}{\bar{\alpha}}$, $\frac{\Delta Z}{\bar{Z}}$, $\frac{\Delta G}{\bar{G}}$ are positive for all tests.

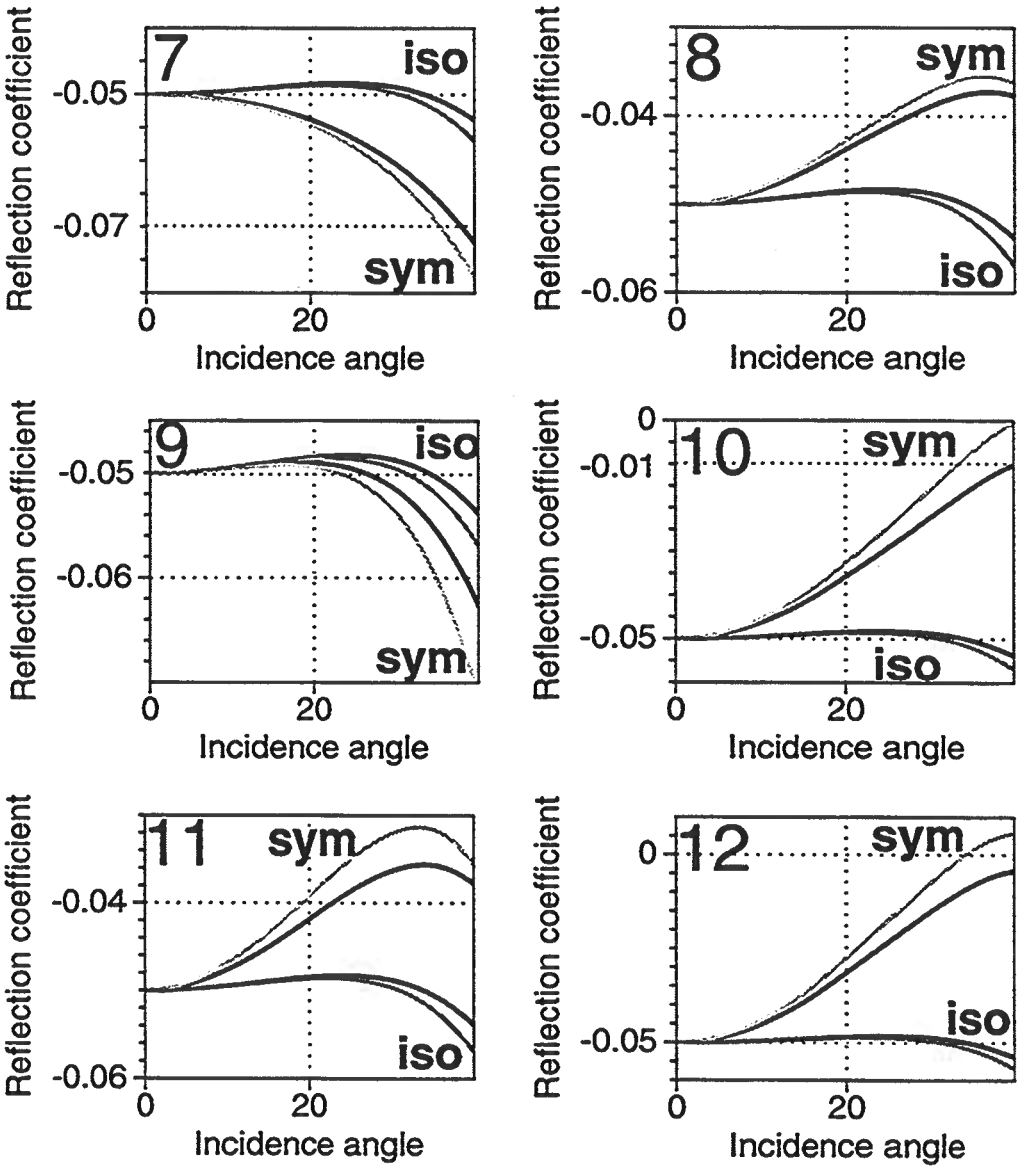

FIG. 4.6. Same as Figure 4.5, except that the parameters $\frac{\Delta\alpha}{\bar{\alpha}}$, $\frac{\Delta Z}{\bar{Z}}$, $\frac{\Delta G}{\bar{G}}$ are negative. Table 4.2 lists the model parameters.

have used a weak-anisotropy approximation in terms of β and γ. If one wants to increase the accuracy, it is better to use equation (4.11) or (preferably) compute the exact reflection coefficient as discussed above. However, despite the additional linearization in γ, the approximations shown in Figures 4.5 and 4.6 provide a good match with the exact solutions: for small angles of incidence, the accuracy is very high while the approximation still provides the correct trend of incidence angles approaching the critical angle. Most importantly, the approximations predict the correct sign and magnitude of the split in the AVO slopes.

The main contribution of the approximations given here is to establish a physical foundation for (exact) numerical inversion algorithms and highlight simple dependencies that interpreters can use to quickly evaluate the magnitude of anisotropy in a particular play. The approximations are not designed to replace the exact calculation, but rather to provide reasonable first guesses for more exact inversion procedures and to predict changes in the reflection-coefficient curves caused by variations in the anisotropy parameters.

Chapter 5

AZIMUTHALLY VARYING P-WAVE REFLECTIVITY

This chapter is a continuation of the symmetry-plane investigations in Chapter 4. Here, the analytic insight gained by deriving approximate P-wave symmetry-plane reflection coefficients is extended to observations at arbitrary azimuth.

5.1 Approximate description of P-wave azimuthal reflectivity variations

Acquisition lines of seismic surveys are not necessarily aligned with the symmetry planes and the symmetry-axis direction may not be known in advance. While the linearized symmetry-plane reflection coefficients conveniently describe the magnitude of azimuthal change in reflectivity between the symmetry planes of HTI media, they do not elucidate the behavior of the reflection coefficients in arbitrary azimuthal directions. Also, as shown in Figure 4.2, the reflection-coefficient curves do not change uniformly even though they are computed at a constant increment in azimuthal angle. Hence, it is important to understand better the functional behavior of the azimuthal variations. Another point of interest is to investigate if anisotropy parameters $\delta^{(V)}, \gamma$ and $\epsilon^{(V)}$ can be extracted individually based on their different dependencies on the azimuthal angle.

The derivation of reflection coefficients in azimuthally anisotropic media involves the study of six wave modes generated by the incident wave. Probably the first results on this topic were obtained (but not published) by Corrigan (1990), who investigated the small-angle response at boundaries between isotropic and orthorhombic media. Using a Born-scattering approach, he derived the dependence of the initial slope of the reflection coefficient (the AVO gradient B) on the source-receiver azimuth in the form

$$B = B^{(0)} + B^{(1)} \cos 2\phi, \tag{5.1}$$

which is consistent with observations on synthetic data by Mallick (1991).

To obtain approximate reflection coefficients for small and large angles of incidence at interfaces between two HTI media, I use a perturbation technique similar to the one applied in Chapter 3 for VTI media. This approach is based upon a perturbation from an isotropic background medium and requires analytic expressions for P-wave polarization vectors, phase velocities and vertical slownesses as functions of the incidence phase angle i and azimuthal phase angle ϕ (Figure 5.1) for weakly anisotropic HTI media.

A derivation of the polarization vectors that does not require investigating the eigenvector problem for the HTI Christoffel matrix is given in Appendix C. The analogy

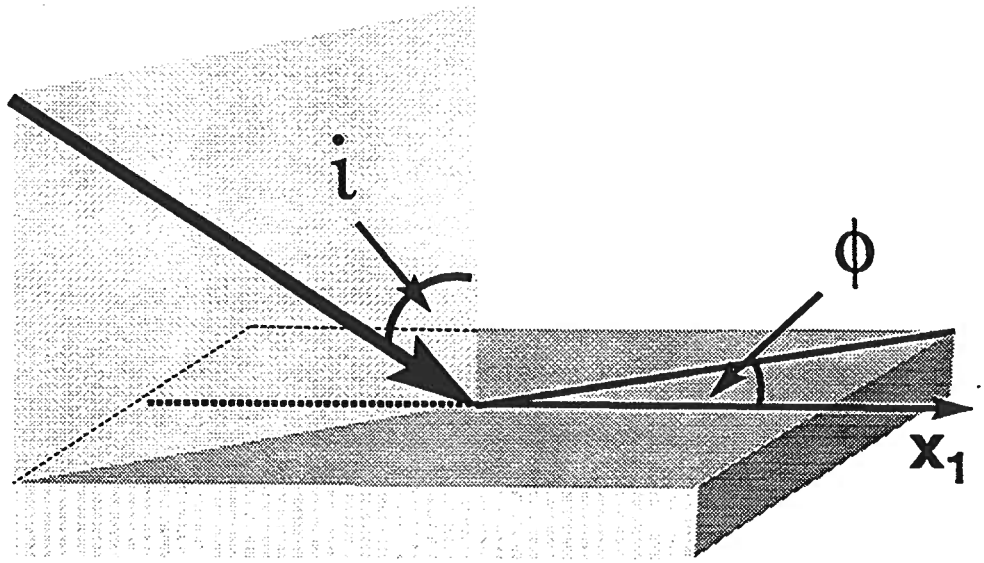

FIG. 5.1. The angle between the slowness vector of the incident wave and vertical is denoted as i. The azimuthal angle ϕ is defined with respect to the symmetry axis pointing in the x_1-direction.

of HTI and VTI media and use of some basic geometry are sufficient to show that the *P*-wave polarization vector $\hat{\mathrm{d}}$ in HTI media can be expressed through the incidence phase angle and azimuthal phase angle as

$$\hat{\mathrm{d}}(i,\phi) = \begin{pmatrix} \mathrm{l}(i,\phi)\sin i\cos\phi \\ \mathrm{m}(i,\phi)\sin i\sin\phi \\ \mathrm{m}(i,\phi)\cos i \end{pmatrix}, \tag{5.2}$$

where m and l are given as

$$\begin{aligned} \mathrm{m}(i,\phi) &= 1 - f\sin^2 i\cos^2\phi\,[\delta^{(V)} + 2(\epsilon^{(V)} - \delta^{(V)})\sin^2 i\cos^2\phi] \\ \mathrm{l}(i,\phi) &= 1 + f\,(1-\sin^2 i\cos^2\phi)\,[\delta^{(V)} + 2(\epsilon^{(V)} - \delta^{(V)})\sin^2 i\cos^2\phi], \end{aligned} \tag{5.3}$$

with $f = \alpha^2/(\alpha^2 - \beta^2)$.

Phase velocities in HTI media as functions of the angle with the symmetry axis and $\epsilon^{(V)}$ and $\delta^{(V)}$ can be derived in a straightforward fashion using the results of Chapter 4, and are given in Tsvankin (1996c). Expressed through the incidence and azimuthal angle, the *P*-wave phase velocity for weak anisotropy takes the following form:

$$V_{P0}(i,\phi) = \alpha\,[1 + \delta^{(V)}\sin^2 i\cos^2\phi + (\epsilon^{(V)} - \delta^{(V)})\sin^4 i\cos^4\phi]. \tag{5.4}$$

Knowledge of the polarizations and phase velocities allows us to set up the perturbation equations for the reflection and transmission coefficients of the waves scattered at HTI/HTI interfaces with the same orientation of the symmetry axis above

and below the interface. This can be done using the same methodology as in Chapter 3, except that M and **b** in equation (3.27) are now 6×6 and 3×6 matrices, respectively.

Denoting the unperturbed quantities with the superscript **u**, the matrix of the linearized reflection coefficients can again be written as

$$\mathbf{\Delta R} = \left(\mathbf{M^u}\right)^{-1} \left(\mathbf{\Delta b} - \mathbf{\Delta M R^u}\right) . \tag{5.5}$$

Here, the operator $\mathbf{\Delta}$ is defined as $\mathbf{\Delta} \equiv d_j \frac{\partial}{\partial d_j}$ with the vector d_j of small deviations from the two identical homogeneous, isotropic media given by

$$d_j = (\frac{\Delta\alpha}{\bar{\alpha}}, \frac{\Delta\beta}{\bar{\beta}}, \frac{\Delta\rho}{\bar{\rho}}, \delta_1^{(V)}, \delta_2^{(V)}, \epsilon_1^{(V)}, \epsilon_2^{(V)}, \gamma_1, \gamma_2)^T . \tag{5.6}$$

The 6×6 matrix $\mathbf{M^u}$ needs to be inverted analytically. This can be achieved using a method developed by Ursin and Haugen (1996) to compute an analytic inverse of the matrix of eigenvectors of the transformed wave equation (Fryer & Frazer, 1987). To find the elements $\mathbf{\Delta b}$ and $\mathbf{\Delta M}$, it is necessary to use the weak-anisotropy approximations for the polarization vectors and phase velocities [equations (5.3) and (5.4)], while the approximate refracted angles can be derived using Snell's law. The compressional plane-wave reflection coefficient can finally be shown to have the following dependence on the incidence (polar) and azimuthal phase angles:

$$\begin{aligned} R_P(i,\phi) \;=\; & \frac{1}{2}\frac{\Delta Z}{\bar{Z}} + \frac{1}{2}\left\{\frac{\Delta\alpha}{\bar{\alpha}} - \left(\frac{2\bar{\beta}}{\bar{\alpha}}\right)^2 \frac{\Delta G}{\bar{G}} + \right. \\ & \left. \left[\Delta\delta^{(V)} + 2\left(\frac{2\bar{\beta}}{\bar{\alpha}}\right)^2 \Delta\gamma\right] \cos^2\phi \right\} \sin^2 i + \\ & \frac{1}{2}\left\{\frac{\Delta\alpha}{\bar{\alpha}} + \Delta\epsilon^{(V)} \cos^4\phi + \Delta\delta^{(V)} \sin^2\phi \cos^2\phi \right\} \sin^2 i \tan^2 i , \end{aligned} \tag{5.7}$$

The simplicity of approximation (5.7) is striking, especially because the equation is linearized only in the small parameters d_j [equation (5.6)] and not in the incidence angle or its trigonometric functions (i.e, no angular terms have been neglected). Specifically, simple trigonometrical relations describe the anisotropic contribution as a function of azimuth. For azimuth $\phi = 90°$, equation (5.7) reduces to equation (4.2), the approximate reflection coefficient for the isotropy plane in HTI media. For the second vertical symmetry plane (the symmetry-axis plane at azimuth $\phi = 0$), the linearized reflection coefficient is identical to equation (4.13), which was derived by using the known VTI approximate reflection coefficient and exploiting the analogy between VTI and HTI media.

Before studying equation (5.7) in more detail, it is instructive to first compare some numerically computed exact reflection coefficients with their linearized approximations. Hereby, the main goal is not to achieve a high numerical accuracy (in that case, more complicated approximations such as those given in Ursin and Haugen (1996)

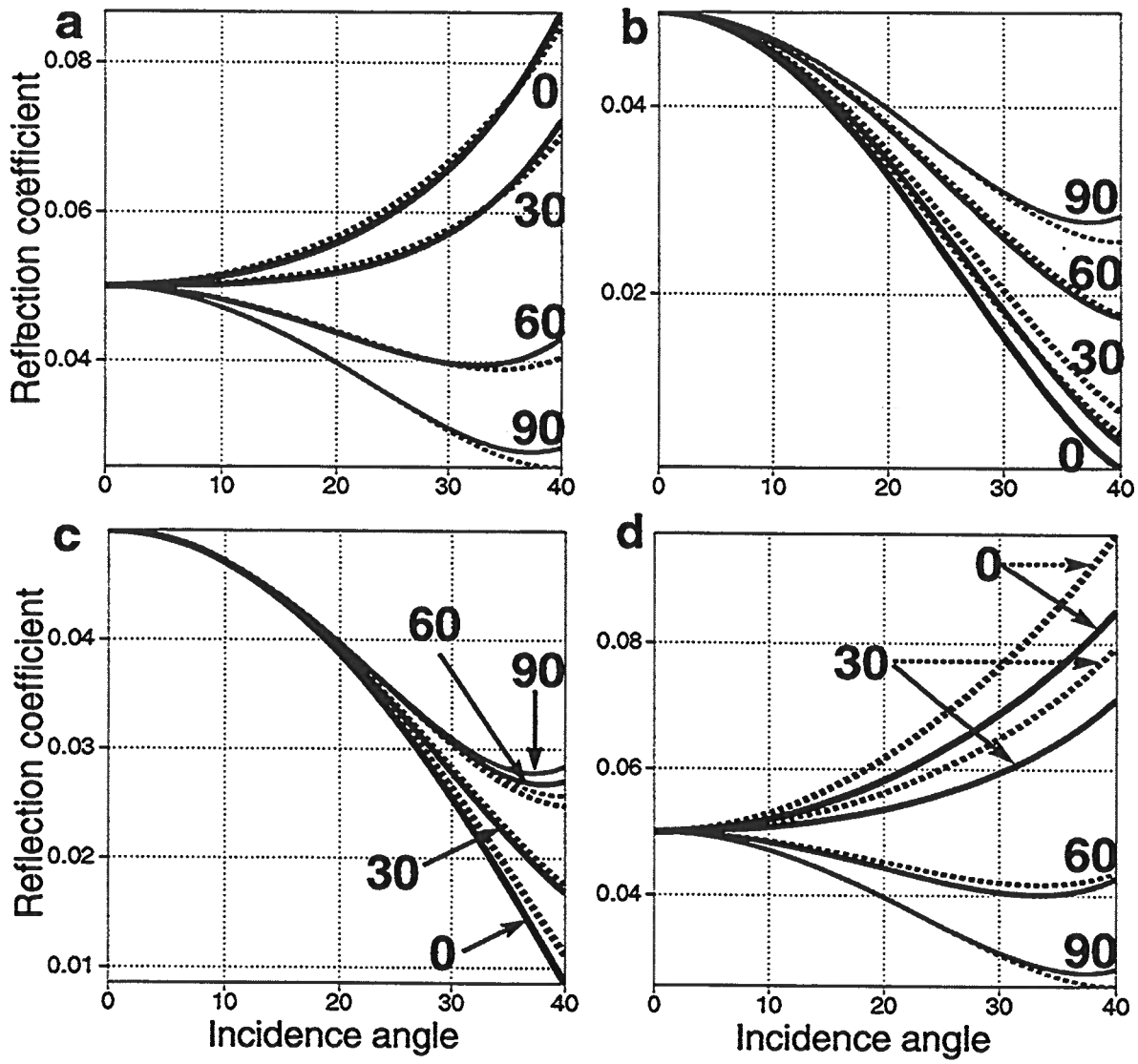

FIG. 5.2. Reflection coefficients for an isotropic layer overlying an HTI medium. Shown are the exact solution (solid lines) and the weak elastic, weak anisotropic approximation (dashed) [equation (5.7)] for azimuths of 0°, 30°, 60° and 90°. Table 5.1 lists the model parameters.

	$\frac{\Delta\alpha}{\bar{\alpha}}$	$\frac{\Delta Z}{\bar{Z}}$	$\frac{\Delta G}{\bar{G}}$	$\delta^{(V)}$	$\epsilon^{(V)}$	γ
Model a	0.1	0.1	0.2	0	0	0.1
Model b	0.1	0.1	0.2	-0.1	0	0
Model c	0.1	0.1	0.2	0	-0.1	0
Model d	0.1	0.1	0.2	-0.05	-0.05	0.15

Table 5.1. Models used to test the accuracy of the approximate reflection coefficient (5.7). The upper medium is isotropic, the lower medium has the following isotropic parameters: compressional vertical velocity $\alpha_2 = 2.5$, faster shear-wave vertical velocity $\beta_2 = 1.5$ and density $\rho_2 = 2.7$.

should be used), but to see if the simple analytic approximation (5.7) of an otherwise incomprehensibly complex reflection coefficient helps to quickly analyze the influence of anisotropy on the reflection signature. In particular, it is instructive to study the accuracy of equation (5.7) for different values of the anisotropy parameters $\epsilon^{(V)}$, $\delta^{(V)}$ and γ. Figure 5.2 shows the reflection coefficients evaluated at boundaries between isotropic and HTI media for azimuths of $0°, 30°, 60°$ and $90°$ and incidence angles up to $40°$. The parameters of the models used in this test are listed in Table 5.1.

The first test shown in Figure 5.2a corresponds to a reflecting HTI medium with a 10% shear-wave splitting parameter ($\gamma = 0.1$). The exact solutions (solid lines, with thickness decreasing with increasing azimuthal angle) and the approximations (dashed) are in very good agreement for all azimuths. The approximations practically coincide with the exact solutions for the $0°$ and $30°$ azimuths, while a small deviation is visible only for azimuths $60°$ and $90°$ and large incidence angles. The second model has a nonzero coefficient $\delta^{(V)}$ in the reflecting medium. Equation (5.7) correctly predicts the spreading of the reflection coefficient curves with azimuth. The slope of the exact curves for $0°$ and $30°$ azimuths is somewhat understated by the approximation and leads to deviations for large angles of incidence. Model c has a nonzero value of parameter $\epsilon^{(V)}$. According to equation (5.7), there should be no significant change in the AVO gradient with azimuth and indeed, the exact solution does not show any split in the reflection coefficient curves for low angles of incidence up to $20°$. Note that the errors of equation (5.7) for the $0°$ and $30°$ azimuths are smaller than those for $90°$ azimuth. The $90°$-azimuth approximation coincides with the classical isotropic linearized expression of the reflection coefficient used sucessfully in conventional AVO analysis. Model d has three nonzero anisotropy parameters, including a shear-wave splitting coefficient of 15%. The approximation has acceptable accuracy for small incidence angles and predicts the correct trend for higher incidence angles. Deviations for large angles of incidence near the symmetry-axis plane are largely caused by the approximate representation of the shear-wave velocity $\beta^{\perp}$ in terms of β and γ. To increase the accuracy in the vicinity of the symmetry-axis plane, the approximation (5.7) should be rewritten in terms of $\beta^{\perp}$.

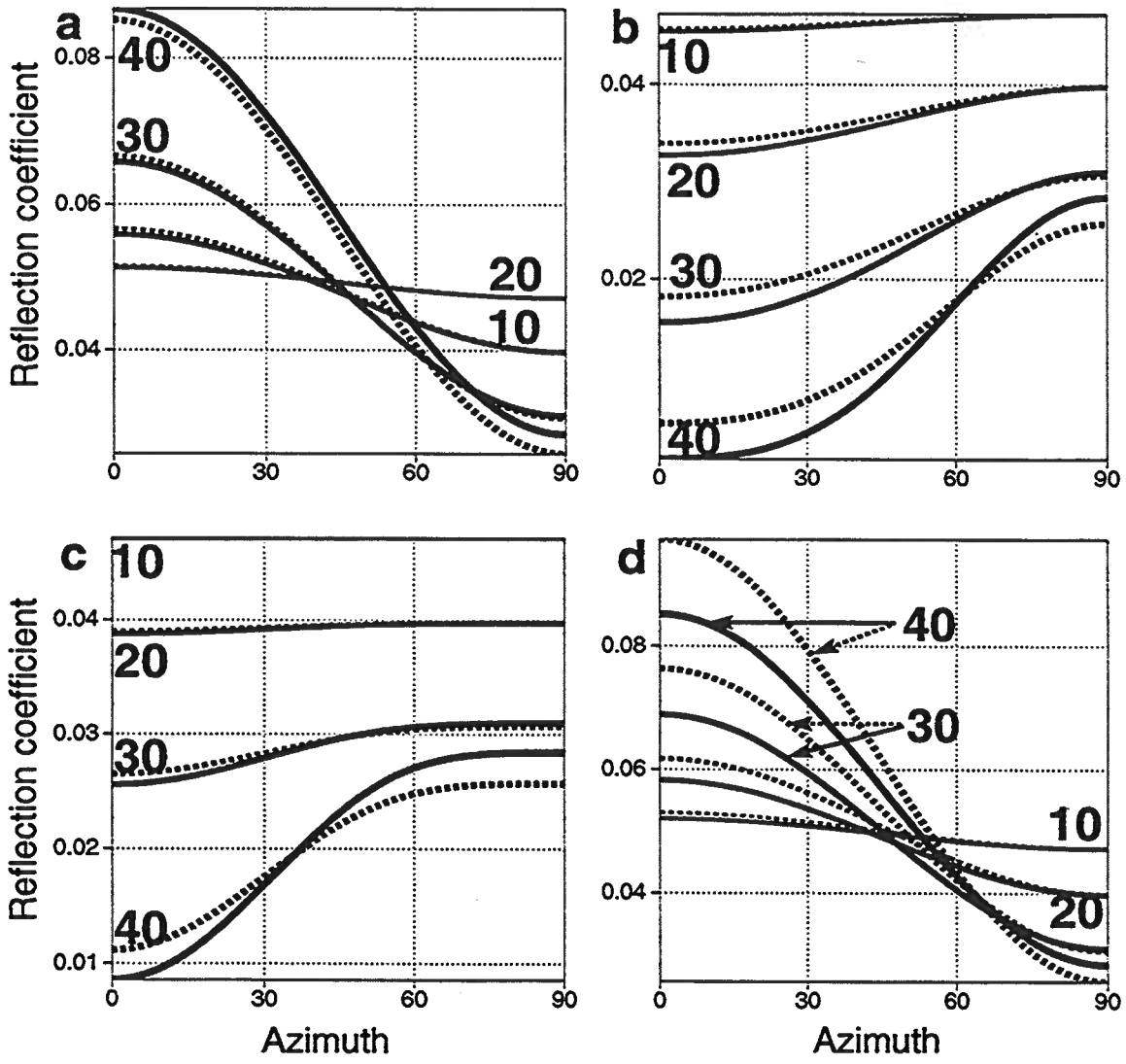

FIG. 5.3. Reflection coefficients for an isotropic layer overlying an HTI medium as a function of the azimuthal phase angle. Shown are the exact solution (solid lines) and the weak elastic, weak anisotropic approximation (dashed) [equation (5.7)] for incidence angles 10°, 20°, 30° and 40°. Note that the reflection coefficient curves computed for Model c and 10° incident angle is invariant with azimuth. Table 5.1 lists the model parameters.

5.2 Functional type of the azimuthal variation

In addition to allowing study of the reflection coefficient as a function of the incidence angle for several azimuths, equation (5.7) enables us to fix the incidence angle and analyze the reflection coefficient as a function of azimuth (Figure 5.3). As seen, the approximations are highly accurate for all azimuths and incidence angles of 10° and 20°. For higher angles, the approximations increasingly deviate from the exact result, but correctly predict the behavior of the azimuthal change. Clearly, the symmetry-plane directions at 0° and 90° azimuth coincide with the extrema of the reflection-coefficient curves plotted as a function of azimuth for fixed incidence angle.

Study of the azimuthal variation in the reflection coefficients can help in finding the orientation of the natural coordinate system of the subsurface without any prior knowledge of the medium parameters. Moreover, because the locations of the extrema are the same for all incidence angles, analysis of stacked data for several azimuths can reveal the symmetry-plane directions, provided that the stacking is performed with the proper (azimuthally varying) normal-moveout velocity. Amplitude analysis on stacked data, however, is not sufficient to distinguish between the symmetry-axis plane and the isotropy plane. For example, the maximum of the reflection curves occurs at the 0° azimuth in Model a, while it is located at the 90° azimuth in Model b.

The curves generated for Model c show several features that are not observed for the other models. First, no azimuthal variation in the reflection coefficient is visible for the 10° incidence angle, and the variation is small for the 20° incidence angle. Additionally, the dependence of the reflection coefficient on azimuth for large angles of incidence is different from the variations observed for the other models. As predicted by the $\cos^4\phi$ term in equation (5.7), a stronger azimuthal change of the reflection coefficient away from the symmetry-axis plane is visible as compared with the azimuthal change close to the isotropy-plane (Figure 5.4).

This discussion of the amplitude variations with offset and azimuth is still primarily qualitative. To relate the observed changes more closely to the medium parameters, let us now consider the implications of equation (5.7) for AVO-with-azimuth analysis.

5.3 Analysis of AVO gradient variations

Equation (5.7) shows that azimuthal anisotropy in HTI media causes a difference between the azimuthal dependence of the AVO gradient and that of the higher-angle term.

The behavior of $R_P(i,\phi)$ at small incidence angles is described by the AVO gradient B composed of the azimuthally invariant part B^{iso} and the anisotropic contribution B^{ani} multiplied with the squared cosine of the azimuthal angle ϕ with the symmetry axis. If the symmetry-axis orientation is unknown, ϕ should be formally expressed by the difference between the azimuthal direction ϕ_k of the k-th observed azimuth and the direction of the symmetry-axis plane ϕ_{sym}. The AVO gradient measured at azimuth

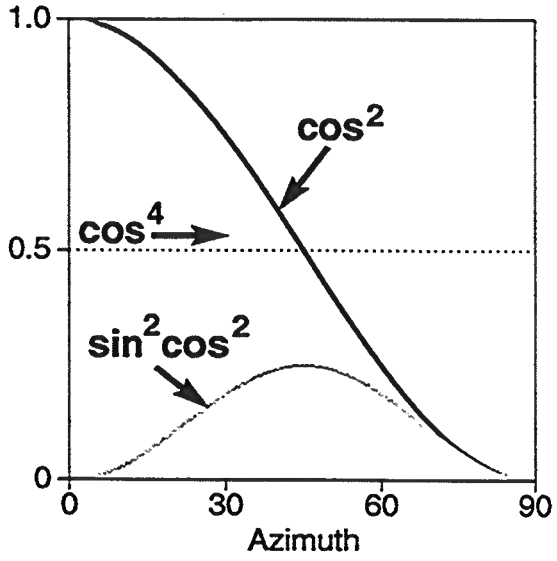

FIG. 5.4. The influence of the anisotropy parameters on the reflection response depends on the azimuthal angle with the symmetry axis. The AVO gradient changes as a function of the squared cosine of azimuth. The higher-angle ($\sin^2 i \tan^2 i$) term contains two parameters with different azimuthal dependences of $\cos^4\phi$ and $\sin^2\phi\cos^2\phi$.

ϕ_k thus can be written as

$$B(\phi_k) = B^{\text{iso}} + B^{\text{ani}} \cos^2(\phi_k - \phi_{\text{sym}}), \tag{5.8}$$

with

$$B^{\text{iso}} = 1/2 \left[\frac{\Delta\alpha}{\bar{\alpha}} - \left(\frac{2\bar{\beta}}{\bar{\alpha}}\right)^2 \frac{\Delta G}{\bar{G}} \right]; \tag{5.9}$$

$$B^{\text{ani}} = 1/2 \left[\Delta\delta^{(V)} + 2\left(\frac{2\bar{\beta}}{\bar{\alpha}}\right)^2 \Delta\gamma \right]. \tag{5.10}$$

Equation (5.8) is nonlinear, with three unknowns (B^{iso}, B^{ani} and ϕ_{sym}). If the direction of the symmetry axis is known (for example, from S-wave data), the equation becomes linear and two independent measurements suffice to solve for B^{iso} and B^{ani}. In multi-azimuth surveys, many more azimuths should be sampled and a least-squares approach can be used to find the optimum values of the unknowns in equation (5.8). Due to the nonlinearity of equation (5.8), the solution will not be unique and will yield two possible directions of the symmetry axis orthogonal to each other. However, a simple rough estimate of the sign of B^{ani} or an a-priori knowledge of the approximate symmetry-axis direction is enough to identify the symmetry-axis direction unambigu-

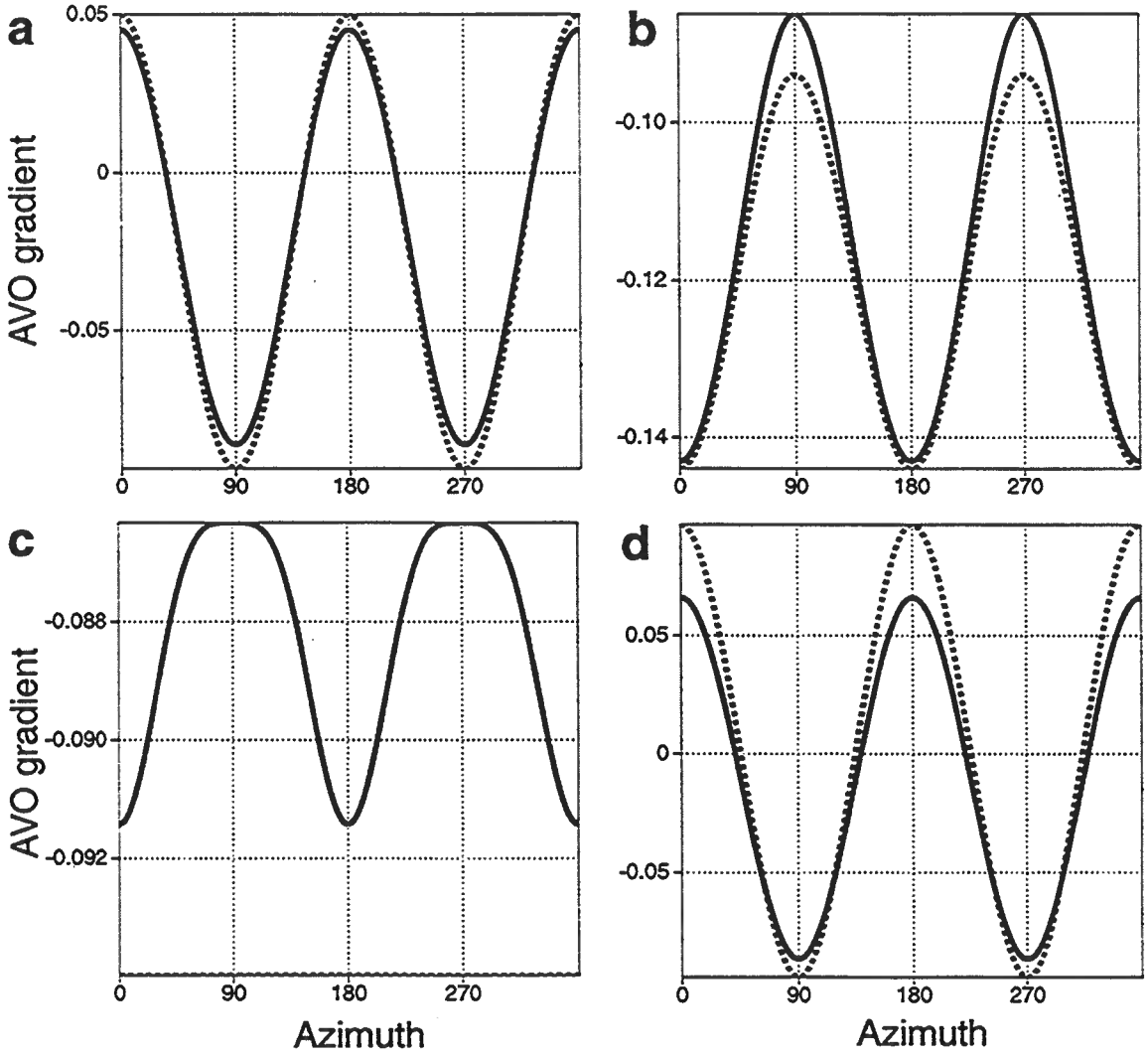

FIG. 5.5. *P*-wave AVO gradient for an isotropic layer overlying an HTI medium as a function of the azimuthal phase angle. The AVO gradients extracted from the exact reflection coefficients are shown as solid lines and dashed lines represent the weak elastic, weak anisotropic approximation based on equation (5.8). Table 5.1 lists the model parameters.

	$B^{\text{ani}}_{\text{observed}}$	$B^{\text{ani}}_{\text{approx}}$
Model a	0.131	0.144
Model b	-0.057	-0.05
Model c	$5.4 \cdot 10^{-3}$	0
Model d	0.152	0.188

Table 5.2. Magnitude of the AVO-gradient variation obtained from the exact reflection coefficient and the value predicted by equation (5.7) for the models given in Table 5.1.

ously.

The dashed lines in Figure 5.5 shows the approximate AVO gradient from equation (5.8). The "exact" gradient (solid line) is computed by simply averaging the slope of the exact reflection coefficient over 0 to 20° incidence angles. The curves shown in Figure 5.5 are evaluated for the models shown in Table 5.1. The extrema denoting the symmetry-plane directions can be easily picked, even though a-priori information is needed to distinguish between the symmetry-axis and the isotropy planes. Table 5.2 compares the magnitude of the observed AVO-gradient change with the value of B^{ani} that would be obtained using equation (5.7).

If $B(\phi_k)$ is known for several ϕ_k's and the AVO gradient does not change sign, an alternative graphical interpretation is possible, and fitting an elliptical curve to the azimuthal variations in AVO gradients can help to determine the symmetry-plane directions and the magnitude of the azimuthal change. The modulus of $B(\phi_k)$ can be assigned to the length of a radius vector at different azimuths ϕ_k. The tip of this vector then delineates a curve that closely resembles an ellipse with the semi-axes aligned with the symmetry-plane directions (see Figure 5.6). The semi-axes have the lengths (B^{iso}) and $(B^{\text{iso}} + B^{\text{ani}})$ and point towards the symmetry-directions of the medium.

An analogous elliptical dependence can be observed for azimuthal changes in NMO velocity. The azimuthal variation of NMO velocity always (except for certain complex areas such as those where common-midpoint reflection time decreases with offset) represents an ellipse in the horizontal plane, with the orientation of the axes determined both by the properties of the medium and the direction of the reflector normal (Grechka & Tsvankin, 1996).

There are several alternative ways to represent $R_P(i,\phi)$. For example, equation (5.7) is consistent with Corrigan's (1990) approximation [equation (5.1)], with

$$\begin{aligned} B^{(0)} &= \frac{\Delta\alpha}{\bar{\alpha}} - \left(\frac{2\bar{\beta}}{\bar{\alpha}}\right)^2 \left(\frac{\Delta G}{\bar{G}} - \Delta\gamma\right) + 1/2\,\Delta\delta^{(V)} \\ B^{(1)} &= \left(\frac{2\bar{\beta}}{\bar{\alpha}}\right)^2 \Delta\gamma + 1/2\,\Delta\delta^{(V)}. \end{aligned} \tag{5.11}$$

In practice, it may happen that $\beta^{\perp}$, the slow vertical shear velocity, is known instead of β. In this case, to achieve a higher accuracy, the AVO gradient in HTI

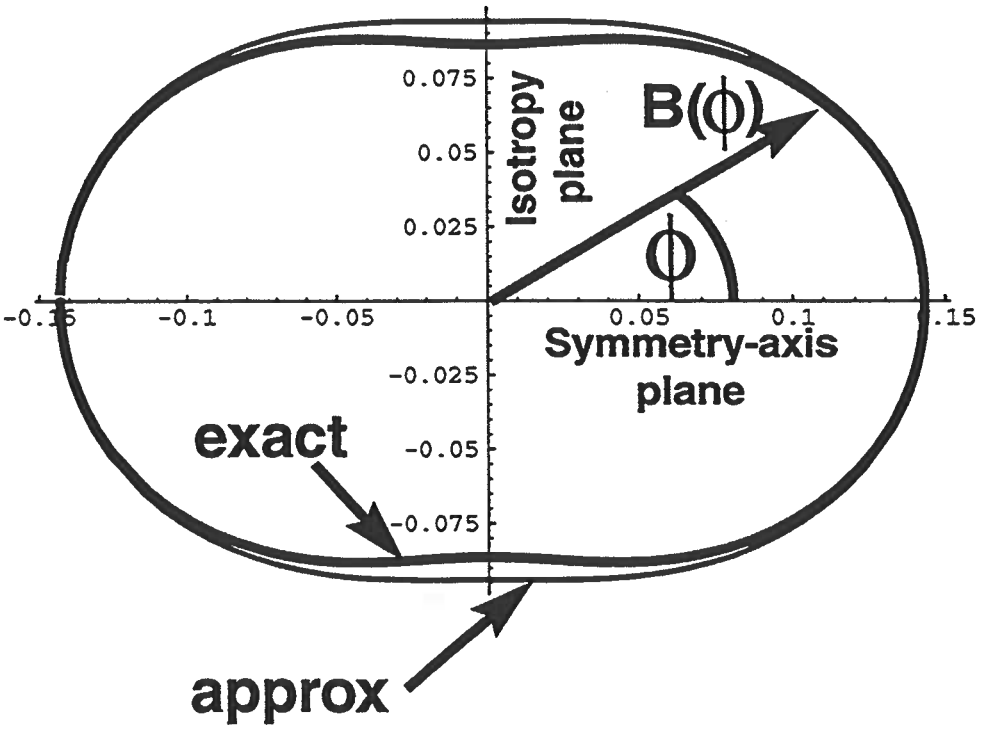

FIG. 5.6. The azimuthal change in AVO gradient can often be described by an close-to-elliptically shaped curve. The curve shown here is delineated by a vector of length B that has been computed for Model b in Table 5.1.

media [equation (5.7)] should be rewritten in terms of $\beta^{\perp}$ rather than β:

$$B(\phi) = 1/2\left(\frac{\Delta\alpha}{\bar{\alpha}} - \left(\frac{2\bar{\beta}^{\perp}}{\bar{\alpha}}\right)^2 \frac{\Delta G^{\perp}}{\bar{G}^{\perp}} + \Delta\delta^{(V)}\cos^2\phi - 2\left(\frac{2\bar{\beta}^{\perp}}{\bar{\alpha}}\right)^2 \Delta\gamma\sin^2\phi\right). \quad (5.12)$$

5.4 AVO-gradient inversion in HTI media

To eliminate the "isotropic" quantities in equation (5.9) in the special case of inverting AVO measurements in the isotropy and symmetry-axis planes, it is best to use the difference between the AVO gradients measured in the symmetry and isotropy planes rather than inverting the gradients individually. Keeping just the two lowest-order terms and assuming that the incidence layer is isotropic, we find

$$B(\phi_{\text{sym}}) - B(\phi_{\text{sym}} + \pi/2) \cong \left\{\left(\frac{2\bar{\beta}}{\bar{\alpha}}\right)^2 \gamma_2 + \frac{1}{2}\delta_2^{(V)}\right\}. \quad (5.13)$$

Equation (5.13) shows that the difference in the gradient depends on just two anisotropic parameters – the shear wave splitting parameter and the coefficient $\delta_2^{(V)}$. For $\bar{\beta}/\bar{\alpha} \approx 1/2$, the difference between the gradient terms becomes simply $\gamma_2 + \frac{1}{2}\delta_2^{(V)}$. This means that the weighting factor for the shear-wave splitting parameter is twice as large as that for $\delta_2^{(V)}$. As shown by Tsvankin (1996c), the parameter $\delta_2^{(V)}$ can be obtained from P–wave normal-moveout (NMO) velocities. If $\delta_2^{(V)}$ has been determined, the difference in the gradients can be inverted for the shear-wave splitting parameter, which (for penny-shaped cracks) is close to the crack density, given an approximate value of the ratio $\frac{2\bar{\beta}}{\bar{\alpha}}$. Also, the crack density can be obtained directly from the difference $[B(\phi_{\text{sym}}) - B(\phi_{\text{sym}} + \pi/2)]$ in the important special case of the vanishing parameter ϵ ($\epsilon = \epsilon^{(V)} = 0$), typical for fractured, fluid-filled coal layers. If $\epsilon = 0$, then $\delta^{(V)} \approx -\gamma$ (Tsvankin, 1996c), and the crack density remains the only anisotropic parameter in equation (5.13).

While it is clear that $\Delta\gamma$ and $\Delta\delta^{(V)}$ are responsible for the magnitude of the azimuthal variation, equation (5.7) shows that both coefficients cause the same functional behavior of azimuthal change and cannot be inverted separately. Hence, one of the important lessons learned from the studies of the approximate AVO gradient is that the difference in the shear-wave splitting parameter $\Delta\gamma$ and $\Delta\delta^{(V)}$ cannot be determined separately because both parameters influence the azimuthally dependent AVO-gradient in the same way. Equation (5.7) additionally predicts that picking the extrema of the azimuthal AVO-gradient variation yields two possible directions of the symmetry axis. Only if some prior information on the symmetry-axis direction (for example from geologic data) or on the anisotropy parameters is available can the symmetry-axis direction be delineated unambiguously.

5.5 Azimuthal variation of the higher-angle term

For incidence angles $i > 20°$, both the AVO gradient term *and* the higher-angle term will influence the reflection coefficient. For azimuthal directions close to the symmetry axis and large incidence angles, the coefficient $\epsilon^{(V)}$ will have a significant impact on the azimuthally variable reflection coefficient.

Here, I discuss the interesting special case of reflection coefficients with small or even nonexistent AVO gradient variations (i.e., the term $[\Delta\delta^{(V)} + 2\left(\frac{2\bar{\beta}}{\bar{\alpha}}\right)^2 \Delta\gamma]$ is negligibly small). In this case, equation (5.7) still predicts an azimuthal change in the reflection coefficient at large angles of incidence for nonzero values of $\Delta\epsilon^{(V)}$ and $\Delta\delta^{(V)}$. Note that these parameters have different influences on the azimuthal change of the reflection coefficient. The influence of $\Delta\delta^{(V)}$ on the large-angle reflection response reaches its maximum at an azimuth of 45° while $\Delta\epsilon^{(V)}$ is primarily responsible for the azimuthal variation of the large-angle term for azimuths close to the symmetry-axis plane.

The appearance of $\Delta\delta^{(V)}$ in the $\sin^2\tan^2$-term is somewhat surprising because this term does not enter the isotropy-plane coefficient (4.2) or the symmetry-axis plane coefficient (4.11). However, the impact of $\Delta\delta^{(V)}$ is significant only for azimuthal angles close to 45°, where the influence of $\Delta\delta^{(V)}$ and $\Delta\epsilon^{(V)}$ are comparable (see Figure 5.4). Consequently, $\Delta\epsilon^{(V)}$ is the parameter that mostly controls the azimuthal variation.

5.6 Azimuthal changes of the transmission coefficient

AVO analysis of surface data, as well as borehole studies in vertically stratified media also can include the investigation of transmission phenomena. The derivations above yield the following linearized *P*-wave transmission coefficient at interfaces between two weakly anisotropic HTI media with the same direction of the symmetry axis:

$$\begin{aligned} T_P(i,\phi) \;=\; & 1 - \frac{1}{2}\frac{\Delta Z}{\bar{Z}} + \\ & \frac{1}{2}\left\{\frac{\Delta\alpha}{\bar{\alpha}} + \Delta\delta^{(V)}\cos^2\phi\right\}\sin^2 i + \\ & \frac{1}{2}\left\{\frac{\Delta\alpha}{\bar{\alpha}} + \Delta\epsilon^{(V)}\cos^2\phi + \right. \\ & \left.\Delta\delta^{(V)}\sin^2\phi\cos^2\phi\right\}\sin^2 i\tan^2 i + \\ & \left\{(\Delta\epsilon^{(V)} - \Delta\delta^{(V)})\cos^2\phi\right\}\sin^4 i\,. \end{aligned} \tag{5.14}$$

Unlike the linearized reflection coefficient, $T_P(i,\phi)$ contains no dependence on the shear-wave splitting parameter or the shear-wave vertical velocity. The difference in $\delta^{(V)}$ is the only term responsible for the azimuthal variation in the AVO-gradient term. For higher angles of incidence, two terms ($\sin^4 i$ and $\sin^2 i\tan^2 i$) with more

complicated azimuthal dependence of the anisotropic parameters become increasingly important.

Chapter 6

SHEAR WAVES IN HTI SYMMETRY PLANES

So far, the discussion has been focused on P-wave reflection coefficients. In current exploration practice, however, shear-wave surveys are also acquired and interpreted for the presence of azimuthal anisotropy (Lynn *et al.*, 1995; Kendall, 1995). The main objective of such studies is to relate the anisotropy (determined from conventional shear-wave splitting analysis) to the fracture parameters of the medium. Azimuthal anisotropy has a first-order influence on vertically incident shear waves causing them to split into two orthogonally polarized components traveling with different velocities. The parameter of crack systems of great interest in exploration is the crack density, which is close to the fractional difference between the velocities of split shear waves at vertical incidence and can be approximated by Thomsen's (1986) coefficient γ. Estimates of anisotropy using the time delay between the fast and slow shear waves yield robust measurements of γ averaged over the propagation path of the shear waves within the medium. Thus, analysis of shear-wave traveltimes via the classical rotation analysis of Alford (1986) helps to estimate the crack density (for HTI media), albeit with a low vertical resolution. This chapter discusses the feasibility of using shear-wave reflection amplitudes at oblique incidence angles to estimate the anisotropy parameters.

6.1 Shear-wave surveys perpendicular and parallel to fracture strike

The survey geometry in Figure 6.1 is similar to that of shear-wave experiments by Lynn and Thomsen (1990) and Lynn et al. (1995). As described in the previous chapter, the $S^{\parallel}$-wave polarization is confined to the fracture plane (or isotropy plane) whereas the $S^{\perp}$-wave is polarized in the plane formed by the slowness vector and the symmetry axis. Let us first consider an AVO experiment carried out along the fracture strike (in the isotropy plane) on the surface of a two-layer model. It is hereby assumed that both layers are fractured in the same direction, but with different fracture density. If the source is oriented in the strike direction, it generates an $S^{\parallel}$-wave polarized within the fracture plane. Since in this plane, the shear-wave velocity is independent of the propagation angle, the approximate reflection coefficient is identical to the isotropic SV-wave reflection coefficient [equation (2.23)]:

$$R_{S\parallel}^{\text{strike}} = R_{SV}^{\text{iso}}, \tag{6.1}$$

with V_S in R_{SV}^{iso} replaced by $\beta = \sqrt{c_{44}/\rho}$, i.e., the velocity of the S-wave polarized within the fracture plane. For a survey aligned with the fracture strike, the $S^{\perp}$-wave is

polarized perpendicular to the vertical propagation plane. Therefore, its approximate reflection coefficient has the form of equation (2.22) for the isotropic SH-wave:

$$R_{S^\perp}^{\text{strike}} = R_{SH}^{\text{iso}}, \tag{6.2}$$

where V_S in R_{SH}^{iso} needs to be replaced by the correct (slow) shear velocity $\beta^\perp = \sqrt{c_{55}/\rho}$.

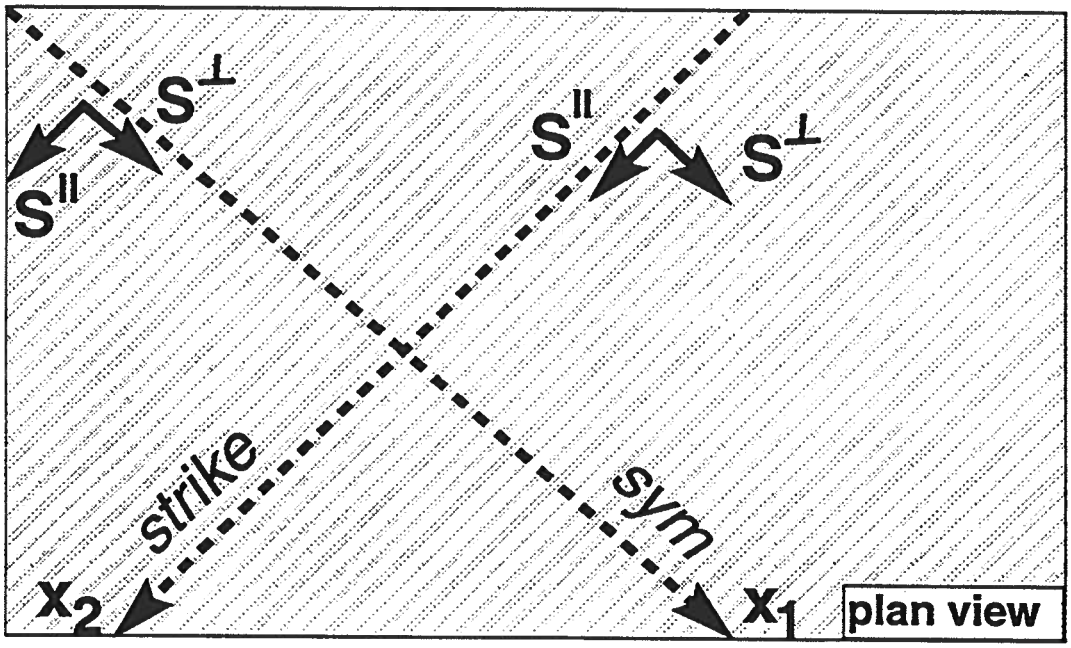

FIG. 6.1. Sketch of a shear-wave experiment in the presence of aligned near-vertical cracks (plan view). Arrows show the polarization directions of $S^{\parallel}$ and $S^{\perp}$ waves. Amplitude analysis will be carried in the isotropy plane parallel to the fracture strike (x_2-direction) and in the symmetry-axis direction (x_1-direction).

Let us now consider a survey line acquired along the axis of symmetry (the x_1-axis in Figure 6.1). Fortunately, the derivations necessary for this study are rather straightforward if one applies the analogy between wave propagation in the $[x_1, x_3]$-plane of HTI and VTI models discussed in Chapter 4. This limited analogy allows one to obtain the approximate reflection coefficient $R_{S^\perp}^{\text{sym}}$ from equation (3.34):

$$R_{S^\perp}^{\text{sym}} = R_{SV}^{\text{iso}} + 1/2 \left(\frac{\bar{\alpha}}{\bar{\beta}^\perp}\right)^2 (\Delta\epsilon^{(V)} - \Delta\delta^{(V)}) \sin^2 j, \tag{6.3}$$

with V_S in R_{SV}^{iso} [equation (2.23)] being replaced by $\beta^\perp$, the vertical velocity of the shear wave polarized in the symmetry-axis plane. $\bar{\alpha}$ in equation (6.3) denotes the average vertical P-wave velocity. Arguments similar to those in the derivation of $R_{S^\perp}^{\text{sym}}$

make it possible to obtain the reflection coefficient for the $S^{\parallel}$-wave:

$$R_{S^{\parallel}}^{sym} = R_{SH}^{iso} + 1/2\,\Delta\gamma^{(V)}\,\tan^2 j\,. \tag{6.4}$$

Here, the V_S-term in R_{SH}^{iso} [equation (2.22)] corresponds to the vertical $S^{\parallel}$-wave velocity. Angles j in equations (6.3) and (6.4) denote phase angles of the incident shear waves.

6.2 Insight into shear-wave AVO

Application of the developed analytic results requires finding a set of parameters suitable for comparison of the individual shear-wave reflection coefficients. Obviously, for anisotropic media, $\beta(\doteq \beta^{\parallel}) \neq \beta^{\perp}$. As mentioned above, the parameter of most interest in reservoir characterization is the crack density, which is proportional to the product of the number of cracks per unit volume and their mean cubed diameter. Since the crack density for penny-shaped cracks is close to the shear-wave splitting parameter γ (Tsvankin, 1996c), I will retain γ in the expressions for both shear waves. From the definition of anisotropy parameter γ, it follows that

$$\begin{aligned} \beta^{\perp} &= \frac{\beta}{\sqrt{1+2\gamma}} \approx \beta\,(1-\gamma)\,, \\ \frac{\Delta\beta^{\perp}}{\bar{\beta}^{\perp}} &\approx \frac{\Delta\beta}{\bar{\beta}} + \gamma_1 - \gamma_2\,, \end{aligned} \tag{6.5}$$

accurate to first order in γ. $\frac{\Delta\beta}{\bar{\beta}}$ will denote the relative change in fast shear-wave velocity for the remainder of this thesis.

To understand better the accuracy of this approximation, I compute $\frac{\Delta\beta^{\perp}}{\bar{\beta}^{\perp}}$ as a function of γ (the upper medium is isotropic) for two values of $\frac{\Delta\beta}{\bar{\beta}}$ (Figure 6.2). Shown are the exact solutions (solid lines) and the approximations based on equation (6.5). For increasing γ, the contrast in $\beta^{\perp}$ decreases because the velocity for shear waves polarized perpendicular to the fractures becomes smaller. The approximations show modest deviation from the exact result. However, even this small deviation can have an observable influence on the reflection coefficient. Since the reflection response is formed by small differences in the elastic constants across the boundary, inaccuracies of the size observed in Figure 6.2 can be significant.

Using the relation between the vertical shear velocities shown in equation (6.5), the $R_{S^{\perp}}^{strike}$ reflection coefficient can be expressed through the fast vertical shear wave velocity. Both reflection coefficients for shear waves traveling in the fracture plane [equations (6.1) and (6.2)] can then be conveniently expressed as follows:

$$R_{S^{\parallel}}^{strike} = -1/2\,\frac{\Delta Z^S}{\bar{Z}^S} + \left(\frac{7}{2}\frac{\Delta\beta}{\bar{\beta}} + 2\frac{\Delta\rho}{\bar{\rho}}\right)\sin^2 j - 1/2\,\frac{\Delta\beta}{\bar{\beta}}\sin^2 j\,\tan^2 j$$

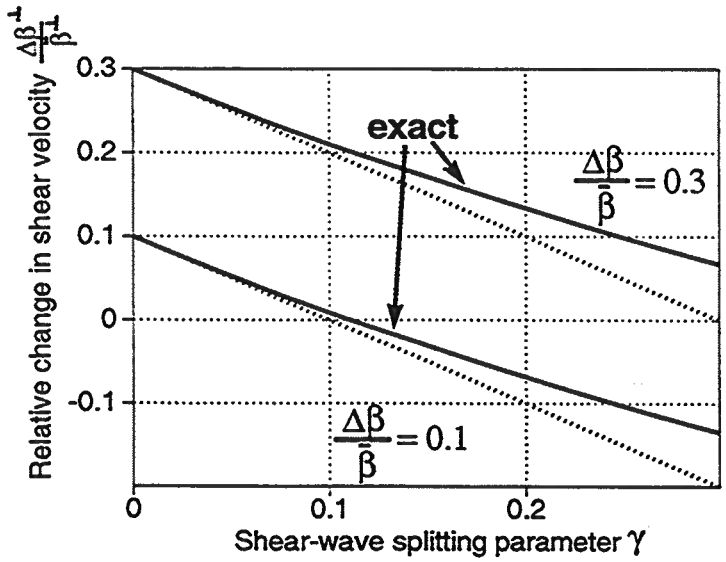

FIG. 6.2. Relative change in $\beta^{\perp}$ as a function of γ (the upper medium is isotropic) for two values of $\frac{\Delta\beta}{\bar{\beta}}$. Shown are the exact results (solid lines) and approximations from equation (6.5) (dashed).

$$R_{S^{\perp}}^{\text{strike}} = -1/2 \left(\frac{\Delta Z^S}{\bar{Z}^S} - \Delta\gamma \right) + 1/2 \left(\frac{\Delta\beta}{\bar{\beta}} - \Delta\gamma \right) \tan^2 j, \tag{6.6}$$

where ($Z^S = \rho\beta$) denotes the shear-wave impedance for the vertically-incident fast S-wave. For weak anisotropy, i.e., small moduli of the anisotropy parameters, the difference between $R_{S^{\parallel}}^{\text{strike}}$ and $R_{S^{\perp}}^{\text{strike}}$ at normal incidence is equal to half the difference in anisotropy parameter γ across the reflecting interface (Thomsen, 1988). This information can be combined with an estimate of the AVO gradient extracted from the $S^{\perp}$ data set to yield $\frac{\Delta\beta}{\bar{\beta}}$. The last parameter of interest, $\frac{\Delta\rho}{\bar{\rho}}$, can be calculated from the $S^{\parallel}$-wave AVO gradient.

Shear-wave AVO analysis along the fracture-strike direction has the potential of uniquely determining the difference in the elastic parameters across a reflecting boundary. In a noisy environment, it may be desirable to further constrain the inversion by including additional information. A similar analysis, for example, is possible for the higher-angle ($\sin^2 j \tan^2 j$) term, but it is unlikely that this coefficient can be reliably extracted from field data; polarization and amplitude distortions for post-critically-incident shear waves can prohibit application of AVO analysis.

Another option is AVO analysis of shear waves propagating normal to the fractures. Clearly, for vertical incidence, there is no distinction between wave propagation in the symmetry-axis plane or the fracture plane. However, the AVO gradients in the symmetry-axis plane are different from those in the fracture plane and these variations

can be helpful in the inversion for medium parameters. Taking into account that for weak anisotropy $\gamma^{(V)} \approx -\gamma$ [equation (4.8)], we find

$$\begin{aligned} \mathrm{R}_{S^{\parallel}}^{\mathrm{sym}} &= -\frac{1}{2}\frac{\Delta Z^S}{\bar{Z}^S} + \frac{1}{2}\left(\frac{\Delta\beta}{\bar{\beta}} - \Delta\gamma\right)\tan^2 j \\ \mathrm{R}_{S^{\perp}}^{\mathrm{sym}} &= -\frac{1}{2}\left(\frac{\Delta Z^S}{\bar{Z}^S} - \Delta\gamma\right) + \left\{\frac{7}{2}\left(\frac{\Delta\beta}{\bar{\beta}} - \Delta\gamma\right) + 2\frac{\Delta\rho}{\bar{\rho}} + \right. \\ &\quad \left. \frac{1}{2}\left(\frac{\bar{\alpha}}{\bar{\beta}}\right)^2 (\Delta\epsilon^{(V)} - \Delta\delta^{(V)})\right\}\sin^2 j - \frac{1}{2}\left(\frac{\Delta\beta}{\bar{\beta}} - \Delta\gamma\right)\sin^2 j \tan^2 j . \quad (6.7) \end{aligned}$$

If the difference $\Delta\gamma = (\gamma_2 - \gamma_1)$ is extracted from the shear-wave normal-incidence reflection coefficients, the AVO gradient of the $S^{\parallel}$-wave can then be used to find $\frac{\Delta\beta}{\bar{\beta}}$. Unlike the $S^{\parallel}$-wave, which solely depends on $\frac{\Delta\beta}{\bar{\beta}}$ and γ, the $S^{\perp}$ wave is additionally influenced by the difference of $(\delta^{(V)} - \epsilon^{(V)})$. $(\delta^{(V)} - \epsilon^{(V)})$, as demonstrated by Tsvankin (1996c), is close to the anisotropy coefficient η (Alkhalifah & Tsvankin, 1995) needed for time processing in the symmetry-axis plane of HTI media. Moreover, the parameter combination $(\delta^{(V)} - \epsilon^{(V)})$ will change significantly for different contents of the cracks, hence shear-wave AVO has the potential of not only estimating the shear-wave splitting parameter, but also to infer the nature of the crack filling.

Certainly, the additional linearizations used to derive equations (6.6) and (6.7) may reduce the accuracy of the approximation. The quality of the approximation and the variations of the reflection coefficients from one symmetry plane to the other are studied for four different combinations of isotropic/HTI interfaces in Figure 6.3 (model parameters given in Table 6.1). The first model has only one nonzero anisotropy parameter $\delta_2^{(V)}$. Equations (6.6) and (6.7) correctly predict an identical, moderately negative AVO gradient for $R_{S^{\perp}}^{\mathrm{strike}}$ and $R_{S^{\parallel}}^{\mathrm{sym}}$ and a more negative gradient for $R_{S^{\parallel}}^{\mathrm{strike}}$ than for $R_{S^{\perp}}^{\mathrm{sym}}$. The accuracy of the approximations is sufficiently high for all four examples. Model b has a zero value of $\epsilon_2^{(V)}$, typical for tight formations with saturated cracks. Although the $S^{\parallel}$-wave reflection curves are vertically shifted with respect to the $S^{\perp}$ curves due to the different normal-incidence reflection coefficients, $R_{S^{\perp}}^{\mathrm{strike}}$ and $R_{S^{\parallel}}^{\mathrm{sym}}$ have similar gradients (in the weak anisotropy limit, both $R_{S^{\perp}}^{\mathrm{strike}}$ and $R_{S^{\parallel}}^{\mathrm{sym}}$ have the same AVO gradient). The $R_{S^{\perp}}^{\mathrm{sym}}$ gradient, on the other hand, is negative and larger in absolute value than is the $R_{S^{\parallel}}^{\mathrm{strike}}$ gradient. The same observation can be made for Model c, with nonzero anisotropy parameters $\epsilon^{(V)}$, $\delta^{(V)}$ and γ in the lower medium. Finally, a model of elliptical anisotropy ($\delta_2^{(V)} = \epsilon_2^{(V)}$) and 5 % shear wave splitting parameter ($\gamma = 0.05$) is used in Model d. Here, the normal incidence reflection coefficients are negative and the reflection coefficients are decreasing in absolute value with increasing angle of incidence. The approximate solution provides a good estimate of the exact reflection coefficient curves.

Note that equations (6.6) and (6.7) include the exact $S^{\parallel}$-wave vertical velocity while the $S^{\perp}$-wave vertical velocity is approximated. The difference in accuracy between the $S^{\parallel}$ and $S^{\perp}$ coefficients is therefore just a matter of the design of the

	Model a	Model b	Model c	Model d
$\frac{\Delta\alpha}{\bar{\alpha}}$	-0.1	0.1	-0.1	0.1
$\frac{\Delta\beta}{\bar{\beta}}$	-0.15	-0.15	-0.1	0.1
$\frac{\Delta\rho}{\bar{\rho}}$	-0.15	-0.15	-0.1	0.1
$\epsilon_2^{(V)}$	0	0	-0.11	-0.11
$\delta_2^{(V)}$	-0.15	-0.067	-0.18	-0.11
γ	0	0.15	0.15	0.05

Table 6.1. Model parameters used in the numerical tests shown in Figure 6.3. The vertical P and $S^{\parallel}$-wave velocities of the lower medium are 2.69 km/s and 1.4 km/s; its density is 2.07 g/cm^3. The upper medium is purely isotropic.

approximations. It is straightforward to rewrite equations (6.6) and (6.7) as functions of $\frac{\Delta\beta^{\perp}}{\beta^{\perp}}$, if this parameter can be estimated more accurately than $\frac{\Delta\beta}{\bar{\beta}}$.

The examples shown in Figure 6.3 demonstrate that the derived approximations are sufficiently accurate for both positive and negative jumps in the relative difference in the isotropic parameters across the reflecting boundary and small values of anisotropy parameters. Moreover, in addition to independent study of the AVO gradients for each wavetype, the form of equations (6.6) and (6.7) suggests using the differences in the AVO gradients for S-waves propagating in the vertical symmetry planes of HTI media. Keeping just the lowest-order term and denoting $\Delta\sigma^{(V)} = \left(\frac{\bar{\alpha}}{\bar{\beta}}\right)^2 (\Delta\epsilon^{(V)} - \Delta\delta^{(V)})$, we find the following differences in the reflection coefficients:

$$
\begin{aligned}
\mathrm{R}_{S^{\parallel}}^{\mathrm{sym}} - \mathrm{R}_{S^{\perp}}^{\mathrm{strike}} &= -1/2\,\Delta\gamma \\
\mathrm{R}_{S^{\parallel}}^{\mathrm{strike}} - \mathrm{R}_{S^{\perp}}^{\mathrm{strike}} &= -1/2\,\Delta\gamma + \left(3\frac{\Delta\beta}{\bar{\beta}} + 2\frac{\Delta\rho}{\bar{\rho}} + 1/2\,\Delta\gamma\right)\sin^2 j \\
\mathrm{R}_{S^{\perp}}^{\mathrm{sym}} - \mathrm{R}_{S^{\parallel}}^{\mathrm{strike}} &= 1/2\,\Delta\gamma + \left(-7/2\,\Delta\gamma + 1/2\,\Delta\sigma^{(V)}\right)\sin^2 j \\
\mathrm{R}_{S^{\parallel}}^{\mathrm{sym}} - \mathrm{R}_{S^{\parallel}}^{\mathrm{strike}} &= -\left(3\frac{\Delta\beta}{\bar{\beta}} + 2\frac{\Delta\rho}{\bar{\rho}} + 1/2\,\Delta\gamma\right)\sin^2 j \\
\mathrm{R}_{S^{\perp}}^{\mathrm{sym}} - \mathrm{R}_{S^{\perp}}^{\mathrm{strike}} &= \left(3\left(\frac{\Delta\beta}{\bar{\beta}} - \Delta\gamma\right) + 2\frac{\Delta\rho}{\bar{\rho}} + 1/2\,\Delta\sigma^{(V)}\right)\sin^2 j \\
\mathrm{R}_{S^{\parallel}}^{\mathrm{sym}} - \mathrm{R}_{S^{\perp}}^{\mathrm{sym}} &= -1/2\,\Delta\gamma - \left(3\left(\frac{\Delta\beta}{\bar{\beta}} - \Delta\gamma\right) + 2\frac{\Delta\rho}{\bar{\rho}} + 1/2\,\Delta\sigma^{(V)}\right)\sin^2 j \qquad (6.8)
\end{aligned}
$$

Four combinations of the reflection coefficients involving two different modes allow us to obtain the shear-wave splitting parameter from the difference in the normal-incidence reflection coefficient. Additionally, five equations for the differences in the AVO gradients can be solved for the four unknowns $\frac{\Delta\beta}{\bar{\beta}}$, $\frac{\Delta\rho}{\bar{\rho}}$, $\Delta\gamma$ and $\Delta\sigma^{(V)}$.

A second, qualitative way to use the results derived in this chapter is to study lateral variations in the S-wave AVO gradients for the survey area. Assuming that the fracture-plane velocity β changes slowly (or is known), the AVO gradients of $R_{S\perp}^{strike}$, $R_{S\parallel}^{sym}$ and $R_{S\perp}^{sym}$ will reflect changes in γ. The $R_{S\perp}^{sym}$ AVO gradient will additionally sense changes in $(\epsilon^{(V)} - \delta^{(V)})$ and provide insight in the change of the filling of the cracks. Spatial mapping of the individual AVO gradients may therefore be a fast tool to identify "weak" spots of high fracture density. A more detailed discussion on the feasibility of shear-wave AVO can be found in Rüger (1996). For completeness, in Appendix D, I include a collection of all pure and converted-wave reflection coefficients in HTI symmetry planes.

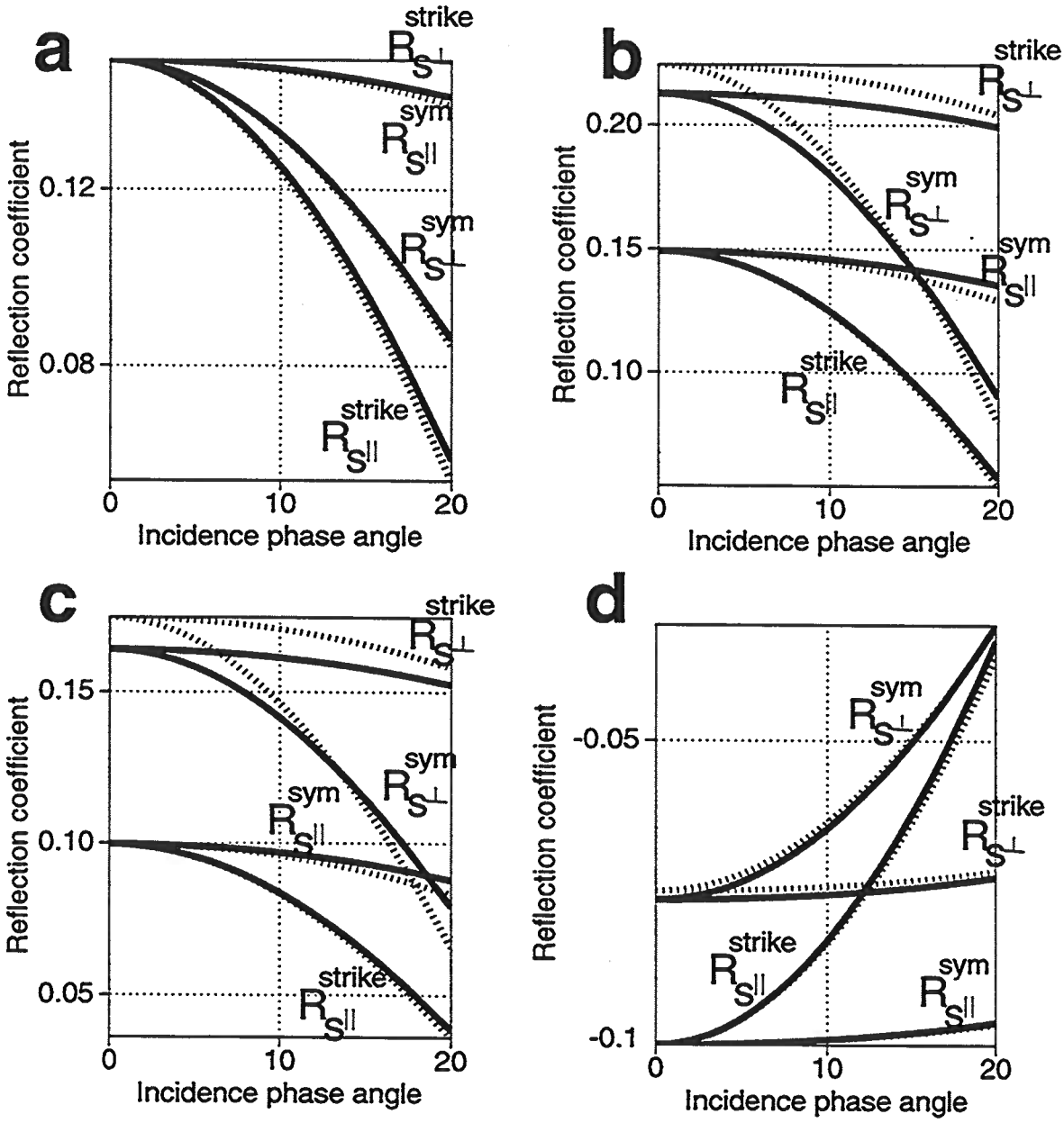

FIG. 6.3. $S^{\parallel}$- and $S^{\perp}$-wave reflection coefficients for the two vertical symmetry planes at isotropic/HTI interfaces. Shown are the exact solutions (solid lines) and approximations based on equations (6.6) and (6.7)(dashed). The model parameters are given in Table 6.1.

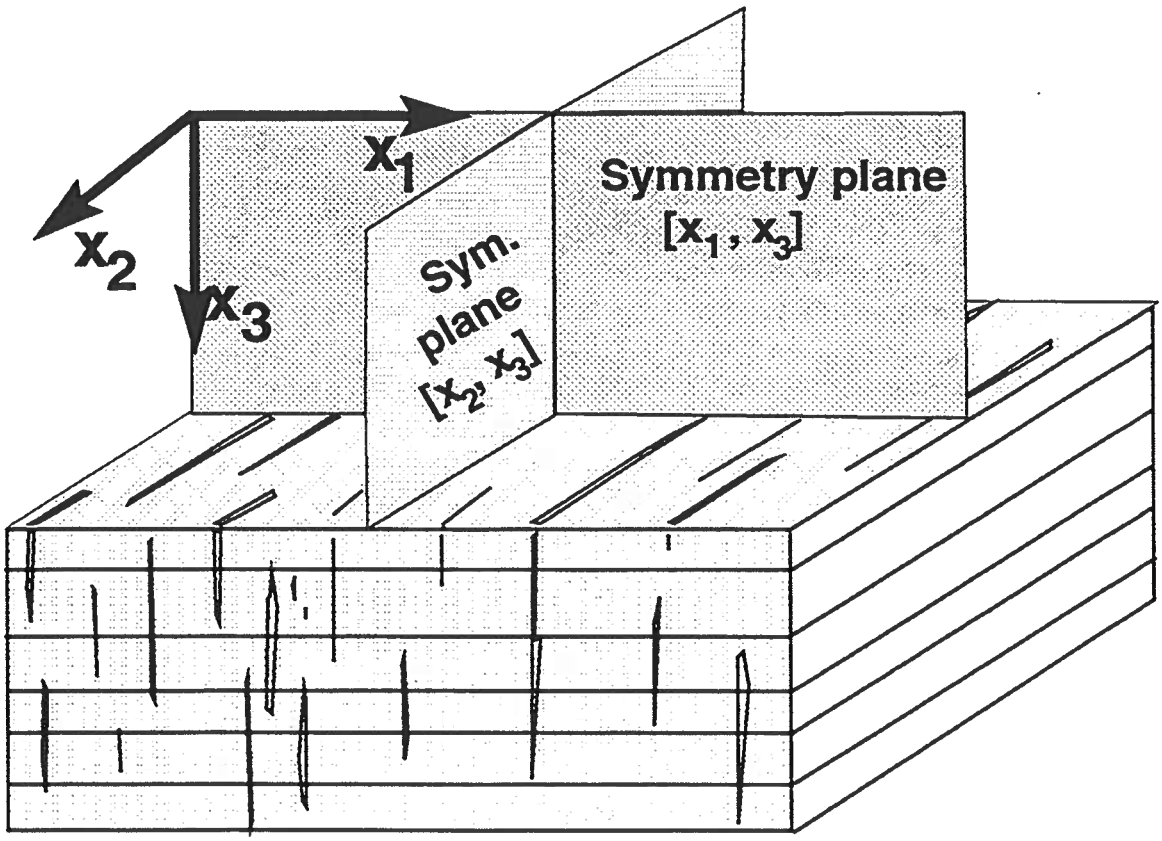

FIG. 7.1. Sketch of an orthorhombic model created by combining horizontal layering with a system of parallel vertical cracks. Two vertical symmetry planes are determined by the crack orientation.

Chapter 7

REFLECTION COEFFICIENTS IN THE SYMMETRY PLANES OF ORTHORHOMBIC MEDIA

Horizontal transverse isotropy is a useful model for studying the first-order influence of azimuthal anisotropy. More realistic models can be described by the orthorhombic symmetry system. Wave propagation in orthorhombic media is rather complex; analysis of wavefronts and slowness surfaces in orthorhombic media can, for example, be found in Musgrave (1970), Helbig (1994) and Schoenberg & Helbig (1995). Although the following investigation is valid for orthorhombic media of any origin, it is instructive to examine an orthorhombic model due to a combination of a VTI background medium with a system of aligned vertical cracks (Figure 7.1). This orthorhombic model (as in any other orthorhombic model with a horizontal symmetry plane) has two vertical symmetry planes (symmetry plane $[x_1, x_3]$ and symmetry plane $[x_2, x_3]$). In this chapter, I obtain approximations for reflection coefficients of P-waves incident in the two vertical symmetry planes of orthorhombic media to gain a better understanding of the magnitude of azimuthal change of the AVO gradients and relate it to the anisotropy in the subsurface.

7.1 Effective parameters for orthorhombic media

A rigorous mathematical analysis of the symmetry-plane reflection responses is possible by studying the corresponding Christoffel equations for orthorhombic media in the same way as was done n the HTI study in Chapter 4. Study of the symmetry-plane Christoffel equations in Appendix C helps to relate wave propagation in the $[x_1, x_3]$ and $[x_2, x_3]$ planes of orthorhombic models to wave propagation in VTI media. This analysis, given in more detail in Tsvankin (1996a), proves that symmetry-plane propagation in orthorhombic media can be completely described by known VTI equations. In other words, all conclusions about the limited equivalence of VTI and HTI media (Chapter 4) remain valid for symmetry-plane propagation in orthorhombic models. This leads to the introduction of new dimensionless anisotropy parameters defined similarly to the well-known Thomsen's (1986) coefficients ϵ, δ and γ (Tsvankin, 1996a):

- $\epsilon^{(2)}$ – the VTI parameter ϵ in the symmetry plane $[x_1, x_3]$ normal to the x_2-axis (close to the fractional difference between the P-wave velocities in the x_1- and x_3-directions):

$$\epsilon^{(2)} \equiv \frac{c_{11} - c_{33}}{2c_{33}}. \tag{7.1}$$

- $\delta^{(2)}$ – the VTI parameter δ in the $[x_1, x_3]$-plane (responsible for near-vertical P-wave velocity variations; also influences SV-wave velocity anisotropy):

$$\delta^{(2)} \equiv \frac{(c_{13}+c_{55})^2-(c_{33}-c_{55})^2}{2c_{33}\,(c_{33}-c_{55})}. \tag{7.2}$$

- $\gamma^{(2)}$ – the VTI parameter γ in the $[x_1, x_3]$-plane (close to the fractional difference between the SH-wave velocities in the x_1- and x_3-directions):

$$\gamma^{(2)} \equiv \frac{c_{66}-c_{44}}{2c_{44}}. \tag{7.3}$$

- $\epsilon^{(1)}$ – the VTI parameter ϵ in the $[x_2, x_3]$-plane:

$$\epsilon^{(1)} \equiv \frac{c_{22}-c_{33}}{2c_{33}}. \tag{7.4}$$

- $\delta^{(1)}$ – the VTI parameter δ in the $[x_2, x_3]$-plane:

$$\delta^{(1)} \equiv \frac{(c_{23}+c_{44})^2-(c_{33}-c_{44})^2}{2c_{33}\,(c_{33}-c_{44})}. \tag{7.5}$$

- $\gamma^{(1)}$ – the VTI parameter γ in the $[x_2, x_3]$-plane:

$$\gamma^{(1)} \equiv \frac{c_{66}-c_{55}}{2c_{55}}. \tag{7.6}$$

- $\delta^{(3)}$ – the VTI parameter δ in the $[x_1, x_2]$-plane (x_1 plays the role of the symmetry axis):

$$\delta^{(3)} \equiv \frac{(c_{12}+c_{66})^2-(c_{11}-c_{66})^2}{2c_{11}\,(c_{11}-c_{66})}. \tag{7.7}$$

These seven dimensionless parameters, together with the vertical velocities:

- α – the vertical velocity of the P-wave:

$$\alpha \equiv \sqrt{\frac{c_{33}}{\rho}}. \tag{7.8}$$

- β – the vertical velocity of the S-wave polarized in the x_2-direction:

$$\beta \equiv \sqrt{\frac{c_{44}}{\rho}}, \tag{7.9}$$

Orthorhombic	VTI	HTI
$\delta^{(2)} = \frac{(c_{13}+c_{55})^2-(c_{33}-c_{55})^2}{2c_{33}(c_{33}-c_{55})}$	δ	$\delta^{(V)}$
$\delta^{(1)} = \frac{(c_{23}+c_{44})^2-(c_{33}-c_{44})^2}{2c_{33}(c_{33}-c_{44})}$	δ	0
$\delta^{(3)} = \frac{(c_{12}+c_{66})^2-(c_{11}-c_{66})^2}{2c_{11}(c_{11}-c_{66})}$	0	$\delta^{(V)} - 2\epsilon^{(V)}$
$\epsilon^{(2)} = \frac{c_{11}-c_{33}}{2c_{33}}$	ϵ	$\epsilon^{(V)}$
$\epsilon^{(1)} = \frac{c_{22}-c_{33}}{2c_{33}}$	ϵ	0
$\gamma^{(2)} = \frac{c_{66}-c_{44}}{2c_{44}}$	γ	$-\gamma$
$\gamma^{(1)} = \frac{c_{66}-c_{55}}{2c_{55}}$	γ	0

Table 7.1. Seven anisotropy parameters (plus two vertical velocities) completely describe orthorhombic anisotropy. Their relationship to the generic (VTI) Thomsen coefficients and to HTI parameters $\delta^{(V)}$ and $\epsilon^{(V)}$ are shown in the second and third column. The expressions for $\delta^{(3)}$ and $\gamma^{(2)}$ are approximate, the other relations are valid for any strength of anisotropy.

can replace the nine independent stiffness components of the orthorhombic model. As summarized in Table 7.1, both vertical and horizontal transverse isotropy can be considered as degenerated special cases of orthorhombic media. An orthorhombic medium reduces to the VTI model if the properties in all vertical planes are identical, and the velocity of each mode in the $[x_1, x_2]$-plane is constant (although the velocities of the two S-waves generally differ from one another). Another special case is transverse isotropy with a horizontal axis of symmetry. If the symmetry axis is oriented along the x_1-direction, the parameters $\epsilon^{(2)}$, $\delta^{(2)}$ and $\gamma^{(2)}$ coincide with the coefficients $\epsilon^{(V)}$, $\delta^{(V)}$ and $\gamma^{(V)}$ introduced in Chapter 4.

7.2 *P*-wave reflections in the symmetry planes

Seismic signatures in the $[x_1, x_3]$-plane of media with orthorhombic symmetry can be evaluated by means of already known VTI equations. Published VTI phase-velocity equations in c_{ij}-notation, for example, exactly express phase velocity in symmetry planes of orthorhombic media (with appropriate substitutions in the $[x_2, x_3]$-plane; see details below). Additionally, reflection coefficients in the symmetry planes of orthorhombic media are the same as in VTI media if the upper and lower media have the same orientations of the symmetry planes. To compute exact symmetry-plane reflection coefficients in order to understand better their azimuthal variations, it is hence sufficient to use Graebner's (1992) algorithm introduced in Chapter 3. Also, the approximate VTI reflection coefficients can be used in the symmetry-planes: following the simple recipe of replacing δ and ϵ with $\delta^{(2)}$ and $\epsilon^{(2)}$ yields the approximate *P*-wave

reflection coefficient in the $[x_1, x_3]$-symmetry-plane of orthorhombic media:

$$\begin{aligned} R_P^{[x_1,x_3]}(i) &= \frac{1}{2}\frac{\Delta Z}{\bar{Z}} + \\ &\frac{1}{2}\left[\frac{\Delta\alpha}{\bar{\alpha}} - \left(\frac{2\bar{\beta}^{\perp}}{\bar{\alpha}}\right)^2 \frac{\Delta G^{\perp}}{\bar{G}^{\perp}} + \Delta\delta^{(2)}\right]\sin^2 i + \\ &\frac{1}{2}\left(\frac{\Delta\alpha}{\bar{\alpha}} + \Delta\epsilon^{(2)}\right)\sin^2 i \tan^2 i \,, \end{aligned} \tag{7.10}$$

with $\beta^{\perp} = \sqrt{c_{55}/\rho}$. At the expense of reduced numerical accuracy, equation (7.10) can also be written as a function of the second vertical shear-wave velocity $\beta = \sqrt{c_{44}/\rho}$ and the shear-wave splitting parameter $\gamma = \frac{c_{44}-c_{55}}{2c_{55}}$:

$$\begin{aligned} R_P^{[x_1,x_3]}(i) &= \frac{1}{2}\frac{\Delta Z}{\bar{Z}} + \\ &\frac{1}{2}\left[\frac{\Delta\alpha}{\bar{\alpha}} - \left(\frac{2\bar{\beta}}{\bar{\alpha}}\right)^2 \left(\frac{\Delta G}{\bar{G}} - 2\Delta\gamma\right) + \Delta\delta^{(2)}\right]\sin^2 i + \\ &\frac{1}{2}\left(\frac{\Delta\alpha}{\bar{\alpha}} + \Delta\epsilon^{(2)}\right)\sin^2 i \tan^2 i \,. \end{aligned} \tag{7.11}$$

Basically the same observations can be made by comparing the Christoffel equations in the $[x_2, x_3]$-plane of orthorhombic media with those for VTI media. Graebner's (1992) algorithm for VTI systems can also be used in this case, but one has to make the substitutions

$$c_{11} \rightarrow c_{22}, \quad c_{55} \rightarrow c_{44}, \quad c_{13} \rightarrow c_{23} \,.$$

Thus, the $[x_2, x_3]$-plane of orthorhombic media can be replaced by a second equivalent VTI medium with $\epsilon = \epsilon^{(1)}$ and $\delta = \delta^{(1)}$ [equations (7.4) and (7.4)]. Substituting $\delta^{(1)}$ and $\epsilon^{(1)}$ into equation (3.33) yields the approximate reflection coefficient for the $[x_2, x_3]$ symmetry plane:

$$\begin{aligned} R_P^{[x_2,x_3]}(i) &= \frac{1}{2}\frac{\Delta Z}{\bar{Z}} + \\ &\frac{1}{2}\left(\frac{\Delta\alpha}{\bar{\alpha}} - \left(\frac{2\bar{\beta}}{\bar{\alpha}}\right)^2 \frac{\Delta G}{\bar{G}} + \Delta\delta^{(1)}\right)\sin^2 i + \\ &\frac{1}{2}\left(\frac{\Delta\alpha}{\bar{\alpha}} + \Delta\epsilon^{(1)}\right)\sin^2 i \tan^2 i \,. \end{aligned} \tag{7.12}$$

The same approach can be used to derive the shear-wave reflection coefficients in the vertical symmetry planes of orthorhombic media; for completeness, the results

are presented in Appendix E. The results shown in this chapter are applicable to interfaces between isotropic, VTI, HTI and orthorhombic media, provided that their vertical symmetry planes are aligned.

7.3 Azimuthal variation of orthorhombic reflection coefficients

The discussion above shows that the approximate reflection coefficients in the two vertical symmetry planes of orthorhombic media are essentially identical to the reflection coefficients in the HTI symmetry-axis plane. This result makes it possible to use the difference in the P-wave reflection coefficients in the two vertical symmetry planes of orthorhombic media to invert for the shear-wave splitting parameter. To eliminate the "isotropic quantities" in equations (7.11) and (7.12), I follow the approach suggested for HTI media (Chapter 5) and find the difference between the two symmetry-plane coefficients:

$$\begin{aligned} R_P^{[x_1,x_3]} - R_P^{[x_2,x_3]} &= \left\{ \left(\frac{2\bar{\beta}}{\bar{\alpha}} \right)^2 \Delta\gamma + \right. \\ &\left. \frac{1}{2} \left(\Delta\delta^{(2)} - \Delta\delta^{(1)} \right) \right\} \sin^2 i + \\ &\frac{1}{2} \left\{ \Delta\epsilon^{(2)} - \Delta\epsilon^{(1)} \right\} \sin^2 i \tan^2 i \,. \end{aligned} \tag{7.13}$$

For an isotropic overburden ($\gamma_1 = \delta_1^{(1)} = \delta_1^{(2)} = 0$), the difference in the AVO gradient depends on just three anisotropic parameters - the shear-wave splitting parameter γ_2 and two new parameters $\delta_2^{(1)}$ and $\delta_2^{(2)}$ describing the anisotropy for near-vertical P-wave propagation in the symmetry planes. Tsvankin (1996a) shows that it is possible to obtain the parameters $\delta^{(1)}$ and $\delta^{(2)}$ from short-spread P-wave moveout velocity in the vertical symmetry planes, provided an estimate of the vertical velocity is available (for examples from vertical velocities measured in a VSP experiment). Thus, we can get γ by combining NMO and AVO analysis. Note that for orthorhombic models with a single crack system, γ gives an estimate of the crack density.

Chapter 8

P-WAVE AVO FOR FRACTURED RESERVOIRS

In this chapter, I address some important practical aspects of *P*-wave AVO analysis for fractured formations of HTI symmetry. First, I review the assumptions of Hudson's theory (Hudson, 1981) used to compute the parameters of the effective anisotropic continuum that replaces the cracked material[1]. Then, I show the AVO responses for unfractured and fractured layers with different content of cracks and finally address some (of the many) complications that arise in the extraction and interpretation of the reflection coefficients from seismic data. These problems are especially challenging if the overburden is anisotropic and the reflecting target-layer is thin. The chapter ends with some remarks concerning the acquisition and processing of seismic data in the presence of azimuthal anisotropy.

8.1 Effective parameters of fractured solids

Clearly, fractured layers of complicated fracture geometry and crack distribution cannot be mathematically described in every detail. However, under certain assumptions it is possible to derive average elastodynamic properties of a cracked solid. For example, it can be shown that if a medium contains aligned cracks which are small compared to the seismic wavelength, the waves propagate through it as if the material were homogeneous and anisotropic (Crampin, 1984b).

Hudson (1981), (1986) derived formulas to compute effective elastic properties of rocks containing systems of cracks. For mathematical convenience and because his equations describe effective properties of the cracked medium, Hudson assumes the following conditions:

- the cracks are (on average) oblate spheroids of small aspect ratio;
- the distribution of positions of cracks is random on the scale of a seismic wavelength;
- the cracks are sparsely distributed and disconnected, and their total volume is a small fraction of the volume of the rock;

[1]This however does not imply that the approximations developed in this thesis are limited to Hudson's fracture model; the coefficients $\delta^{(V)}, \epsilon^{(V)}$ and γ can be evaluated for any arbitrary HTI medium.

- the crack radius and the spacing between the cracks are much smaller than the seismic wavelength ($ka << 1$ where k is the wavenumber and a is the crack radius);

- the crack contents are softer than the matrix and

- the diffraction field due to any crack is approximately uniform over the face of any other crack.

For more details on the intrinsic assumptions of Hudson's theory, see Peacock and Hudson (1990).

To first order in the crack density, Hudson's formulas agree with other existing theories [for example, Nishizawa (1982)] and, despite their limiting assumptions, have been successfully applied by several authors to interpret seismic anisotropy (Crampin *et al.*, 1986; Sayers, 1988). The effective parameters used in this chapter are computed using Hudson's second-order equations, which are accurate to second order in crack density and allow for crack-crack interactions. Different conditions within the cracks can be taken into account: in this chapter, I compute the elastic constants due to dry (gas-filled) and fluid (water-filled) cracks.

8.2 Influence of fracturing on the AVO response

Figure 8.1 shows three models with a different target layer (the layer in the middle). The elastic parameters of the first target layer are given in the first column of Table 8.1; the parameters of the other two target layers are computed for the same host rock, but this time containing cracks with aspect ratio 0.001 and seven-percent crack density. The parameters of the second and third columns are computed for water-filled and dry cracks, respectively. The cracks are vertically aligned causing fractured layers of HTI symmetry. The same crack models have been used by Gajewski (1993) who also used Hudson's theory of fractured materials (Hudson, 1981) to compute the effective parameters.

Initially, I consider reflections from the top of the target with the overburden assumed to be isotropic. Subsequently, I will study the influence of an anisotropic overburden on the reflection amplitudes. Below, I analyze the influence of the layer-thickness on the amplitude of the reflected wavefield.

Before evaluating the reflection response for the three models, let us briefly investigate the difference between the model parameters and use equation (5.7) to predict the behavior of the three AVO responses. Both fractured and unfractured models have the same density and the same fast vertical shear-wave velocity. This is physically reasonable because, as confirmed by Hudson's equations, the shear wave polarized within the fracture plane should not be influenced by the fracturing. Also, the fractures are too thin to influence the bulk density of the host rock; the vertical P-wave velocities α are very similar for the medium with fluid-filled cracks and for the unfractured

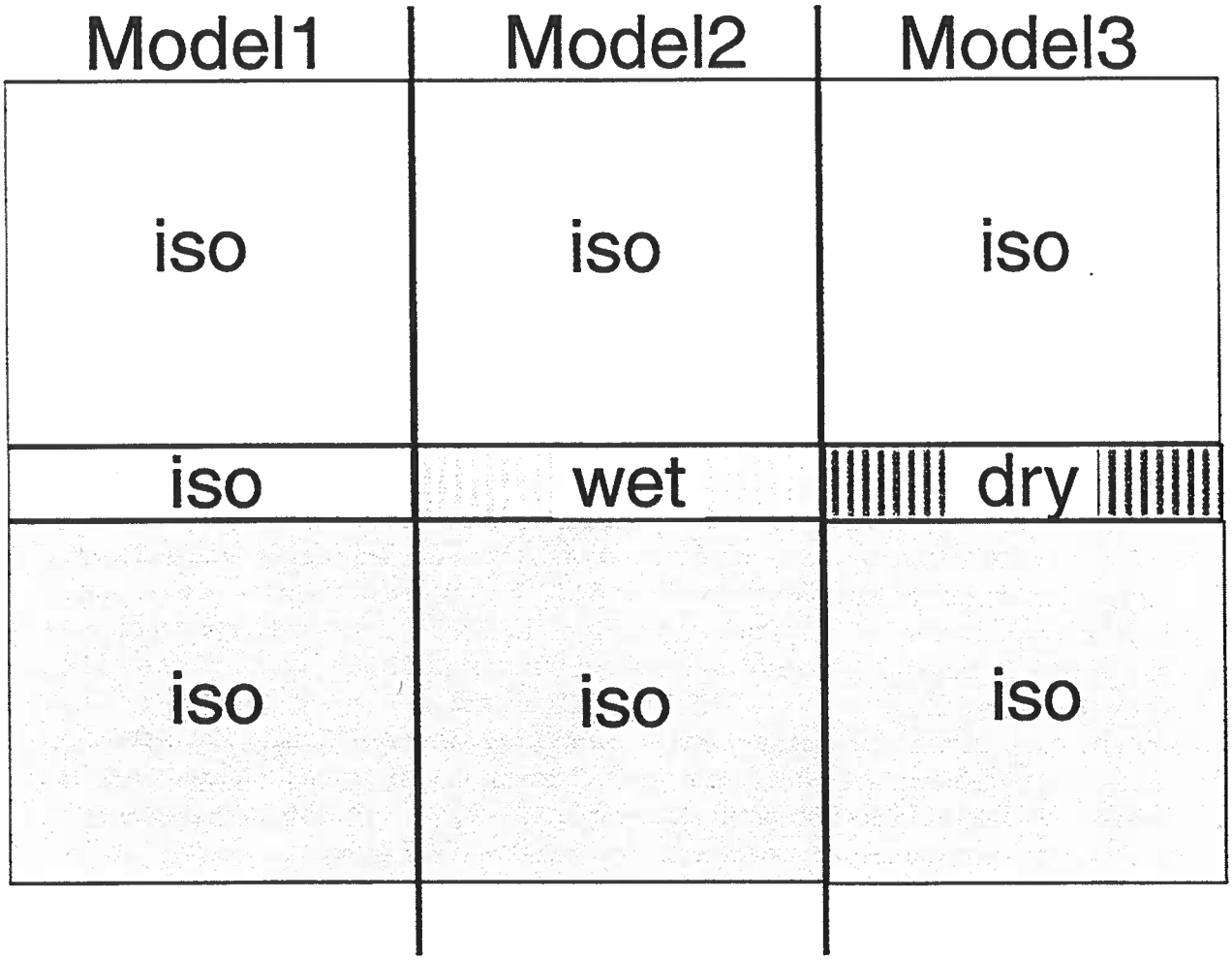

FIG. 8.1. Three models used to study the differences in the AVO response caused by dry and fluid-filled cracks. Table 8.1 lists the model parameters.

	isotropic	wet cracks	dry cracks
α	4.500	4.498	4.388
β	2.530	2.530	2.530
ρ	2.800	2.800	2.800
γ	0.000	0.085	0.085
$\epsilon^{(V)}$	0.000	-0.003	-0.150
$\delta^{(V)}$	0.000	-0.088	-0.155

Table 8.1. Parameters of the reflecting layers used to investigate the azimuthally varying AVO reponse. Model 1 (isotropic), Model 2 (wet cracks) and Model 4 (dry cracks) have the same host rock, but differ in the density and filling of the cracks.

	isotropic	wet cracks	dry cracks
$\frac{\Delta\alpha}{\bar{\alpha}}$	0.203	0.203	0.180
$\frac{\Delta Z}{\bar{Z}}$	0.350	0.350	0.328
$\frac{\Delta G}{\bar{G}}$	0.601	0.601	0.601

Table 8.2. Percentage changes in elastic parameters for reflections from the top of the target layer. The parameters of the isotropic overburden are $V_P = 3.67$ km/s, $V_S = 2.0$ km/s, $\rho = 2.41$ g/cm^3.

rock and is slightly less (about 2.5 %) for the medium with dry cracks. The anisotropy parameters, however, are substantially influenced by the presence and content of the cracks. For wet cracks, the parameter $\epsilon^{(V)}$ is negligibly small, and the shear-wave-splitting parameter γ and coefficient $\delta^{(V)}$ have almost the same magnitude but opposite sign. In contrast, if the cracks are dry, the absolute values of both $\epsilon^{(V)}$ and $\delta^{(V)}$ are approximately twice as large as the shear-wave splitting parameter γ.

The differences in the anisotropy parameters cause different azimuthal changes in the reflection response for each of the models. Overall, considering the percentage changes in the elastic parameters (see Table 8.2) for a *P*-wave incident in an isotropic overburden, equation (5.7) predicts that the initial slope of the reflection coefficient for Model 1 is identical to the isotropy-plane coefficient of Model 2, while it is slightly less negative as compared to Model 3. Additionally, for wet cracks, $|\gamma|$ and $|\delta^{(V)}|$ are similar, and equation (5.7) suggests that there exists a substantial azimuthal difference in the AVO gradients, with a more negative isotropy-plane gradient [recall that the difference in the gradients is approximated by $(\delta^{(V)} + 2\gamma)$]. In contrast, the parameters of the layer containing dry cracks suggest that the AVO gradient will not change significantly for different azimuths. In this case, the reflection coefficients computed at different azimuths start to diverge at large angles of incidence.

Figures 8.2-8.4 show the exact and approximate reflection coefficients for the three models from Table 8.1. The parameters of the isotropic overburden are identical and are given in the caption of Table 8.2. Likewise, for comparison, the vertical scale for the three plots is unchanged. Approximation (5.7) is sufficiently close to the exact reflection coefficients for all three models; specifically, it predicts the different azimuthal changes in the small- and large-angle reflection response for the dry and water-filled cracks.

In addition to confirming the physical insight provided by equation (5.7), this modeling study shows that the *P*-wave AVO response from a fractured reservoir varies significantly as a function of the content of the crack. Therefore, *P*-wave AVO has the potential of discriminating between gas- and fluid-filled crack systems. A second important message is that the azimuthal difference in AVO gradients cannot be related directly to the crack density and that knowledge of the anisotropy parameter $\delta^{(V)}$ is crucial to any azimuthal AVO analysis. Also, if the AVO response at different azimuths is diverging substantially at large angles of incidence, it is a strong indication that $\epsilon^{(V)}$

has a significant value. In this case, the less negative AVO gradient corresponds to the isotropy-plane reflection because $\Delta\epsilon^{(V)}$ is negative for a reflection from the boundary between an isotropic layer and a fractured reservoir of HTI symmetry.

Finally, if γ is available from S-wave data, this study suggests combining the shear-wave-splitting and azimuthal-AVO analysis to obtain $\delta^{(V)}$ for study of the contents of the cracks. Alternatively, as mentioned above, P-wave NMO and AVO analysis have to be combined for a meaningful interpretation of the crack parameters.

8.3 Propagation phenomena in the anisotropic overburden

The discussion above is related to the interpretation and inversion of the reflection coefficients. In practice, we record the amplitude-versus-offset signature at the surface rather than the reflection coefficients at the target horizon. Corrections for the angular amplitude variation caused by the wave phenomena above the reflector is an essential part of the AVO analysis. To obtain the reflection coefficient at the target horizon, it is necessary to correct for the angular amplitude variation associated with the wave propagation between the reflector and the surface. The presence of anisotropy above the reflector leads to the so-called wavefront focusing phenomenon, or distortions of the amplitude distribution along the wavefronts of the incident and reflected waves (Tsvankin, 1995a). This situation may be quite typical for fractured reservoirs because the cracks are seldom confined to the reservoir layer (Mueller, 1991). Let us consider the wavefield from a point force in the symmetry-axis plane (containing the symmetry axis) of a two-layer HTI model with the same axis orientation in both layers. The angular amplitude dependence of the incident P–wave can be found in the weak-anisotropy approximation by adapting the result of Tsvankin (1995a):

$$U_P(R,\theta) = \frac{F_u}{4\pi\rho^{(1)}[V_{P0}^{(1)}]^2 R}\,(1-\delta_1-2(\epsilon_1-\delta_1)\sin^2 2\theta-\delta_1\sin^2\theta)\,, \qquad (8.1)$$

where U is the magnitude of the displacement, $\rho^{(1)}$ and $V_{P0}^{(1)}$ are the density and the P–wave symmetry-axis direction velocity (respectively) in the incidence medium, and R is the source-receiver distance. The source term F_u is the projection of the force on the displacement (polarization) vector. Note that, due to the 3-D nature of the wavefront focusing phenomena, the radiation pattern in the symmetry-axis plane of HTI media *cannot* be described by using the analogy with vertical transverse isotropy.

The comparison of the leading angular terms in equations (8.1) and (5.7) shows that the wavefront focusing and the anisotropic term in the reflection coefficient have a comparable influence on the angular amplitude variation. Since the difference $\epsilon_1-\delta_1$ is usually positive for HTI media due to parallel cracks (Thomsen, 1995), propagation phenomena above the reflector causes the P-wave amplitude in the symmetry-axis plane to decrease away from vertical (this can be observed, for example, in Figures 4.4b and 4.4c in the concentration of rays near vertical).

The influence of propagation phenomena cannot be ignored even if the medium

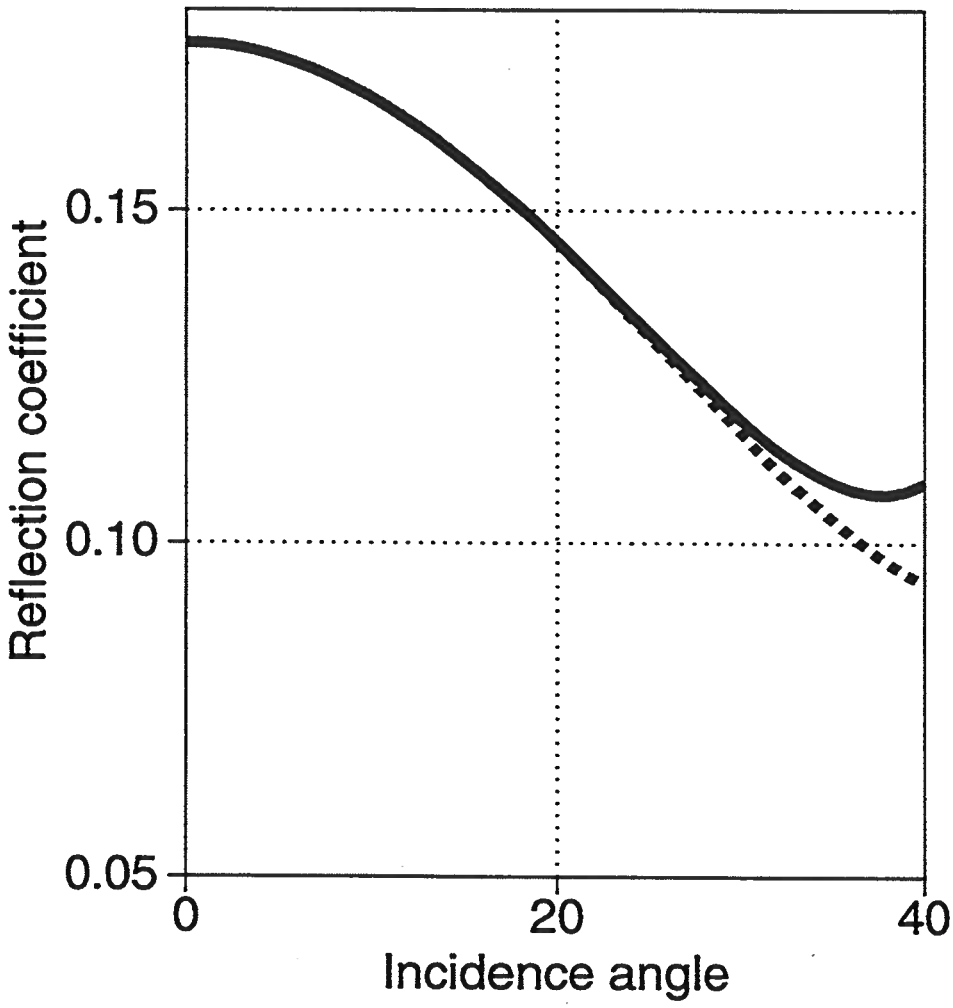

FIG. 8.2. The exact reflection coefficient (solid line) and the approximation (dashed) for an isotropic layer overlying the unfractured target layer. Model parameters are given in Tables 8.1 and 8.2 (the left column)

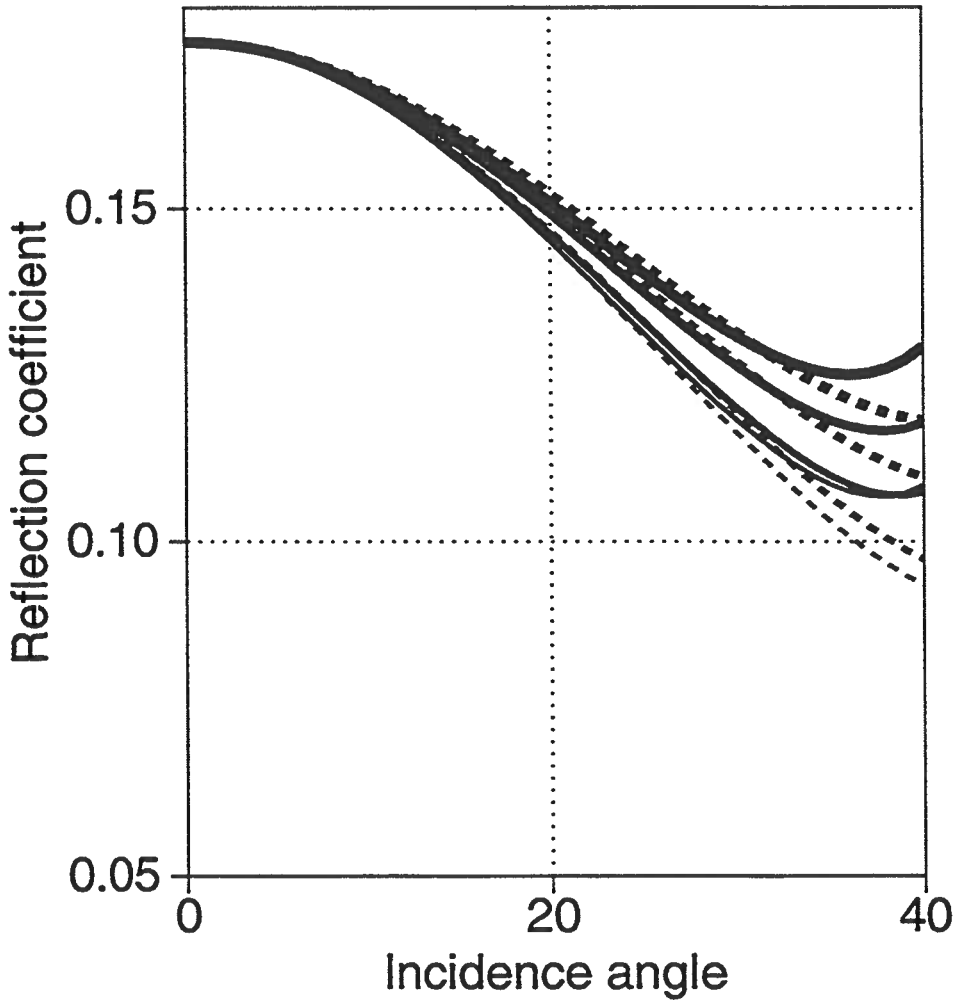

FIG. 8.3. Same as Figure 8.2, but the reflecting layer contains fluid-filled cracks (the central columns in Tables 8.1 and 8.2). The reflection coefficients are shown for azimuths of $0°, 30°, 60°$ and $90°$ measured from the symmetry-axis, with decreasing line thickness.

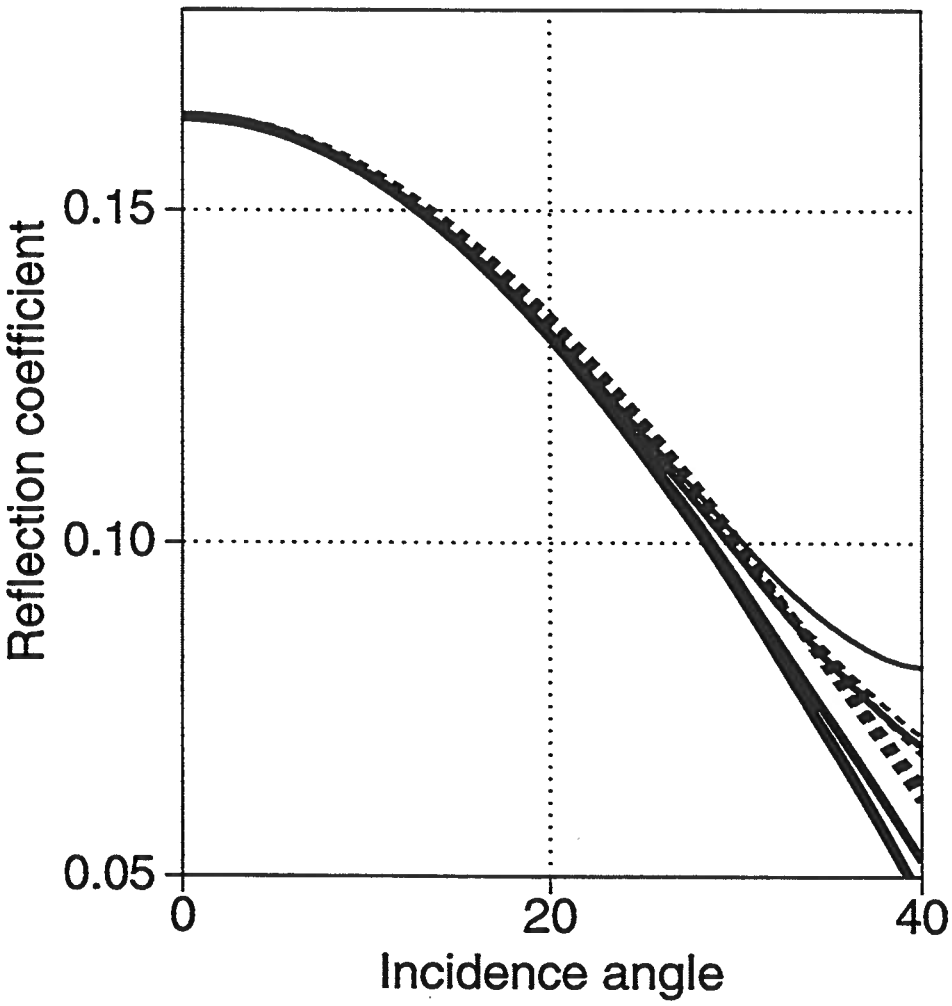

FIG. 8.4. Same as Figure 8.2 and 8.3, but the reflecting layer has dry cracks (the central columns in Tables 8.1 and 8.2).

above the reflector has a vertical axis of symmetry (we assume an HTI reflecting medium). Although the angular amplitude distortion will be exactly the same in the symmetry and isotropy plane, it will add a multiplier to equation (5.13) and cause errors in the estimation of the crack density. Therefore, correction for the influence of the anisotropy in the overburden should become an essential element of anisotropic AVO processing.

8.4 Amplitude versus offset or versus phase angle?

Serious challenges in the AVO interpretation exist even if the parameters of the azimuthally anisotropic overburden are known. For example, in the case of an azimuthally anisotropic overburden, the relation between offset and phase angle is non-trivial, and displaying the extracted reflection coefficient as a function of the source-receiver offset rather than as a function of the incident phase angle can lead to a misleading interpretation of the azimuthal AVO changes. To illustrate this point, let us assume that the target layer is located at a depth of 1 km and that the cracks are gas-filled (the parameters of the layer are shown in the third column of Table 8.1). The upper medium is composed of the same host rock as in the above examples, but is now fractured with a crack density of 5 percent. To simplify the discussion further, we assume that the fracture orientation is identical in both layers and only the reflection coefficients in the two vertical symmetry planes are considered.

Figures 8.5a and 8.5b show the reflection coefficients as a function of the incidence phase angle for dry and water-filled cracks in the overburden, respectively, together with the isotropy-plane approximation [equation (4.2)] and the symmetry-axis-plane approximation [equation (4.11)]. For the overburden with dry cracks, the isotropy-plane AVO gradient is more negative than is the symmetry-plane AVO gradient, but at larger angles of incidence, this trend changes and the isotropy-plane coefficient is increasingly larger than the symmetry-axis-plane coefficient (a clear indication that $\epsilon_2^{(V)} - \epsilon_1^{(V)} < 0$). On the other hand, no AVO-gradient change is visible in Figure 8.5b, and the divergent trend of the reflection-coefficient curves is observable only for large angles of incidence. As in the above study, this example demonstrates that it is impossible to directly relate the difference in azimuthal AVO variation to the crack density of the model: here, the identical reflecting layer and overburden with the same crack density produce different AVO responses for dry and wet cracks above the reflector.

Figure 8.6a and 8.6b show the same reflection coefficients as a function of offset rather than the incidence angle [these results have been generated by a dynamic ray-tracing program written by Grechka (1989)]. The difference from the results in Figure 8.5 is striking: in the case of the dry-fractured overburden, the relation between the AVO gradients is reversed (the isotropy-plane AVO slope is less negative than the symmetry-axis-plane slope), while the AVO gradients for the fluid-filled fractured overburden are obviously split, i.e, artificial reflection-coefficient changes are introduced.

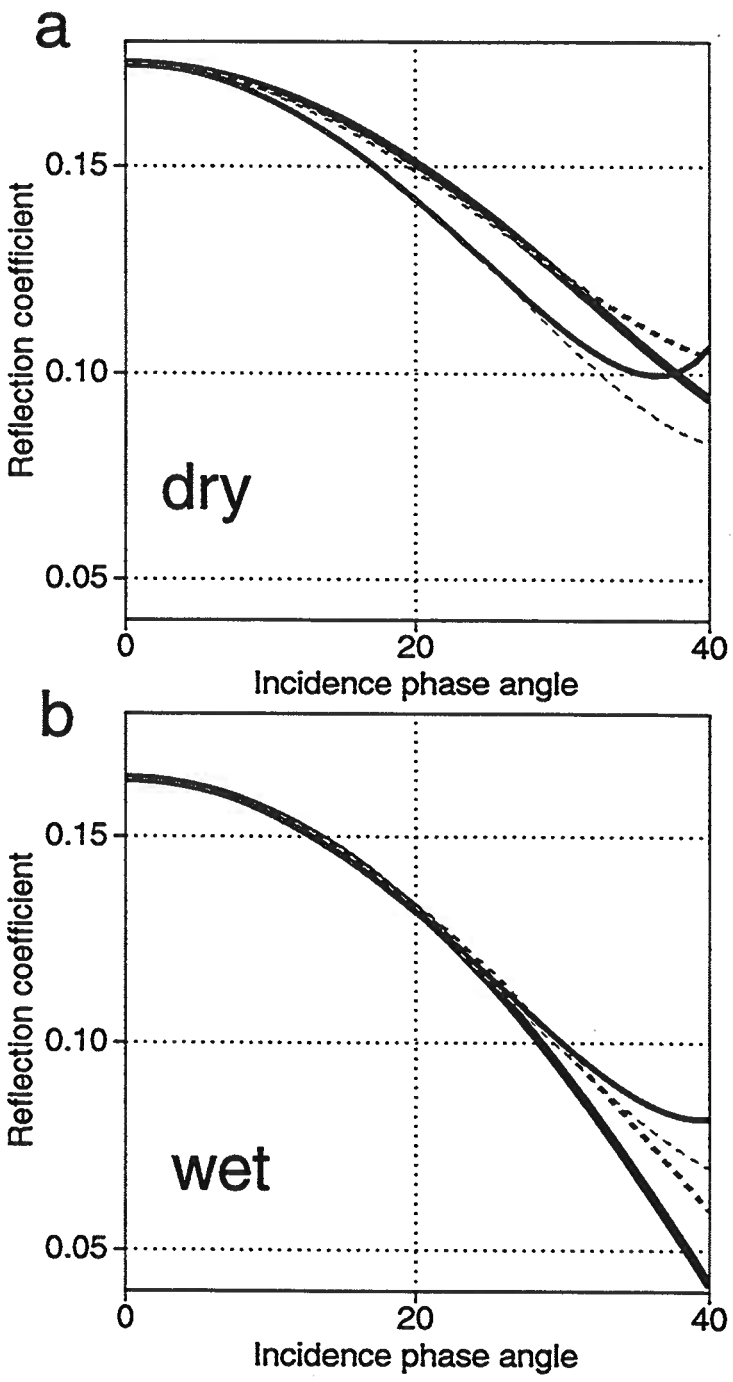

FIG. 8.5. Exact reflection coefficients (solid) and approximations (dashed) computed for the symmetry-axis plane (thick) and the isotropy plane (thin). The target (reflecting) layer contains dry cracks with a crack density of $\eta = 0.07$; the upper layer is fractured with $\eta = 0.05$, and the cracks are dry (a) and water-filled (b).

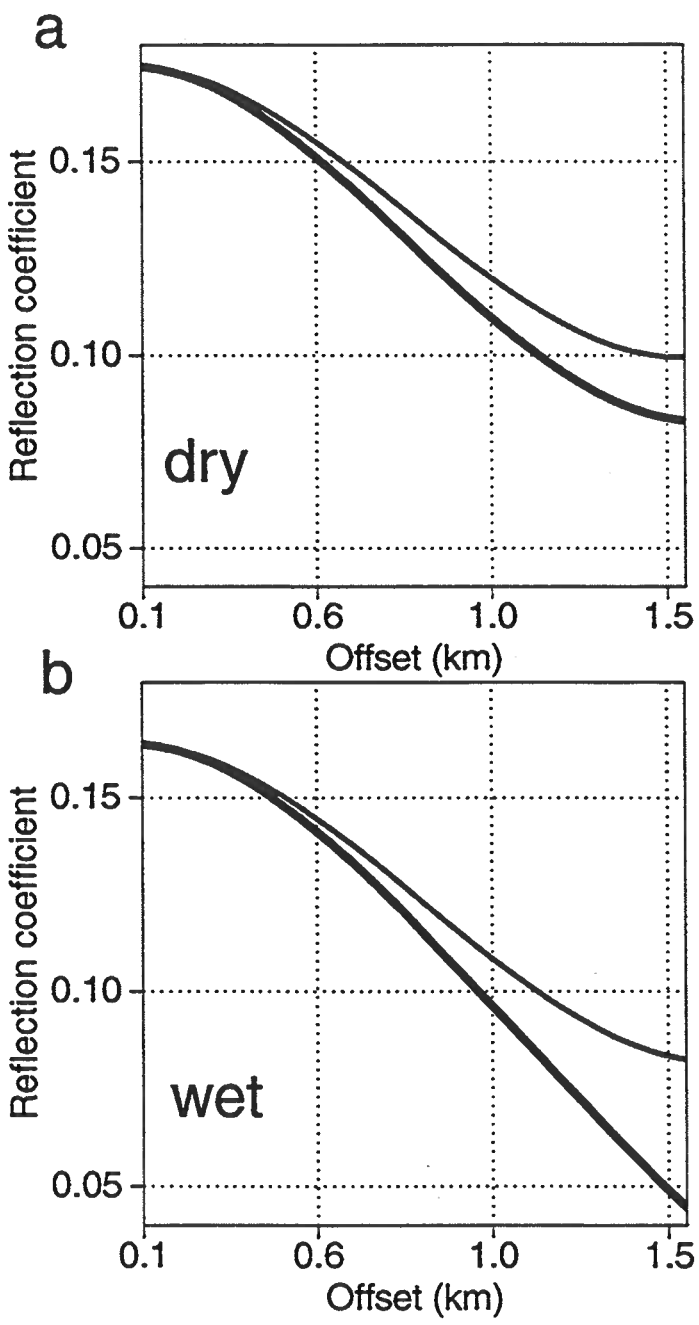

FIG. 8.6. Same as Figure 8.5, but the exact reflection coefficients are shown as a function of the source-receiver offset.

The explanation for the difference between the reflection coefficient curves is given in Figure 8.7a and 8.7b, which show the relations between the offsets and the incidence phase angles for the models from Figures 8.5 and 8.6. In azimuthally anisotropic media, the relation between group- and phase angles varies with azimuth. While both angles coincide for waves propagating in the isotropy plane, they can differ significantly for waves traveling in the symmetry-axis plane due to the presence of polar anisotropy. In other words, while rays connecting sources and receivers at any fixed offset form the same angle with vertical at the reflector, the associated phase angles are azimuthally varying. To correctly interpret the AVO signatures in anisotropic media, it is essential to represent them as a function of phase angle.

8.5 Thickness of the target layer

As shown above, complications caused by wave propagation in the anisotropic overburden can severely hamper both the extraction of the reflection coefficient and the AVO interpretation. Serious problems of a different nature also arise if the fractured layer is thin, i.e., if its thickness is comparable to or smaller than the seismic wavelength.

Consider waves reflected from a fractured layer 0.1 km thick at a depth of 1 km. The fractured layer has the parameters shown in the third column of Table 8.1, i.e., it has dry cracks with a crack density of seven percent. Both the upper and lower medium are isotropic (see Figure 8.1). As in isotropic media, thin layering causes interference between the top and bottom reflections. This can be seen in the seismic section (Figure 8.8) showing symmetry-axis-plane vertical component seismograms generated by a reflectivity algorithm (Corrigan, 1990). As observed at large offsets and 0.7–0.8 s traveltime, the much stronger bottom reflection starts to interfere with the diminishing-amplitude reflection from the top of the target layer.

Interference tends to increase with offset because the lower reflecting layer often has a higher velocity. While the interference problem also arises in isotropic media, it can be especially harmful for azimuthal AVO studies because azimuthal differences in the AVO signature are often observed at large angles of incidence.

One of the important conclusions of this modeling study is that azimuthal AVO and NMO analysis need to be combined for the interpretation of anisotropy parameters. The extraction of azimuthal variations of reflection traveltimes can, however, be very difficult in the case of a thin target layer. The reflection traveltimes from the top and bottom of the fractured layer are shown in Figure 8.9, for waves traveling in 0°, 30°, 60° and 90° azimuthal direction. Because the overburden is isotropic, no azimuthal change can be observed for the reflection traveltimes from the top of the layer. The azimuthal anisotropy in the fractured layer influences the bottom reflection, but the azimuthal time difference is not significant due to the small thickness of the layer. The difference in the moveouts for the lower reflections as seen in Figure 8.9 hardly allows any reliable extraction of anisotropy parameter $\delta^{(V)}$, which is necessary to infer information on crack density from the AVO measurements. The azimuthal

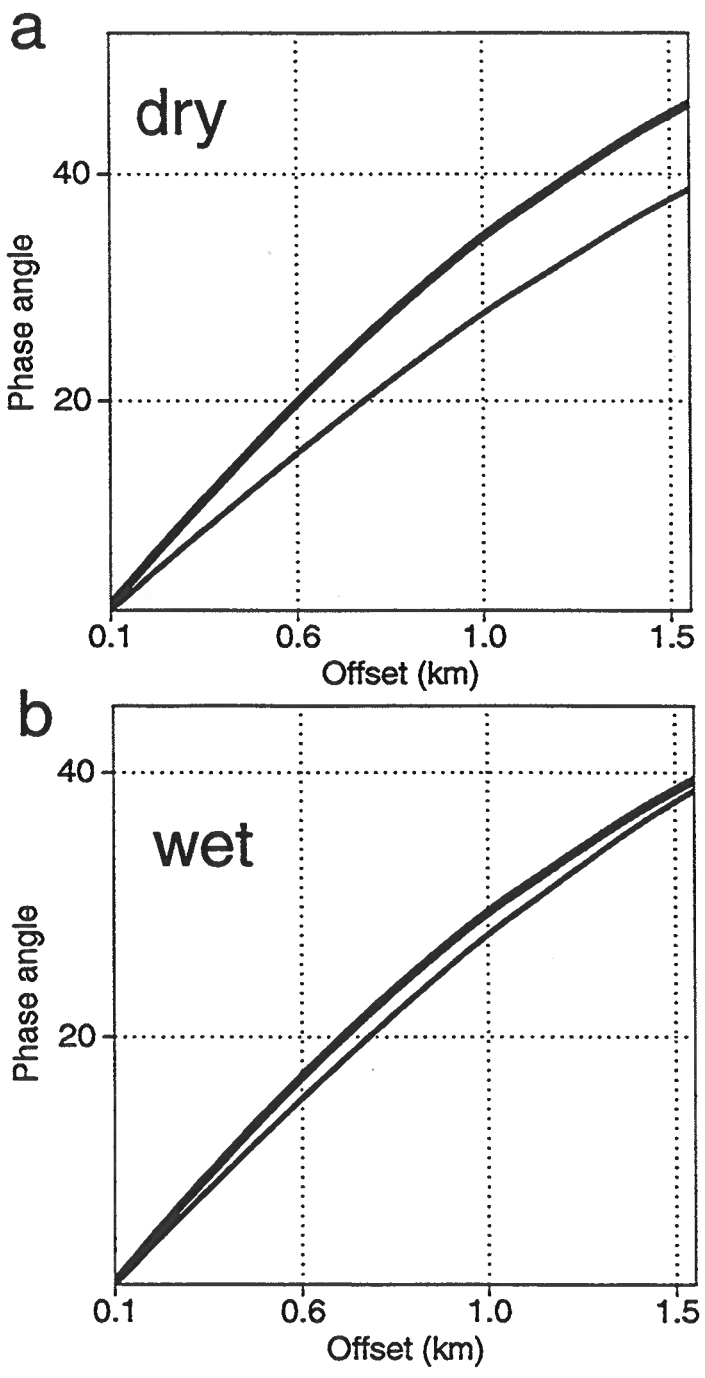

FIG. 8.7. Relation between the phase angles at the reflector and the source-receiver offset for the same models as from Figure 8.5.

reflection-time difference is even smaller for the fluid-filled cracks in the target layer, making any anisotropy-parameter extraction from surface-seismic traveltime data impossible. Additionally, without detailed knowledge of the anisotropy parameters in the layer, it is impossible to interpret the reflection response from the bottom of the target without risking the introduction of artificial AVO gradient changes similar to the case discussed in the previous chapter.

8.6 Data acquisition and processing

If it is known that the subsurface has HTI symmetry and the direction of the symmetry axis has been determined (for example, from *S*-wave data), two independent measurements of the reflection coefficients are sufficient to determine the magnitude of the azimuthal AVO variations. If the symmetry-axis direction is unknown, a minimum of three azimuths needs to be sampled. In practice, there exists a tradeoff between the number of sampled azimuths and the fold within each azimuthal bin (representing traces with similar source-receiver azimuths). A second concern is the offset distribution within each azimuthal bin. The classical acquisition design both for land and marine surveys leads to a uniform, dense distribution of offsets for azimuths aligned with the receiver lines, while the perpendicular direction is sampled much more coarsely. This severely hampers a reliable comparison of AVO results obtained in the two orthogonally oriented azimuthal bins. One way to overcome this problem in the marine environment would be the repeated overshooting of the survey area in different azimuthal directions. Although more expensive, it would significantly improve the data analysis and help to reveal azimuthally changing seismic signatures in a reliable fashion. Alternatives are newly developed survey designs such as the vertical cable and the ocean-bottom cables. On land, the geophones should be planted in areal patterns (instead of the conventionally used swath geometry) to ensure that the offset distribution is uniform in different azimuthal directions.

Another important prerequisite for any useful AVO-with-azimuth investigation is a proper processing sequence that preserves azimuthally varying seismic amplitudes. This requires a careful examination of each processing step (and algorithm) applied to the data to assess implications for the ability to preserve and properly treat azimuthal anisotropy. Conventional processing algorithms such as deconvolution, gaining, trace balancing etc. need to be modified to treat every azimuthal direction independently to not destroy the azimuthal signature. The situation is even more complex for imaging algorithms. For a 1-D Earth, an azimuthal bin with traces of source-receiver azimuth perpendicular to the symmetry-axis of the medium can be processed using isotropic algorithms. These algorithms, however, will introduce amplitude distortions if they are applied in structurally complex areas. Conventional algorithms such as (isotropic) DMO and migration designed to correct for the presence of dip in the overburden are not reliable for azimuths away from the isotropy-plane direction. Similarly, azimuthal bins aligned with the symmetry-axis can be processed with existing VTI algorithms. On the other hand, none of the VTI algorithms developed so far is

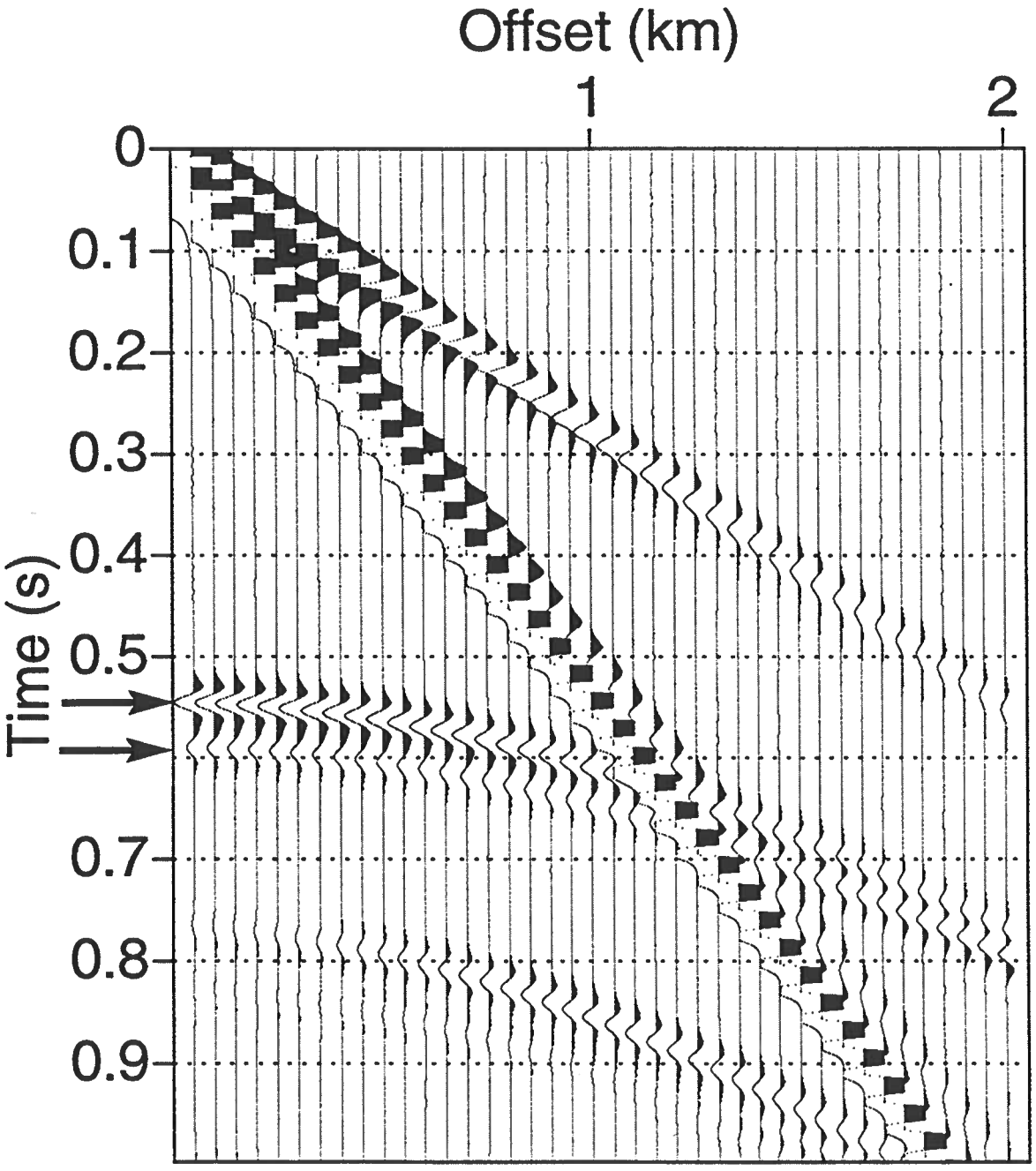

FIG. 8.8. Vertical-component seismograms for receivers situated in the symmetry-axis plane of the fractured target. The traces have been generated with the reflectivity method and contain the full wavefield, including groundroll, direct and converted waves. The reflections from the top and bottom of the fractured layer correspond to the troughs indicated by the arrows.

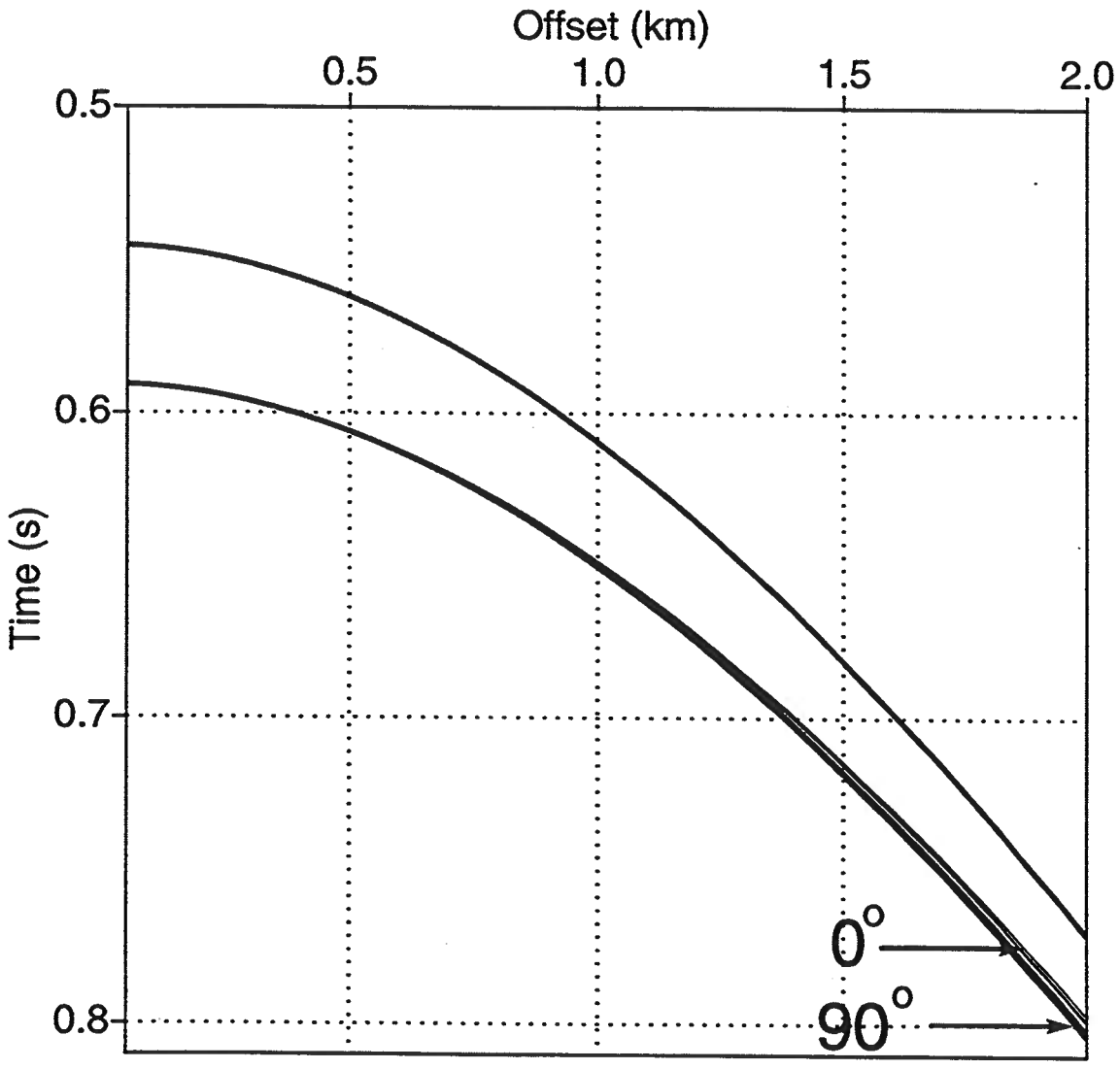

FIG. 8.9. Reflection traveltimes from the top and bottom of the fractured layer for waves traveling in 0°, 30°, 60° and 90° azimuthal direction. The fractured layer causes azimuthal changes in the traveltimes of the bottom reflection, but they are hardly visible because of the small layer thickness.

amplitude-preserving. For other azimuthal directions, no proper processing tools are available.

In conclusion, azimuthal AVO analysis requires carefully-designed acquisition geometries and a careful selection of the applied processing algorithms. Considering these difficulties, any azimuthal AVO analysis, especially in areas of complex geology has to be carried out with extreme care and needs to be combined with a detailed modeling study. Quantitative analysis is feasible only if the medium properties above the reflector are known in sufficient detail, especially if the overburden is anisotropic.

Chapter 9

CONCLUSIONS AND FUTURE WORK

The results of this research improve our understanding of the behavior of reflection coefficients in the presence of anisotropy. The linearized approximations derived here are helpful in obtaining simple representations of otherwise incomprehensibly complex reflection coefficients in anisotropic media. The main assumptions in this reflection-coefficient study — small jumps in the elastic parameters across the reflecting interface, pre-critical incidence and weak anisotropy — are geologically and geophysically reasonable and have proved useful in many exploration contexts.

The derived "Shuey-type" approximate reflection coefficients in VTI media provide a concise description of the AVO-gradient terms and the higher-angle terms as a function of Thomsen's (1986) parameters. For small incidence angles, the approximate P-wave reflection coefficient presented here is identical to previously published equations, but it is more accurate for larger incidence angles ($> 20 - 25^o$).

The refined approximation for reflection coefficients in VTI media can be used to find approximate reflection coefficients in transversely isotropic models with a horizontal axis of symmetry (HTI). The derivation is based on a limited analogy between VTI and HTI media that can also be used to determine kinematic properties and polarizations in HTI media. The equivalence between wave propagation in VTI media and the vertical plane containing the symmetry axis (the so-called symmetry-axis plane) of HTI media allows one to use known VTI equations (exact or approximate) in the symmetry-axis plane of HTI media. For example, existing numerical algorithms for reflection coefficients in VTI media, such as the one proposed by Graebner (1982), can also be used to efficiently compute the exact reflection coefficient in the symmetry-axis plane of HTI models. One of the most important applications of the VTI/HTI analogy is the introduction of new "Thomsen-style" anisotropy parameters for HTI media. Tsvankin (1995), for example, shows that the parameter $\delta^{(V)}$, entering the AVO gradient term of the P-wave reflection coefficient in the HTI symmetry-axis plane, also describes the azimuthal variation of P-wave normal-moveout velocity in HTI media.

The approximate reflection coefficients derived in this paper relate the AVO response to the anisotropy parameters and provide physical insight into the reflection amplitudes of pure and converted waves at boundaries between HTI media with the same orientation of the vertical symmetry planes. The azimuthal change in the P-wave AVO gradient is described by the squared cosine of azimuth. This azimuthal variation can be inverted for the symmetry-plane directions and a combination of the shear-wave splitting parameter γ and the anisotropy coefficient $\delta^{(V)}$. Coefficients γ and $\delta^{(V)}$ cause the same functional form of the azimuthal variation in the AVO gradient and cannot be

extracted individually. It is possible, however, to use P-wave moveout data to recover the parameter $\delta^{(V)}$; in other special cases such as thin fluid-filled cracks, coefficients γ and $\delta^{(V)}$ are directly related to each other.

The two symmetry-plane directions can even be extracted in situations where the azimuthal change in the AVO-gradient does not exist or is too small to be observed. In this case (which I found typical for fractured models with dry cracks), the azimuthal variation may become substantial at large incidence angles, where it is primarily dependent on the anisotropy coefficient $\epsilon^{(V)}$ ($\epsilon^{(V)} \approx -\epsilon$, where ϵ is the generic Thomsen parameter). The azimuthal change in the large-angle reflection coefficient provides enough information to detect the natural coordinate system of the subsurface (i.e., the crack orientation).

Certainly, realistic models of fractured reservoirs may deviate from relatively simple HTI media, and it is important to study whether the reflection response in media of lower symmetry (e.g., orthorhombic) differs significantly from that in the HTI case. Although wave propagation in orthorhombic media is significantly more complex, the approximate reflection coefficients in the symmetry planes have essentially the same form as in HTI models. The difference between the P-wave AVO gradients in the vertical symmetry planes is a function of the shear-wave splitting parameter γ and two new parameters similar to $\delta^{(V)}$, describing near-vertical P-wave velocity variations. Analogous observations have been obtained for all pure and converted-mode reflection coefficients and are useful for investigating the potential of multi-component AVO analysis for realistic azimuthally anisotropic formations.

The approximations derived in this thesis create simple dependencies that interpreters can use to quickly evaluate the magnitude of anisotropy in a particular play. They describe the dependence of the AVO response on the individual anisotropy parameters and show how independent data (such as those obtained by shear-wave-splitting or moveout analysis) can be integrated in the inversion procedure. However, although the approximate reflection coefficients help to detect pronounced anomalies, they are not suitable for quantitative analysis at interfaces with a large contrast in the elastic parameters and strong anisotropy. The HTI approximations presented here will also be inaccurate if the natural coordinate systems of the incidence and reflecting layer differ in orientation, i.e., if the axis of symmetry changes across the boundary.

Numerical examples show that the derived approximate reflection coefficients are close to the exact reflection response for situations where the underlying assumptions on the reflecting boundary are satisfied. However, rather than achieving a high numerical accuracy with the new approximations, it is more important to establish a physical foundation for (exact) numerical inversion algorithms. Evidently, there is little hope to carry out "blind" inversion of the AVO response for subsurface parameters. The linearized reflection coefficients given here indicate which parameters or parameter combinations can be inverted for at small or large angles of incidence. These approximations can also serve as a guide for a more efficient and more accurate inversion, e.g., in the iterative adjustment of the unknown parameters in the forward modeling process.

The practical implementation of the newly-proposed AVO inversion faces challenges similar to or even greater than those in conventional AVO analysis. Prerequisite for any useful AVO-with-azimuth investigation is a processing sequence that preserves azimuthally varying amplitude signatures. Moreover, the influence of lateral inhomogeneities should be corrected for. Wave propagation in an anisotropic overburden has a significant impact on the amplitude variation with offset and azimuth and needs to be included in any AVO processing sequence. Other difficulties include thin layering, curved reflectors or dipping symmetry-axes. These issues are outside of the scope of this investigation and should be addressed in future research.

Amplitude signatures of reflected wavefields in anisotropic media are very difficult to extract from field data. Clearly, much more work on this topic is required. Nevertheless, the formalism developed here has already proved useful in the interpretation of a data set acquired by the Reservoir Characterization Project in the Joffre field (Alberta, Canada) (Rolla, 1995), although the acquisition design was not well-suited for azimuthal analysis of P-wave signatures.

The results presented in this thesis have also influenced several other projects dealing with multi-component AVO analysis for boundaries between azimuthally anisotropic media (Li & Kühnel, 1996; Haugen, 1996; Teng & Mavko, 1996). Other current applications of the derived equations, discussed above, include the implementation of exact numerical inversion methods for small and large angles of incidence. Another area of interest for geophysical exploration is a more detailed study of converted-wave AVO. It can be expected that use of converted-wave data will become more common in the near future. The complexity of the derived reflection coefficient for converted waves implies that the classical intercept-gradient approach in the AVO analysis is not easily applicable to mode conversions.

Finally, based on the experience gained during this thesis research and because of the small azimuthal variation to be expected in most situations, I strongly suggest that any AVO analysis of field data should be complemented by a detailed modeling study to quantify errors introduced by heterogeneity and anisotropy.

REFERENCES

Aki, K., & Richards, P. G. 1980. *Quantitative seismology: theory and methods.* Vol. 1. W. N. Freeman & Co.

Alford, R. M. 1986. Shear data in the presence of azimuthal anisotropy: Dilley, Texas. *In: 56th Annual Internat. Mtg., Soc. Expl. Geophys., Expanded Abstracts.* Soc. Expl. Geophys.

Alkhalifah, T., & Tsvankin, I. 1995. Velocity analysis for transversely isotropic media. *Geophysics*, **60**, 1550–1556.

Banik, N. C. 1987. An effective anisotropy parameter in transversely isotropic media. *Geophysics*, **52**(12), 1654–1664.

Blangy, J. P. 1994. AVO in transversely isotropic media - an overview. *Geophysics*, **59**, 775–781.

Bortfeld, R. 1961. Approximation to the reflection coefficients of plane longitudinal and transverse waves. *Geophysical Prospecting*, **9**, 485–502.

Brekhovskikh, L. M. 1980. *Waves in layered media.* Academic Press, New York.

Castagna, & Backus, Eds. 1993. *Offset dependent reflectivity: theory and methods.* SEG.

Červený, V., & Ravindra, R. 1971. *Theory of seismic head waves.* Univ. of Toronto Press.

Corrigan, D. 1990. The effect of azimuthal anisotropy on the variation of reflectivity with offset. *In: 4IWSA.* Soc. Expl. Geophys.

Crampin, S. 1984a. Anisotropy in exploration seismics. *First Break*, **2**(3), 19–21.

Crampin, S. 1984b. Effective anisotropic constants for wave propagation through cracked solids. *Geophys. J. R. astr. Soc.*, **76**, 135–145.

Crampin, S. 1985. Evidence for aligned cracks in the Earth's crust. *First Break*, **3**, 12–15.

Crampin, S., Bush, I., & Naville, C. 1986. Estimating the internal structure of reservoirs with shear-wave VSP's. *The Leading Edge*, **5**, 35–39.

Daley, P. F., & Hron, F. 1977. Reflection and transmission coefficients for transversely isotropic solids. *Bull. Seis. Soc. Am.*, **67**, 661–675.

Fryer, G. J., & Frazer, L. N. 1987. Seismic waves in stratified anisotropic media – 2: elastodynamic eigensolutions for some anisotropic systems. *Geophys. J. R. astr. Soc.*, **91**, 73–101.

Gajewski, D. 1993. Radiation from point sources in general anisotropic media. *Geophys. J. Int.*, **113**, 299–317.

Gajewski, D., & Pšenčik, I. 1990. Vertical seismic profile synthetics by dynamic raytracing in laterally varying anisotropic structures. *J. geophys. Res.*, **95**, 11301–11315.

Graebner, M. 1992. Plane-wave reflection and transmission coefficients for a transversely isotropic solid (short note). *Geophysics*, **57**(11), 1512–1519.

Grechka, V., & Tsvankin, I. 1996. 3-D description of normal moveout in anisotropic media. *To appear in Geophysics.*

Green, G. 1839. On the law of reflexion and refraction of light. *Transactions of the Cambridge philosophical society*, **7**.

Haugen, G. 1996. AVO-A analysis of a shale over a vertically fractured sandstone. *In: Proceedings of 7IWSA.* Soc. Expl. Geophys.

Helbig, K. 1994. *Foundations of anisotropy for exploration seismics.* Handbook of Geophysical Exploration, vol. 22. Elsevier Science Inc.

Henneke, E. G. 1972. Reflection-refraction of a stress wave at a plane boundary between anisotropic media. *J. Acoust. Soc. Am.*, **51**, 210–217.

Hilterman, F. 1983. *Seismic lithology course, unpublished.*

Hudson, J. A. 1981. Wave speeds and attenuation of elastic waves in material containing cracks. *Geophys. J. R. astr. Soc.*, **64**, 133–150.

Hudson, J. A. 1986. A higher order approximation to the wave propagation constants for a cracked solid. *Geophys. J. R. astr. Soc.*, **87**, 265–274.

Johnson, W. E. 1995. Direct detection of gas in pre-Tertiary sediments? *The Leading Edge*, **14**(2), 119–122.

Keith, C.M., & Crampin, S. 1977. Seismic body waves in anisotropic media: reflection and refraction at a plane interface. *Geophys. J. R. astr. Soc.*, **49**, 181–208.

Kendall, R. R. 1995. Modeling and interpreting shear-waves and fracture anisotropy in South-Central Wyoming. *In: 65nd Annual Internat. Mtg., Soc. Expl. Geophys., Expanded Abstracts.* Soc. Expl. Geophys.

Kim, K. Y., Wrolstad, K. H., & Aminzadeh, F. 1993. Effects of transverse isotropy on P-wave AVO for gas sands. *Geophysics*, **58**(6), 883–888.

Knott, C. G. 1899. Reflection and refraction of elastic waves with seismological applications. *Philosophical Magazine*, **48**(5), 64–97.

Koefoed, O. 1955. On the effect of Poisson's ratio of rock strata on the reflection coefficients of plane waves. *Geophysical Prospecting*, **3**, 381–387.

Lefeuvre, F. 1994. Fracture related anisotropy detection and analysis: and if the P-waves were enough? *Pages 942–945 of: 64th Annual Internat. Mtg., Soc. Expl. Geophys., Expanded Abstracts*, vol. 94.

Li, X., & Kühnel, T. 1996. Mixed mode AVO response in fractured media. *In: 66th Annual Internat. Mtg., Soc. Expl. Geophys., Expanded Abstracts*, vol. 96.

Lynn, H. B., & Thomsen, L. A. 1990. Reflection shear-wave data collected near the principal axes of azimuthal anisotropy. *Geophysics*, **55**(2), 147–156.

Lynn, H. B., Simon, K. M., Bates, C. R., Layman, M., Schneider, R., & Jones, M. 1995. Seismic characterization of a naturally fractured gas reservoir. *Pages 293–296 of: 65th Annual Internat. Mtg., Soc. Expl. Geophys., Expanded Abstracts*, vol. 95.

Mallick, S., & Fraser, L. N. 1991. Reflection/transmission coefficients and azimuthal anisotropy in marine studies. *Geophys. J. Int.*, **105**, 241–252.

Mallick, S., & Frazer, L. N. 1990. Computation of synthetic seismograms for stratified azimuthally anisotropic media. *J. geophys. Res.*, **95**, 8513–8526.

Martin, M. A., & Davis, T. L. 1987. Shear-wave birefringence - a new tool for evaluating fractured reservoirs. *The Leading Edge*, **6**(10), 22–28.

Mueller, M. 1991. Prediction of lateral variability in fracture intensity using multicomponent shear-wave surface seismic as a precursor to horizontal drilling in Austin Chalk. *Geophys. J. Int.*, **107**, 409–415.

Musgrave, M. J. P. 1970. *Crystal acoustics*. Holden Day, San Francisco.

Nishizawa, O. 1982. Seismic velocity anisotropy in a medium containing oriented cracks – transversely isotropic case. *J. Phys. Earth*, **30**, 331–347.

Obolentseva, I. R., & Grechka, V. Y. 1989. *Ray tracing in anisotropic media (algorithms and Fortran codes)*. Institute of Geology and Geophysics Press, Novosibirsk (in Russian).

Ostrander, W. J. 1982. Plane wave reflection coefficients for gas sands at nonnormal angles of incidence. *Page Session:S16.4 of: 52nd Annual Internat. Mtg., Soc. Expl. Geophys., Expanded Abstracts.* Soc. Expl. Geophys.

Peacock, S., & Hudson, J. A. 1990. Seismic properties of rocks with distributions of small cracks. *Geophys. J. Int.*, **102**, 471–484.

Richards, P. G., & Frasier, C. W. 1976. Scattering of elastic waves from depth-dependent inhomogeneities. *Geophysics*, **41**(3), 441–458.

Rolla, M. 1995. Azimuthal AVO analysis, Joffre field, Alberta, Canada. *Pages 1107–1110 of: 65th Annual Internat. Mtg., Soc. Expl. Geophys., Expanded Abstracts*, vol. 95.

Rommel, B.E. 1994. Approximate polarization of plane waves in a medium having weak transverse isotropy. *Geophysics*, **59**, 1605–1612.

Rüger, A. 1996. Analytic insight into shear-wave AVO for fractured reservoirs. *To appear in Proceedings of 7IWSA, special SEG volume on seismic anisotropy, Miami.*

Rüger, A., & Alkhalifah, T. 1996. Efficient anisotropic raytracing. *In: Seismic anisotropy (Fjær, Holt and Rathore, Eds.), SEG, Tulsa*, 556–600.

Rutherford, S. R., & Williams, M. W. 1989. Amplitude-versus-offsets variations in gas sands. *Geophysics*, **54**, 680–688.

Sayers, C. M. 1988. Inversion of ultrasonic wave velocity measurements to obtain microcrack orientation distribution function in rocks. *Ultrasonics*, **26**, 73–77.

Schoenberg, M., & Helbig, K. 1995. Orthorhombic media: modeling elastic wave behavior in a vertically fractured Earth. *Geophysics, in press.*

Schoenberg, M., & Sayers, C. M. 1995. Seismic anisotropy of fractured rocks. *Geophysics*, **60**, 204–211.

Shuck, E. L., Davis, T. L., & Benson, R. D. 1996. Multicomponent 3-D characterization of a coalbed methane reservoir. *Geophysics*, **61**(2), 315–330.

Shuey, R. T. 1985. A simplification of the Zoeppritz-equations. *Geophysics*, **50**(4), 609–614.

Teng, L., & Mavko, G. 1996. Fracture signatures on P-wave AVOZ. *Pages 1818–1821 of: 66th Annual Internat. Mtg., Soc. Expl. Geophys., Expanded Abstracts*, vol. 2.

Thomsen, L. 1986. Weak elastic anisotropy. *Geophysics*, **51**(10), 1954–1966.

Thomsen, L. 1988. Reflection seismology over azimuthally anisotropic media. *Geophysics*, **53**(3), 304–313.

Thomsen, L. 1990. Poisson was not a geophysicist. *The Leading Edge*, **9**(12), 27–29.

Thomsen, L. 1993. Weak anisotropic reflections. *In: Offset dependent reflectivity (Castagna and Backus, Eds.), SEG, Tulsa.*

Thomsen, L. 1995. Elastic anisotropy due to aligned cracks in porous rock. *Geophysical Prospecting*, **43**, 805–829.

Tsvankin, I. 1995a. Body-wave radiation patterns and AVO in transversely isotropic media. *Geophysics*, **60**(5), 1409–1425.

Tsvankin, I. 1995b. *Seismic wavefields in layered isotropic media.* Samizdat Press, Center for Wave Phenomena, Golden, Colorado.

Tsvankin, I. 1996a. Effective parameters and reflection seismic signatures for orthorhombic anisotropy. *In: Center for Wave Phenomena report CWP-199.*

Tsvankin, I. 1996b. *P*-wave signatures and notation for transversely isotropic media: an overview. *Geophysics*, **61**(2), 467–483.

Tsvankin, I. 1996c. Reflection moveout and parameter estimation for horizontal transverse isotropy. *To appear in Geophysics.*

Tsvankin, I., & Chesnokov, E. 1990. Synthesis of body-wave seismograms from point sources in anisotropic media. *J. geophys. Res.*, **95**.

Tsvankin, I., & Thomsen, L. 1994. Nonhyperbolic reflection moveout in anisotropic media. *Geophysics*, **59**(8), 1290–1304.

Ursin, B., & Haugen, G. 1996. Weak-contrast approximation of the elastic scattering matrix in anisotropic media. *To appear in proceedings of workshop on seismic waves in laterally inhomogeneous media, Castle of Trest, Czech Republic.*

White, J. E. 1983. *Underground sound: application of sound waves.* Elsevier.

Wiggins, R., Kenny, G. S., & McClure, C. D. 1983. A method for determining and displaying the shear-velocity reflectivities of a geologic formation. *European Patent Application 0113944.*

Winterstein, D.F. 1990. Velocity anisotropy terminology for geophysicists. *Geophysics*, **55**, 1070–1088.

Wright, J. 1986. Reflection coefficients at pore-fluid contacts as a function of offset (short note). *Geophysics*, **51**(9), 1858–1860.

Wright, J. 1987. The effects of transverse isotropy on reflection amplitudes versus offset. *Geophysics*, **52**, 564–567.

Yardley, G. S.; Graham, G., & Crampin, S. 1991. Viability of shear-wave amplitude versus offset studies in anisotropic media. *Geophys. J. Int.*, **107**, 493–503.

Zoeppritz, K. 1919. Erdbebenwellen, on the reflection and penetration of seismic waves through unstable layers. *Göttinger Nachrichten*, **1**(VII B), 66–84.

Appendix A

DERIVATION OF LINEARIZED VTI SCATTERING COEFFICIENTS

Kinematic and dynamic boundary conditions yield a system of equations that needs to be solved for the scattering coefficients. Using the parameterization introduced in Chapter 2 [equations (2.4)], one obtains a linear system [see equation (3.27)]:

$$\mathbf{M}\begin{pmatrix} R_P & R_{SP} \\ T_P & T_{SP} \\ R_{PS} & R_S \\ T_{PS} & T_S \end{pmatrix} = \mathbf{b}\,. \tag{A.1}$$

The elements m_{ij} of the matrix $\mathbf{M}$ are related to the parameters stated above as follows:

$$\begin{array}{llll} m_{11} = l_{i_1}\sin i_1 & m_{12} = -l_{i_2}\sin i_2 & m_{13} = m_{j_1}\cos j_1 & m_{14} = -m_{j_2}\cos j_2 \\ m_{31} = m_{i_1}\cos i_1 & m_{32} = m_{i_2}\cos i_2 & m_{33} = -l_{j_1}\sin j_1 & m_{34} = -l_{j_2}\sin j_2 \end{array}$$

$$\begin{array}{ll} m_{21} = c_{55}^{(1)}\frac{\sin_{i_1}}{v_{i_1}}\cos i_1(l_{i_1}+m_{i_1}) & m_{22} = c_{55}^{(2)}\frac{\sin_{i_2}}{v_{i_2}}\cos i_2(l_{i_2}+m_{i_2}) \\ m_{23} = c_{55}^{(1)}\frac{1}{v_{j_1}}(m_{j_1}\cos^2 j_1 - l_{j_1}\sin^2 j_1) & m_{24} = c_{55}^{(2)}\frac{1}{v_{j_2}}(m_{j_2}\cos^2 j_2 - l_{j_2}\sin^2 j_2) \\ m_{41} = -c_{13}^{(1)}\frac{\sin^2_{i_1}}{v_{i_1}}l_{i_1} - c_{33}^{(1)}\frac{\cos^2_{i_1}}{v_{i_1}}m_{i_1} & m_{42} = c_{13}^{(2)}\frac{\sin^2_{i_2}}{v_{i_2}}l_{i_2} + c_{33}^{(2)}\frac{\cos^2_{i_2}}{v_{i_2}}m_{i_2} \\ m_{43} = \frac{\sin_{j_1}\cos_{j_1}}{v_{j_1}}(c_{33}^{(1)}l_{j_1} - c_{13}^{(1)}m_{j_1}) & m_{44} = \frac{\sin_{j_2}\cos_{j_2}}{v_{j_2}}(c_{13}^{(2)}m_{j_2} - c_{33}^{(2)}l_{j_2})\,, \end{array}$$

and

$$\mathbf{b} = \begin{pmatrix} -l_{i_1}\sin i_1 & -m_{j_1}\cos j_1 \\ c_{55}^{(1)}\frac{\sin_{i_1}}{v_{i_1}}\cos i_1(l_{i_1}+m_{i_1}) & c_{55}^{(1)}\frac{1}{v_{j_1}}(m_{j_1}\cos^2 j_1 - l_{j_1}\sin^2 j_1) \\ m_{i_1}\cos i_1 & -l_{j_1}\sin j_1 \\ c_{13}^{(1)}\frac{\sin^2_{i_1}}{v_{i_1}}l_{i_1} + c_{33}^{(1)}\frac{\cos^2_{i_1}}{v_{i_1}}m_{i_1} & \frac{\sin_{j_1}\cos_{j_1}}{v_{j_1}}(c_{13}^{(1)}m_{j_1} - c_{33}^{(1)}l_{j_1}) \end{pmatrix}. \tag{A.2}$$

The corresponding unperturbed matrix $\mathbf{M^u}$ in equation (3.30), expressed through the incidence angles i and j is given by

$$\mathbf{M^u} = \begin{pmatrix} \sin i & -\sin i & \cos j & -\cos j \\ 2\bar{\rho}\frac{\bar{V}_{S0}^2}{\bar{V}_{P0}}\sin i\cos i & 2\bar{\rho}\frac{\bar{V}_{S0}^2}{\bar{V}_{P0}}\sin i\cos i & \bar{\rho}\bar{V}_{S0}(\cos^2 j - \sin^2 j) & \bar{\rho}\bar{V}_{S0}(\cos^2 j - \sin^2 j) \\ \cos i & \cos i & -\sin j & -\sin j \\ 2\bar{\rho}\frac{\bar{V}_{S0}^2}{\bar{V}_{P0}}\sin^2 i - \bar{\rho}\bar{V}_{P0} & \bar{\rho}\bar{V}_{P0} - 2\bar{\rho}\frac{\bar{V}_{S0}^2}{\bar{V}_{P0}}\sin^2 i & 2\bar{\rho}\bar{V}_{S0}\sin j\cos j & -2\bar{\rho}\bar{V}_{S0}\sin j\cos j \end{pmatrix}$$

Because of the internal symmetries in $\mathbf{M^u}$, the inverse matrix $(\mathbf{M^u})^{-1}$ has a relatively simple structure:

$$(\mathbf{M^u})^{-1} = \begin{pmatrix} \sin i \frac{\bar{V}_{S0}^2}{\bar{V}_{P0}^2} & \frac{\sin i}{2\bar{\rho}\bar{V}_{P0}\cos i} & \frac{1-2\frac{\bar{V}_{S0}^2}{\bar{V}_{P0}^2}\sin^2 i}{2\cos i} & \frac{-1}{2\bar{\rho}\bar{V}_{P0}} \\ -\sin i \frac{\bar{V}_{S0}^2}{\bar{V}_{P0}^2} & \frac{\sin i}{2\bar{\rho}\bar{V}_{P0}\cos i} & \frac{1-2\frac{\bar{V}_{S0}^2}{\bar{V}_{P0}^2}\sin^2 i}{2\cos i} & \frac{1}{2\bar{\rho}\bar{V}_{P0}} \\ \frac{1-2\frac{\bar{V}_{S0}^2}{\bar{V}_{P0}^2}\sin^2 i}{2\cos j} & \frac{1}{2\bar{\rho}\bar{V}_{S0}} & -\frac{\bar{V}_{S0}}{\bar{V}_{P0}}\sin i & \frac{\sin i}{2\bar{\rho}\bar{V}_{P0}\cos j} \\ \frac{2\frac{\bar{V}_{S0}^2}{\bar{V}_{P0}^2}\sin^2 i-1}{2\cos j} & \frac{1}{2\bar{\rho}\bar{V}_{S0}} & -\frac{\bar{V}_{S0}}{\bar{V}_{P0}}\sin i & \frac{-\sin i}{2\bar{\rho}\bar{V}_{P0}\cos j} \end{pmatrix}.$$

An important step in solving for the approximate reflection coefficients is to derive the *P*-wave and *SV*-wave phase velocities, linearized in the small parameters d_i [equations (3.28)]. Using equations (3.13), (3.14) and (3.29), we find:

$$\begin{aligned} v_{i_1} &= \bar{V}_{P0}\left(1 - \frac{1}{2}\frac{\Delta V_{P0}}{\bar{V}_{P0}} + \delta_1 \sin^2 i_1 \cos^2 i_1 + \epsilon_1 \sin^4 i_1\right) \\ v_{j_1} &= \bar{V}_{S0}\left(1 - \frac{1}{2}\frac{\Delta V_{S0}}{\bar{V}_{S0}} + \frac{\bar{V}_{P0}^2}{\bar{V}_{S0}^2}(\epsilon_1 - \delta_1) \sin^2 j_1 \cos^2 j_1\right) \\ v_{i_2} &= \bar{V}_{P0}\left(1 + \frac{1}{2}\frac{\Delta V_{P0}}{\bar{V}_{P0}} + \delta_2 \sin^2 i_2 \cos^2 i_2 + \epsilon_2 \sin^4 i_2\right) \\ v_{j_2} &= \bar{V}_{S0}\left(1 + \frac{1}{2}\frac{\Delta V_{S0}}{\bar{V}_{S0}} + \frac{\bar{V}_{P0}^2}{\bar{V}_{S0}^2}(\epsilon_2 - \delta_2) \sin^2 j_2 \cos^2 j_2\right) \end{aligned} \qquad \text{(A.3)}$$

A second key element in obtaining the reflection and transmission coefficients in anisotropic media is the derivation of polarization vectors. Equations describing the direction of compressional-wave polarization in VTI media have been published by Rommel (1994) and Tsvankin (1996b). Denoting the phase and polarization angles with the symmetry axis as θ and γ, respectively, one can show that

$$\begin{aligned} \cos\gamma &= (1 - f \sin^2\theta\,[\delta + 2(\epsilon - \delta)\sin^2\theta\,])\cos\theta \\ \sin\gamma &= (1 + f \cos^2\theta\,[\delta + 2(\epsilon - \delta)\sin^2\theta\,])\sin\theta\,, \end{aligned} \qquad \text{(A.4)}$$

with $f = V_{P0}^2/(V_{P0}^2 - V_{S0}^2)$. Equation (A.4), together with equations (2.4), yields:

$$\begin{aligned} \mathrm{l}_{i_1} &= 1 + \bar{f}\cos^2 i_1[\delta_1 + 2(\epsilon_1 - \delta_1)\sin^2 i_1] \\ \mathrm{m}_{i_1} &= 1 - \bar{f}\sin^2 i_1[\delta_1 + 2(\epsilon_1 - \delta_1)\sin^2 i_1] \\ \mathrm{l}_{j_1} &= 1 + \bar{f}\cos^2 j_1[\delta_1 + 2(\epsilon_1 - \delta_1)\sin^2 j_1] \\ \mathrm{m}_{j_1} &= 1 - \bar{f}\sin^2 j_1[\delta_1 + 2(\epsilon_1 - \delta_1)\sin^2 j_1] \end{aligned} \qquad \text{(A.5)}$$

The corresponding expressions for $l_{i_2}, m_{i_2}, l_{j_2}$ and m_{i_2} can be obtained from equations (A.5) by simply interchanging the subscripts 1 and 2. The phase angles of the scattered wave modes need to be related to the phase angle of the incident wave. The most straightforward approach is to relate each phase angle to the horizontal slowness p, which is preserved at the reflecting boundary. The above equations are sufficient to finish the derivation and evaluate equation (3.32).

Here, I state the eight linearized reflection and transmission coefficients evaluated using the perturbation approach discussed above. Reflection and transmission coefficients are given in a form that allows one to distinguish between the isotropic contribution and the additional term caused by the anisotropy. For example, the P-wave reflection coefficient is stated in the form $\grave{P}\acute{P} = \grave{P}\acute{P}^{\text{iso}} + \grave{P}\acute{P}^{\text{anis}}$.

- P-wave reflection coefficient

$$\begin{aligned}
\grave{P}\acute{P}^{\text{iso}} &= 1/2\frac{\Delta Z}{\bar{Z}} + 1/2\left[\frac{\Delta V_{P0}}{\bar{V}_{P0}} - \left(\frac{2\bar{V}_{S0}}{\bar{V}_{P0}}\right)^2 \frac{\Delta G}{\bar{G}}\right]\sin^2 i_1 \\
&\quad +1/2\frac{\Delta V_{P0}}{\bar{V}_{P0}}\sin^2 i_1 \tan^2 i_1 \\
\grave{P}\acute{P}^{\text{anis}} &= 1/2\,(\delta_2 - \delta_1)\sin^2 i_1 + 1/2\,(\epsilon_2 - \epsilon_1)\sin^2 i_1 \tan^2 i_1
\end{aligned}$$

- P-wave transmission coefficient

$$\begin{aligned}
\grave{P}\grave{P}^{\text{iso}} &= 1 - 1/2\frac{\Delta Z}{\bar{Z}} + 1/2\frac{\Delta V_{P0}}{\bar{V}_{P0}}\sin^2 i_1 + 1/2\frac{\Delta V_{P0}}{\bar{V}_{P0}}\sin^2 i_1 \tan^2 i_1 \\
\grave{P}\grave{P}^{\text{anis}} &= 1/2\,(\delta_2 - \delta_1)\sin^2 i_1 + 1/2\,(\epsilon_2 - \epsilon_1)\sin^2 i_1 \tan^2 i_1 \\
&\quad +(\delta_1 - \delta_2 - \epsilon_1 + \epsilon_2)\sin^4 i_1
\end{aligned}$$

- SV-wave reflection coefficient

$$\begin{aligned}
\grave{S}\acute{S}^{\text{iso}} &= -1/2\left(\frac{\Delta\rho}{\bar{\rho}} + \frac{\Delta V_{S0}}{\bar{V}_{S0}}\right) + \left(\frac{7}{2}\frac{\Delta V_{S0}}{\bar{V}_{S0}} + 2\frac{\Delta\rho}{\bar{\rho}}\right)\sin^2 j_1 \\
&\quad -1/2\frac{\Delta V_{S0}}{\bar{V}_{S0}}\sin^2 j_1 \tan^2 j_1 \\
\grave{S}\acute{S}^{\text{anis}} &= -1/2\left(\frac{\bar{V}_{P0}}{\bar{V}_{S0}}\right)^2 (\delta_2 - \delta_1 - \epsilon_2 + \epsilon_1)\sin^2 j_1
\end{aligned}$$

- SV-wave transmission coefficient

$$\begin{aligned}
\grave{S}\grave{S}^{\text{iso}} &= 1 - 1/2\left(\frac{\Delta\rho}{\bar{\rho}} + \frac{\Delta V_{S0}}{\bar{V}_{S0}}\right) + 1/2\frac{\Delta V_{S0}}{\bar{V}_{S0}}\sin^2 j_1 \\
&\quad +1/2\frac{\Delta V_{S0}}{\bar{V}_{S0}}\sin^2 j_1 \tan^2 j_1
\end{aligned}$$

$$\grave{S}\acute{S}^{\text{anis}} = -1/2\left(\frac{\bar{V}_{P0}}{\bar{V}_{S0}}\right)^2(\delta_2-\delta_1-\epsilon_2+\epsilon_1)\sin^2 j_1 + \left(\frac{\bar{V}_{P0}}{\bar{V}_{S0}}\right)^2(\delta_2-\delta_1-\epsilon_2+\epsilon_1)\sin^4 j_1$$

- *SH*-wave reflection coefficient

$$\begin{aligned}\grave{S}\acute{S}^{\text{iso}} &= -1/2\left(\frac{\Delta\rho}{\bar{\rho}}+\frac{\Delta V_{S0}}{\bar{V}_{S0}}\right)+1/2\frac{\Delta V_{S0}}{\bar{V}_{S0}}\sin^2 j_1 \\ &\quad +1/2\frac{\Delta V_{S0}}{\bar{V}_{S0}}\sin^2 j_1\tan^2 j_1 \\ \grave{S}\acute{S}^{\text{anis}} &= 1/2\,(\gamma_2-\gamma_1)\sin^2 j_1+1/2\,(\gamma_2-\gamma_1)\sin^2 j_1\tan^2 j_1\end{aligned}$$

- *SH*-wave transmission coefficient

$$\begin{aligned}\grave{S}\grave{S}^{\text{iso}} &= 1-1/2\left(\frac{\Delta\rho}{\bar{\rho}}+\frac{\Delta V_{S0}}{\bar{V}_{S0}}\right)+1/2\frac{\Delta V_{S0}}{\bar{V}_{S0}}\sin^2 j_1 \\ &\quad +1/2\frac{\Delta V_{S0}}{\bar{V}_{S0}}\sin^2 j_1\tan^2 j_1 \\ \grave{S}\grave{S}^{\text{anis}} &= 1/2\,(\gamma_2-\gamma_1)\sin^2 j_1+1/2\,(\gamma_2-\gamma_1)\sin^2 j_1\tan^2 j_1\end{aligned}$$

- *PS*-converted wave reflection coefficient

$$\begin{aligned}\grave{P}\acute{S}^{\text{iso}} &= -1/2\frac{\Delta\rho}{\bar{\rho}}\frac{\sin i_1}{\cos j_1}-\frac{\bar{V}_{S0}}{\bar{V}_{P0}}\left(\frac{\Delta\rho}{\bar{\rho}}+2\frac{\Delta V_{S0}}{\bar{V}_{S0}}\right)\sin i_1\cos i_1 \\ &\quad +\left(\frac{\bar{V}_{S0}}{\bar{V}_{P0}}\right)^2\left(2\frac{\Delta V_{S0}}{\bar{V}_{S0}}+\frac{\Delta\rho}{\bar{\rho}}\right)\frac{\sin^3 i_1}{\cos j_1} \\ \grave{P}\acute{S}^{\text{anis}} &= \left[\left(\frac{\bar{V}_{P0}^2}{2\,(\bar{V}_{P0}^2-\bar{V}_{S0}^2)\cos j_1}-\frac{\bar{V}_{P0}\bar{V}_{S0}\cos i_1}{2\,(\bar{V}_{P0}^2-\bar{V}_{S0}^2)}\right)(\delta_2-\delta_1)\right]\sin i_1 \\ &\quad +\left[\frac{\bar{V}_{S0}\bar{V}_{P0}\cos i_1}{(\bar{V}_{P0}^2-\bar{V}_{S0}^2)}(\delta_2-\delta_1+\epsilon_1-\epsilon_2)\right]\sin^3 i_1 \\ &\quad -\left[\frac{\bar{V}_{P0}^2}{(\bar{V}_{P0}^2-\bar{V}_{S0}^2)\cos j_1}(\delta_2-\delta_1+\epsilon_1-\epsilon_2)\right]\sin^3 i_1 \\ &\quad +\left[\frac{\bar{V}_{S0}^2}{2(\bar{V}_{P0}^2-\bar{V}_{S0}^2)\cos j_1}(\delta_1-\delta_2)\right]\sin^3 i_1 \\ &\quad +\left[\frac{\bar{V}_{S0}^2}{(\bar{V}_{P0}^2-\bar{V}_{S0}^2)\cos j_1}(\delta_2-\delta_1+\epsilon_1-\epsilon_2)\right]\sin^5 i_1\end{aligned}$$

- *PS*-converted wave transmission coefficient

$$
\begin{aligned}
\grave{P}\grave{S}^{\text{iso}} &= 1/2\,\frac{\Delta\rho}{\bar{\rho}}\,\frac{\sin i_1}{\cos j_1} \\
&\quad - \frac{\bar{V}_{S0}}{\bar{V}_{P0}}\left(\frac{\Delta\rho}{\bar{\rho}} + 2\frac{\Delta V_{S0}}{\bar{V}_{S0}}\right)\sin i_1 \cos i_1 \\
&\quad - \left(\frac{\bar{V}_{S0}}{\bar{V}_{P0}}\right)^2\left(2\,\frac{\Delta V_{S0}}{\bar{V}_{S0}} + \frac{\Delta\rho}{\bar{\rho}}\right)\frac{\sin^3 i_1}{\cos j_1} \\
\grave{P}\grave{S}^{\text{anis}} &= \left[\left(\frac{\bar{V}_{P0}^2}{2\,(\bar{V}_{P0}^2 - \bar{V}_{S0}^2)\cos j_1} + \frac{\bar{V}_{P0}\bar{V}_{S0}\cos i_1}{2\,(\bar{V}_{P0}^2 - \bar{V}_{S0}^2)}\right)(\delta_1 - \delta_2)\right]\sin i_1 \\
&\quad + \left[\frac{\bar{V}_{S0}\bar{V}_{P0}\cos i_1}{(\bar{V}_{P0}^2 - \bar{V}_{S0}^2)}\,(\delta_2 - \delta_1 + \epsilon_1 - \epsilon_2)\right]\sin^3 i_1 \\
&\quad + \left[\frac{\bar{V}_{P0}^2}{(\bar{V}_{P0}^2 - \bar{V}_{S0}^2)\cos j_1}\,(\delta_2 - \delta_1 + \epsilon_1 - \epsilon_2)\right]\sin^3 i_1 \\
&\quad + \left[\frac{\bar{V}_{S0}^2}{2(\bar{V}_{P0}^2 - \bar{V}_{S0}^2)\cos j_1}\,(\delta_2 - \delta_1)\right]\sin^3 i_1 \\
&\quad + \left[\frac{\bar{V}_{S0}^2}{(\bar{V}_{P0}^2 - \bar{V}_{S0}^2)\cos j_1}\,(\delta_1 - \delta_2 + \epsilon_2 - \epsilon_1)\right]\sin^5 i_1
\end{aligned}
$$

- *SP*-converted wave reflection coefficient

$$
\begin{aligned}
\grave{S}\acute{P}^{\text{iso}} &= -1/2\,\frac{\Delta\rho}{\bar{\rho}}\,\frac{\sin j_1}{\cos i_1} - \frac{\bar{V}_{S0}}{\bar{V}_{P0}}\left(\frac{\Delta\rho}{\bar{\rho}} + 2\frac{\Delta V_{S0}}{\bar{V}_{S0}}\right)\sin j_1 \cos j_1 \\
&\quad + \left(2\frac{\Delta V_{S0}}{\bar{V}_{S0}} + \frac{\Delta\rho}{\bar{\rho}}\right)\frac{\sin^3 j_1}{\cos i_1} \\
\grave{S}\acute{P}^{\text{anis}} &= \left[\left(\frac{\bar{V}_{P0}\bar{V}_{S0}\cos j_1}{2(\bar{V}_{P0}^2 - \bar{V}_{S0}^2)} - \frac{\bar{V}_{P0}^2\cos^2 j_1}{2(\bar{V}_{P0}^2 - \bar{V}_{S0}^2)\cos i_1}\right)(\delta_1 - \delta_2)\right]\sin j_1 \\
&\quad + \left[\frac{\bar{V}_{P0}^3\cos j_1}{\bar{V}_{S0}\,(\bar{V}_{P0}^2 - \bar{V}_{S0}^2)}\,(\delta_2 - \delta_1 + \epsilon_1 - \epsilon_2)\right]\sin^3 j_1 \\
&\quad - \left[\frac{\bar{V}_{P0}^4\cos^2 j_1}{\bar{V}_{S0}^2\,(\bar{V}_{P0}^2 - \bar{V}_{S0}^2)\cos i_1}\,(\delta_2 - \delta_1 + \epsilon_1 - \epsilon_2)\right]\sin^3 j_1
\end{aligned}
$$

- *SP*-converted wave transmission coefficient

$$
\begin{aligned}
\grave{S}\grave{P}^{\text{iso}} &= -1/2\,\frac{\Delta\rho}{\bar{\rho}}\,\frac{\sin j_1}{\cos i_1} + \frac{\bar{V}_{S0}}{\bar{V}_{P0}}\left(\frac{\Delta\rho}{\bar{\rho}} + 2\frac{\Delta V_{S0}}{\bar{V}_{S0}}\right)\sin j_1 \cos j_1 \\
&\quad + \left(2\frac{\Delta V_{S0}}{\bar{V}_{S0}} + \frac{\Delta\rho}{\bar{\rho}}\right)\frac{\sin^3 j_1}{\cos i_1}
\end{aligned}
$$

Appendix C

CHRISTOFFEL EQUATIONS FOR SYMMETRY PLANE PROPAGATION

The study of Christoffel systems is the key to understanding seismic wave propagation and analyzing analogies between waves propagating in different symmetry systems. The following collection of determinants of the Christoffel system proved to be very valuable for this study. The elements of the Christoffel determinants are given in terms of the density normalized stiffness tensor and are shown in reduced-index notation (using the Voigt recipe).

For symmetry-plane propagation, the Christoffel determinants $\mathbf{C}_{\text{iso}}, \mathbf{C}_{\text{VTI}}, \mathbf{C}_{\text{HTI}}$ and $\mathbf{C}_{\text{Orth}}$ for isotropic, transversely isotropic media with vertical and horizontal axis of symmetry and orthorhombic media are given by:

Propagation in $[x_1, x_3]-$plane

$$\mathbf{C}_{\text{iso}} = \begin{vmatrix} -1 + a_{11}p_1^2 + a_{55}p_3^2 & 0 & (a_{11} - a_{55})p_1p_3 \\ 0 & -1 + a_{55}p_1^2 + a_{55}p_3^2 & 0 \\ (a_{11} - a_{55})p_1p_3 & 0 & -1 + a_{55}p_1^2 + a_{11}p_3^2 \end{vmatrix}$$

$$\mathbf{C}_{\text{VTI}} = \begin{vmatrix} -1 + a_{11}p_1^2 + a_{55}p_3^2 & 0 & (a_{13} + a_{55})p_1p_3 \\ 0 & -1 + a_{66}p_1^2 + a_{55}p_3^2 & 0 \\ (a_{13} + a_{55})p_1p_3 & 0 & -1 + a_{55}p_1^2 + a_{33}p_3^2 \end{vmatrix}$$

$$\mathbf{C}_{\text{HTI}} = \begin{vmatrix} -1 + a_{11}p_1^2 + a_{55}p_3^2 & 0 & (a_{13} + a_{55})p_1p_3 \\ 0 & -1 + a_{55}p_1^2 + a_{44}p_3^2 & 0 \\ (a_{13} + a_{55})p_1p_3 & 0 & -1 + a_{55}p_1^2 + a_{33}p_3^2 \end{vmatrix}$$

$$\mathbf{C}_{\text{Orth}} = \begin{vmatrix} -1 + a_{11}p_1^2 + a_{55}p_3^2 & 0 & (a_{13} + a_{55})p_1p_3 \\ 0 & -1 + a_{66}p_1^2 + a_{44}p_3^2 & 0 \\ (a_{13} + a_{55})p_1p_3 & 0 & -1 + a_{55}p_1^2 + a_{33}p_3^2 \end{vmatrix}$$

Propagation in $[x_2, x_3]-$plane

$$\mathbf{C}_{\text{iso}} = \begin{vmatrix} -1 + a_{55}p_2^2 + a_{55}p_3^2 & 0 & 0 \\ 0 & -1 + a_{11}p_2^2 + a_{55}p_3^2 & (a_{11} - a_{55})p_2p_3 \\ 0 & (a_{11} - a_{55})p_2p_3 & -1 + a_{55}p_2^2 + a_{11}p_3^2 \end{vmatrix}$$

$$\mathbf{C}_{\mathrm{VTI}} = \begin{vmatrix} -1 + a_{66}p_2^2 + a_{55}p_3^2 & 0 & 0 \\ 0 & -1 + a_{11}p_2^2 + a_{55}p_3^2 & (a_{13} + a_{55})p_2p_3 \\ 0 & (a_{13} + a_{55})p_2p_3 & -1 + a_{55}p_2^2 + a_{33}p_3^2 \end{vmatrix}$$

$$\mathbf{C}_{\mathrm{HTI}} = \begin{vmatrix} -1 + a_{55}p_2^2 + a_{55}p_3^2 & 0 & 0 \\ 0 & -1 + a_{33}p_2^2 + a_{44}p_3^2 & (a_{33} - a_{44})p_2p_3 \\ 0 & (a_{33} - a_{44})p_2p_3 & -1 + a_{44}p_2^2 + a_{33}p_3^2 \end{vmatrix}$$

$$\mathbf{C}_{\mathrm{Orth}} = \begin{vmatrix} -1 + a_{66}p_2^2 + a_{55}p_3^2 & 0 & 0 \\ 0 & -1 + a_{22}p_2^2 + a_{44}p_3^2 & (a_{23} + a_{44})p_2p_3 \\ 0 & (a_{23} + a_{44})p_2p_3 & -1 + a_{44}p_2^2 + a_{33}p_3^2 \end{vmatrix}$$

Appendix D

APPROXIMATE REFLECTION AND TRANSMISSION COEFFICIENTS FOR SYMMETRY PLANES IN HTI MEDIA

The same assumption as for the expressions shown in Appendix A hold for the following HTI coefficients. The medium parameters are defined in the main text (see Chapters 4,5,6).

- *P*-wave reflection coefficient (isotropy plane)

$$\grave{P}\acute{P} = 1/2\frac{\Delta Z}{\bar{Z}} + 1/2\left[\frac{\Delta\alpha}{\bar{\alpha}} - \left(\frac{2\bar{\beta}}{\bar{\alpha}}\right)^2\frac{\Delta G}{\bar{G}}\right]\sin^2 i_1 + 1/2\frac{\Delta\alpha}{\bar{\alpha}}\sin^2 i_1\tan^2 i_1$$

- *P*-wave transmission coefficient (isotropy plane)

$$\grave{P}\grave{P} = 1 - 1/2\frac{\Delta Z}{\bar{Z}} + 1/2\frac{\Delta\alpha}{\bar{\alpha}}\sin^2 i_1 + 1/2\frac{\Delta\alpha}{\bar{\alpha}}\sin^2 i_1\tan^2 i_1$$

- $S^{\parallel}$-wave reflection coefficient (isotropy plane)

$$\grave{S}^{\parallel}\acute{S}^{\parallel} = -1/2\left(\frac{\Delta\rho}{\bar{\rho}} + \frac{\Delta\beta}{\bar{\beta}}\right) + \left(\frac{7}{2}\frac{\Delta\beta}{\bar{\beta}} + 2\frac{\Delta\rho}{\bar{\rho}}\right)\sin^2 j_1 - 1/2\frac{\Delta\beta}{\bar{\beta}}\sin^2 j_1\tan^2 j_1$$

- $S^{\parallel}$-wave transmission coefficient (isotropy plane)

$$\grave{S}^{\parallel}\grave{S}^{\parallel} = 1 - 1/2\left(\frac{\Delta\rho}{\bar{\rho}} + \frac{\Delta\beta}{\bar{\beta}}\right) + 1/2\frac{\Delta\beta}{\bar{\beta}}\sin^2 j_1 + 1/2\frac{\Delta\beta}{\bar{\beta}}\sin^2 j_1\tan^2 j_1$$

- $S^{\perp}$-wave reflection coefficient (isotropy plane)

$$\begin{aligned}\grave{S}^{\perp}\acute{S}^{\perp} &= -1/2\left(\frac{\Delta\rho}{\bar{\rho}}+\frac{\Delta\beta}{\bar{\beta}}+\gamma_1-\gamma_2\right)\\ &\quad +1/2\left(\frac{\Delta\beta}{\bar{\beta}}+\gamma_1-\gamma_2\right)\sin^2 j_1\\ &\quad +1/2\left(\frac{\Delta\beta}{\bar{\beta}}+\gamma_1-\gamma_2\right)\sin^2 j_1\tan^2 j_1\end{aligned}$$

- $S^{\perp}$-wave transmission coefficient (isotropy plane)

$$\begin{aligned}\grave{S}^{\perp}\grave{S}^{\perp} &= 1-1/2\left(\frac{\Delta\rho}{\bar{\rho}}+\frac{\Delta\beta}{\bar{\beta}}+\gamma_1-\gamma_2\right)\\ &\quad +1/2\left(\frac{\Delta\beta}{\bar{\beta}}+\gamma_1-\gamma_2\right)\sin^2 j_1\\ &\quad +1/2\left(\frac{\Delta\beta}{\bar{\beta}}+\gamma_1-\gamma_2\right)\sin^2 j_1\tan^2 j_1\end{aligned}$$

- $PS^{\parallel}$ reflection coefficient (isotropy plane)

$$\begin{aligned}\grave{P}\acute{S}^{\parallel} &= -1/2\frac{\Delta\rho}{\bar{\rho}}\frac{\sin i_1}{\cos j_1}-\frac{\bar{\beta}}{\bar{\alpha}}\left(\frac{\Delta\rho}{\bar{\rho}}+2\frac{\Delta\beta}{\bar{\beta}}\right)\sin i_1\cos i_1\\ &\quad +\left(\frac{\bar{\beta}}{\bar{\alpha}}\right)^2\left(2\frac{\Delta\beta}{\bar{\beta}}+\frac{\Delta\rho}{\bar{\rho}}\right)\frac{\sin^3 i_1}{\cos j_1}\end{aligned}$$

- $PS^{\parallel}$ transmission coefficient (isotropy plane)

$$\begin{aligned}\grave{P}\grave{S}^{\parallel} &= 1/2\frac{\Delta\rho}{\bar{\rho}}\frac{\sin i_1}{\cos j_1}-\frac{\bar{\beta}}{\bar{\alpha}}\left(\frac{\Delta\rho}{\bar{\rho}}+2\frac{\Delta\beta}{\bar{\beta}}\right)\sin i_1\cos i_1\\ &\quad -\left(\frac{\bar{\beta}}{\bar{\alpha}}\right)^2\left(2\frac{\Delta\beta}{\bar{\beta}}+\frac{\Delta\rho}{\bar{\rho}}\right)\frac{\sin^3 i_1}{\cos j_1}\end{aligned}$$

- $S^{\parallel}P$ reflection coefficient (isotropy plane)

$$\begin{aligned}\grave{S}^{\parallel}\acute{P} &= -1/2\frac{\Delta\rho}{\bar{\rho}}\frac{\sin j_1}{\cos i_1}-\frac{\bar{\beta}}{\bar{\alpha}}\left(\frac{\Delta\rho}{\bar{\rho}}+2\frac{\Delta\beta}{\bar{\beta}}\right)\sin j_1\cos j_1\\ &\quad +\left(2\frac{\Delta\beta}{\bar{\beta}}+\frac{\Delta\rho}{\bar{\rho}}\right)\frac{\sin^3 j_1}{\cos i_1}\end{aligned}$$

- $S^{\parallel}P$ transmission coefficient (isotropy plane)

$$\begin{aligned}\grave{S}^{\parallel}\grave{P} &= -1/2\,\frac{\Delta\rho}{\bar{\rho}}\frac{\sin j_1}{\cos i} + \frac{\bar{\beta}}{\bar{\alpha}}\left(\frac{\Delta\rho}{\bar{\rho}} + 2\frac{\Delta\beta}{\bar{\beta}}\right)\sin j_1\cos j_1 \\ &\quad + \left(2\frac{\Delta\beta}{\bar{\beta}} + \frac{\Delta\rho}{\bar{\rho}}\right)\frac{\sin^3 j_1}{\cos i_1}\end{aligned}$$

- P-wave reflection coefficient (symmetry-axis plane)

$$\begin{aligned}\grave{P}\acute{P} &= \frac{1}{2}\frac{\Delta Z}{\bar{Z}} + \frac{1}{2}\left\{\frac{\Delta\alpha}{\bar{\alpha}} - 4\left(\frac{\bar{\beta}}{\bar{\alpha}}\right)^2\left(\frac{\Delta G}{\bar{G}} + 2(\gamma_1-\gamma_2)\right)\right. \\ &\quad \left. + \delta_2^{(V)} - \delta_1^{(V)}\right\}\sin^2 i_1 \\ &\quad + \frac{1}{2}\left\{\frac{\Delta\alpha}{\bar{\alpha}} + \epsilon_2^{(V)} - \epsilon_1^{(V)}\right\}\sin^2 i_1\tan^2 i_1\end{aligned}$$

- P-wave transmission coefficient (symmetry-axis plane)

$$\begin{aligned}\grave{P}\grave{P} &= 1 - \frac{1}{2}\frac{\Delta Z}{\bar{Z}} + \frac{1}{2}\left\{\frac{\Delta\alpha}{\bar{\alpha}} + \delta_2^{(V)} - \delta_1^{(V)}\right\}\sin^2 i_1 \\ &\quad + \frac{1}{2}\left\{\frac{\Delta\alpha}{\bar{\alpha}} + \epsilon_2^{(V)} - \epsilon_1^{(V)}\right\}\sin^2 i_1\tan^2 i_1 \\ &\quad + \left\{\delta_1^{(V)} - \delta_2^{(V)} + \epsilon_2^{(V)} - \epsilon_1^{(V)}\right\}\sin^4 i_1,\end{aligned}$$

- $S^{\perp}$-wave reflection coefficient (symmetry-axis plane)

$$\begin{aligned}\grave{S}^{\perp}\acute{S}^{\perp} &= -1/2\left(\frac{\Delta\rho}{\bar{\rho}} + \frac{\Delta\beta}{\bar{\beta}} + \gamma_1 - \gamma_2\right) \\ &\quad + \left\{\frac{7}{2}\left(\frac{\Delta\beta}{\bar{\beta}} + \gamma_1 - \gamma_2\right) + 2\frac{\Delta\rho}{\bar{\rho}} - 1/2\left(\frac{\bar{\alpha}}{\bar{\beta}}\right)^2(\delta_2^{(V)} - \delta_1^{(V)} - \epsilon_2^{(V)} + \epsilon_1^{(V)})\right\}\sin^2 j_1 \\ &\quad - 1/2\left(\frac{\Delta\beta}{\bar{\beta}} + \gamma_1 - \gamma_2\right)\sin^2 j_1\tan^2 j_1\end{aligned}$$

- $S^{\perp}$-wave transmission coefficient (symmetry-axis plane)

$$\begin{aligned}\grave{S}^{\perp}\grave{S}^{\perp} &= 1 - 1/2\left(\frac{\Delta\rho}{\bar{\rho}} + \frac{\Delta\beta}{\bar{\beta}} + \gamma_1 - \gamma_2\right) \\ &\quad + \frac{1}{2}\left\{\frac{\Delta\beta}{\bar{\beta}} + \gamma_1 - \gamma_2 - 1/2\left(\frac{\bar{\alpha}}{\bar{\beta}}\right)^2(\delta_2^{(V)} - \delta_1^{(V)} - \epsilon_2^{(V)} + \epsilon_1^{(V)})\right\}\sin^2 j_1\end{aligned}$$

$$+\left(\frac{\Delta\beta}{\bar{\beta}}+\gamma_1-\gamma_2\right)\sin^2 j_1\tan^2 j_1$$
$$+\left(\frac{\bar{\alpha}}{\bar{\beta}}\right)^2\left(\delta_2^{(V)}-\delta_1^{(V)}-\epsilon_2^{(V)}+\epsilon_1^{(V)}\right)\sin^4 j_1$$

- $S^{\parallel}$-wave reflection coefficient (symmetry-axis plane)

$$\grave{S}^{\parallel}\acute{S}^{\parallel} = -1/2\left(\frac{\Delta\rho}{\bar{\rho}}+\frac{\Delta\beta}{\bar{\beta}}\right) + \frac{1}{2}\left(\frac{\Delta\beta}{\bar{\beta}}+\gamma_1-\gamma_2\right)\sin^2 j_1 + \frac{1}{2}\left(\frac{\Delta\beta}{\bar{\beta}}+\gamma_1-\gamma_2\right)\sin^2 j_1\tan^2 j_1$$

- $S^{\parallel}$-wave transmission coefficient (symmetry-axis plane)

$$\grave{S}^{\parallel}\acute{S}^{\parallel} = 1+\grave{S}^{\parallel}\acute{S}^{\parallel}$$

- $PS^{\perp}$ reflection coefficient (symmetry-axis plane)

$$\begin{aligned}\grave{P}\acute{S}^{\perp} = & -1/2\frac{\Delta\rho}{\bar{\rho}}\frac{\sin i_1}{\cos j_1}\\ & -\frac{\bar{\beta}}{\bar{\alpha}}\left\{\frac{\Delta\rho}{\bar{\rho}}+2\left(\frac{\Delta\beta}{\bar{\beta}}+\gamma_1-\gamma_2\right)\right\}\sin i_1\cos i_1\\ & +\left(\frac{\bar{\beta}}{\bar{\alpha}}\right)^2\left\{2\left(\frac{\Delta\beta}{\bar{\beta}}+\gamma_1-\gamma_2\right)+\frac{\Delta\rho}{\bar{\rho}}\right\}\frac{\sin^3 i_1}{\cos j_1}\\ & +\left[\left(\frac{\bar{\alpha}^2}{2\left(\bar{\alpha}^2-\bar{\beta}^2\right)\cos j_1}-\frac{\bar{\alpha}\bar{\beta}\cos i_1}{2\left(\bar{\alpha}^2-\bar{\beta}^2\right)}\right)\left(\delta_2^{(V)}-\delta_1^{(V)}\right)\right]\sin i_1\\ & +\left[\frac{\bar{\beta}\bar{\alpha}\cos i_1}{\left(\bar{\alpha}^2-\bar{\beta}^2\right)}\left(\delta_2^{(V)}-\delta_1^{(V)}+\epsilon_1^{(V)}-\epsilon_2^{(V)}\right)\right]\sin^3 i_1\\ & -\left[\frac{\bar{\alpha}^2}{\left(\bar{\alpha}^2-\bar{\beta}^2\right)\cos j_1}\left(\delta_2^{(V)}-\delta_1^{(V)}+\epsilon_1^{(V)}-\epsilon_2^{(V)}\right)\right]\sin^3 i_1\\ & +\left[\frac{\bar{\beta}^2}{2\left(\bar{\alpha}^2-\bar{\beta}^2\right)\cos j_1}\left(\delta_1^{(V)}-\delta_2^{(V)}\right)\right]\sin^3 i_1\\ & +\left[\frac{\bar{\beta}^2}{\left(\bar{\alpha}^2-\bar{\beta}^2\right)\cos j_1}\left(\delta_2^{(V)}-\delta_1^{(V)}+\epsilon_1^{(V)}-\epsilon_2^{(V)}\right)\right]\sin^5 i_1\end{aligned}$$

- $PS^{\perp}$ transmission coefficient (symmetry-axis plane)

$$\grave{P}\grave{S}^{\perp} = 1/2\frac{\Delta\rho}{\bar{\rho}}\frac{\sin i_1}{\cos j_1}$$

$$
\begin{aligned}
&- \frac{\bar{\beta}}{\bar{\alpha}} \left\{ \frac{\Delta\rho}{\bar{\rho}} + 2\left(\frac{\Delta\beta}{\bar{\beta}} + \gamma_1 - \gamma_2 \right) \right\} \sin i_1 \cos i_1 \\
&- \left(\frac{\bar{\beta}}{\bar{\alpha}} \right)^2 \left\{ 2\left(\frac{\Delta\beta}{\bar{\beta}} + \gamma_1 - \gamma_2 \right) + \frac{\Delta\rho}{\bar{\rho}} \right\} \frac{\sin^3 i_1}{\cos j_1} \\
&+ \left[\left(\frac{\bar{\alpha}^2}{2\left(\bar{\alpha}^2 - \bar{\beta}^2\right)\cos j_1} + \frac{\bar{\alpha}\bar{\beta}\cos i_1}{2\left(\bar{\alpha}^2 - \bar{\beta}^2\right)} \right) \left(\delta_1^{(V)} - \delta_2^{(V)} \right) \right] \sin i_1 \\
&+ \left[\frac{\bar{\beta}\bar{\alpha}\cos i_1}{\left(\bar{\alpha}^2 - \bar{\beta}^2\right)} \left(\delta_2^{(V)} - \delta_1^{(V)} + \epsilon_1^{(V)} - \epsilon_2^{(V)} \right) \right] \sin^3 i_1 \\
&+ \left[\frac{\bar{\alpha}^2}{\left(\bar{\alpha}^2 - \bar{\beta}^2\right)\cos j_1} \left(\delta_2^{(V)} - \delta_1^{(V)} + \epsilon_1^{(V)} - \epsilon_2^{(V)} \right) \right] \sin^3 i_1 \\
&+ \left[\frac{\bar{\beta}^2}{2\left(\bar{\alpha}^2 - \bar{\beta}^2\right)\cos j_1} \left(\delta_2^{(V)} - \delta_1^{(V)} \right) \right] \sin^3 i_1 \\
&+ \left[\frac{\bar{\beta}^2}{\left(\bar{\alpha}^2 - \bar{\beta}^2\right)\cos j_1} \left(\delta_1^{(V)} - \delta_2^{(V)} + \epsilon_2^{(V)} - \epsilon_1^{(V)} \right) \right] \sin^5 i_1
\end{aligned}
$$

- $S^{\perp}P$ reflection coefficient (symmetry-axis plane)

$$
\begin{aligned}
\grave{S}^{\perp}\acute{P} \;=\; & -1/2\, \frac{\Delta\rho}{\bar{\rho}} \frac{\sin j_1}{\cos i_1} \\
& - \frac{\bar{\beta}}{\bar{\alpha}} \left\{ \frac{\Delta\rho}{\bar{\rho}} + 2\left(\frac{\Delta\beta}{\bar{\beta}} + \gamma_1 - \gamma_2 \right) \right\} \sin j_1 \cos j_1 \\
& + \left\{ 2\left(\frac{\Delta\beta}{\bar{\beta}} + \gamma_1 - \gamma_2 \right) + \frac{\Delta\rho}{\bar{\rho}} \right\} \frac{\sin^3 j_1}{\cos i_1} \\
& + \left[\left(\frac{\bar{\alpha}\bar{\beta}\cos j_1}{2(\bar{\alpha}^2 - \bar{\beta}^2)} - \frac{\bar{\alpha}^2 \cos^2 j_1}{2(\bar{\alpha}^2 - \bar{\beta}^2)\cos i_1} \right) \left(\delta_1^{(V)} - \delta_2^{(V)} \right) \right] \sin j_1 \\
& + \left[\frac{\bar{\alpha}^3 \cos j_1}{\bar{\beta}\left(\bar{\alpha}^2 - \bar{\beta}^2\right)} \left(\delta_2^{(V)} - \delta_1^{(V)} + \epsilon_1^{(V)} - \epsilon_2^{(V)} \right) \right] \sin^3 j_1 \\
& - \left[\frac{\bar{\alpha}^4 \cos^2 j_1}{\bar{\beta}^2\left(\bar{\alpha}^2 - \bar{\beta}^2\right)\cos i_1} \left(\delta_2^{(V)} - \delta_1^{(V)} + \epsilon_1^{(V)} - \epsilon_2^{(V)} \right) \right] \sin^3 j_1
\end{aligned}
$$

- $S^{\perp}P$ transmission coefficient (symmetry-axis plane)

$$
\begin{aligned}
\grave{S}^{\perp}\grave{P} \;=\; & -1/2\, \frac{\Delta\rho}{\bar{\rho}} \frac{\sin j_1}{\cos i_1} \\
& + \frac{\bar{\beta}}{\bar{\alpha}} \left\{ \frac{\Delta\rho}{\bar{\rho}} + 2\left(\frac{\Delta\beta}{\bar{\beta}} + \gamma_1 - \gamma_2 \right) \right\} \sin j_1 \cos j_1 \\
& + \left\{ 2\left(\frac{\Delta\beta}{\bar{\beta}} + \gamma_1 - \gamma_2 \right) + \frac{\Delta\rho}{\bar{\rho}} \right\} \frac{\sin^3 j_1}{\cos i_1}
\end{aligned}
$$

$$
\begin{aligned}
&+\left[\left(\frac{\bar{\alpha}\bar{\beta}\cos j_1}{2\left(\bar{\alpha}^2-\bar{\beta}^2\right)}+\frac{\bar{\alpha}^2\cos^2 j_1}{2\left(\bar{\alpha}^2-\bar{\beta}^2\right)\cos i_1}\right)\left(\delta_2^{(V)}-\delta_1^{(V)}\right)\right]\sin j_1\\
&-\left[\frac{\bar{\alpha}^3\cos j_1}{\bar{\beta}\left(\bar{\alpha}^2-\bar{\beta}^2\right)}\left(\delta_2^{(V)}-\delta_1^{(V)}+\epsilon_1^{(V)}-\epsilon_2^{(V)}\right)\right]\sin^3 j_1\\
&-\left[\frac{\bar{\alpha}^4\cos^2 j_1}{\bar{\beta}^2(\bar{\alpha}^2-\bar{\beta}^2)\cos i_1}\left(\delta_2^{(V)}-\delta_1^{(V)}+\epsilon_1^{(V)}-\epsilon_2^{(V)}\right)\right]\sin^3 j_1
\end{aligned}
$$

Appendix E

SHEAR-WAVE REFLECTION IN SYMMETRY PLANES OF ORTHORHOMBIC MEDIA

The derivations of HTI and orthorhombic media reflection coefficients are very similar. Analysis of symmetry-plane Christoffel systems yields the scattering coefficients and naturally leads to the introduction of a new effective parameterization (Tsvankin, 1996a). For completeness, I state the $[x_1, x_3]$-symmetry-plane reflection coefficients for the shear wave polarized (for vertical incidence and symmetry-plane propagation) in the $[x_1, x_3]$-plane ($S^{\perp}$), and in the $[x_2, x_3]$-plane ($S^{\parallel}$):

$$\begin{aligned} \mathrm{R}_{S^{\parallel}}^{[x_1,x_3]} &= \mathrm{R}_{SH}^{\mathrm{iso}} + 1/2\,\Delta\gamma^{(2)} \tan^2 j \\ \mathrm{R}_{S^{\perp}}^{[x_1,x_3]} &= \mathrm{R}_{SV}^{\mathrm{iso}} + 1/2 \left(\frac{\bar{\alpha}}{\bar{\beta}^{\perp}}\right)^2 (\Delta\epsilon^{(2)} - \Delta\delta^{(2)}) \sin^2 j\,, \end{aligned} \tag{E.1}$$

with shear-wave velocities $\beta = \sqrt{c_{44}/\rho}$ in $\mathrm{R}_{S^{\parallel}}^{[x_1,x_3]}$ and $\beta^{\perp} = \sqrt{c_{55}/\rho}$ in $\mathrm{R}_{S^{\perp}}^{[x_1,x_3]}$. Parameters $\delta^{(2)}$ and $\epsilon^{(2)}$ are responsible for near-vertical and near-horizontal P-wave propagation, respectively, exactly as δ and ϵ in VTI models. $\gamma^{(2)}$ determines the velocity variation of the $S^{\parallel}$ wave polarized normal to the $[x_1, x_3]$-plane. The reflection coefficients $\mathrm{R}_{SH}^{\mathrm{iso}}$ and $\mathrm{R}_{SV}^{\mathrm{iso}}$ are shown in Chapter 2 and need to be evaluated for the corresponding vertical shear-wave velocities.

For shear waves propagating in the $[x_2, x_3]$-plane, the solutions for the reflection coefficients are as follows:

$$\begin{aligned} \mathrm{R}_{S^{\parallel}}^{[x_2,x_3]} &= \mathrm{R}_{SH}^{\mathrm{iso}} + 1/2 \left(\frac{\bar{\alpha}}{\bar{\beta}}\right)^2 (\Delta\epsilon^{(1)} - \Delta\delta^{(1)}) \sin^2 j\,. \\ \mathrm{R}_{S^{\perp}}^{[x_2,x_3]} &= \mathrm{R}_{SV}^{\mathrm{iso}} + 1/2\,\Delta\gamma^{(1)} \tan^2 j\,. \end{aligned} \tag{E.2}$$

As before, the $S^{\parallel}$-wave coefficients are shown with velocity β whereas the $S^{\perp}$-wave vertical shear-velocity is $\beta^{\perp}$. A definition of the new effective coefficients and their relations to the generic Thomsen parameters (VTI) and HTI parameters is given in Chapter 7.